



# Failure of heterogeneous materials: A dynamic phase transition?

D. Bonamy<sup>a</sup>, E. Bouchaud<sup>b,\*</sup>

<sup>a</sup> CEA-Saclay, IRAMIS, SPCSI, Groupe Complex Systems & Fracture, F-91191 Gif-sur-Yvette, France

<sup>b</sup> CEA-Saclay, IRAMIS, SPEC, Groupe Instabilités et Turbulence, Orme des Merisiers, F-91191 Gif-sur-Yvette, France

## ARTICLE INFO

### Article history:

Accepted 29 June 2010

Available online 4 August 2010

editor: I. Procaccia

## ABSTRACT

While there exists a unified theoretical framework – Linear Elastic Fracture Mechanics – to describe the failure of homogeneous materials, understanding and modeling the mechanical properties of heterogeneous media continue to raise significant fundamental challenges. Stress enhancement in the vicinity of cracks indeed makes classical homogenization methods irrelevant to predict the toughness and lifetime of heterogeneous materials. “Mean field” approaches have been proposed to estimate these quantities, but they remain limited to dilute damage.

Numerical simulations do not suffer from such limitations, and disorder can be tuned continuously. Molecular Dynamics simulations allow one to characterize damage and fracture in amorphous materials at the nanoscale, i.e. at the scale of their inhomogeneities. However, these simulations are up to now limited to dynamic fracture, which confers further complexity to the observed mechanisms. A “minimalist” approach consists in exploiting the analogy between scalar mode III elasticity and electricity through the study of random fuse networks breakdown. In two dimensions, powerful algorithms can compute the exact stress field in an elastic medium containing cracks of arbitrary shapes. However, although these tools have been useful in solving some classical problems (e.g. size dependence of materials strength), a clear predictive unified theoretical framework is still missing.

An efficient theory should be able to predict, *a minima*, the morphology of fracture surfaces, which encodes the interaction between the propagating crack front and the surrounding microstructure. We provide a review of recent quantitative fractography experiments. The most striking observations in this field is the existence of universal morphological features, independent of both the material and the loading conditions, reminiscent of interface growth problems. In this context, we analyze models which describe the crack front as an elastic line that propagates in a random potential. In these models, the onset of crack propagation is interpreted as a dynamic phase transition, while sub-critical crack growth is assimilated to thermally assisted depinning.

© 2010 Elsevier B.V. All rights reserved.

## Contents

1. Introduction.....	2
2. Elements of fracture mechanics.....	3
2.1. Failure of ideal elastic materials .....	3
2.1.1. Linear elastic fracture mechanics: Basic concepts.....	3
2.1.2. Straight cracks.....	4

\* Corresponding address: Norwegian University of Science and Technology (NTNU), Department of Physics, Hogskoleringen 5, N-7491 Trondheim, Norway.

E-mail address: [elisabeth.bouchaud@cea.fr](mailto:elisabeth.bouchaud@cea.fr) (E. Bouchaud).

2.1.3.	Weakly distorted cracks .....	5
2.1.4.	Crack path .....	7
2.2.	Failure of real materials: mechanisms of energy dissipation .....	7
2.2.1.	Fracture of single crystals: cleavage .....	7
2.2.2.	Fracture of metals: The importance of plasticity .....	8
2.2.3.	Quasi-brittle fracture .....	9
2.2.4.	Fracture of glass: Brittle or quasi-brittle? .....	10
3.	Morphology of fracture profiles .....	10
3.1.	Fracture of a paper sheet .....	11
3.2.	Interfacial fracture .....	13
3.2.1.	Self-affine properties of the crack front .....	13
3.2.2.	Spatio-temporal evolution: avalanche dynamics .....	13
3.3.	Fracture of a three-dimensional solid .....	16
3.3.1.	In-plane crack roughness .....	16
3.3.2.	Out-of-plane roughness: A universal exponent? .....	16
3.3.3.	Exceptions: Small exponents .....	19
3.3.4.	Transient regime: From a straight notch to a rough front .....	20
4.	Morphology of fracture surfaces .....	21
4.1.	Anisotropy of fracture surfaces .....	21
4.1.1.	Two-dimensional structure function .....	22
4.1.2.	Two classes of universality .....	23
5.	Statistical models of fracture .....	24
5.1.	Molecular dynamics simulations .....	25
5.1.1.	Fracture of bidimensional Lennard-Jones glasses .....	25
5.1.2.	Fracture and damage of silicate glasses and ceramics .....	26
5.2.	Non-perturbative semi-analytic solution in two-dimensions: Iterated conformal mapping .....	28
5.3.	A “mean field” approach to failure: Fiber bundle models .....	28
5.4.	Random fuse models .....	29
5.4.1.	Damage precursors: avalanches .....	31
5.4.2.	Crack surfaces in perfectly plastic RFM: A minimum energy surface .....	32
5.4.3.	Crack surfaces in brittle RFM: A gradient percolation process .....	32
5.4.4.	Crack surfaces in brittle RFM: Numerical results .....	33
6.	Models of an elastic front propagating through randomly distributed obstacles .....	33
6.1.	Equation of motion: Interfacial crack front .....	34
6.1.1.	Velocity evolution as a function of the loading .....	34
6.1.2.	Effective toughness distribution .....	35
6.1.3.	Displacement-imposed quasi-static failure: Intermittency and crackling noise .....	36
6.1.4.	In-plane roughness predictions .....	36
6.2.	Morphology of fracture surfaces: Three-dimensional crack front .....	37
6.2.1.	A phenomenological model derived from symmetry principles .....	37
6.2.2.	Path equations within a linear elastic description: 2D case .....	38
6.2.3.	Path equations within a linear elastic description: 3D case .....	39
7.	Discussion .....	40
	Acknowledgements .....	41
	References .....	41

## 1. Introduction

The role of heterogeneities on the fracture properties of materials is still an open question, although it has been debated for years. It is far from being incidental, since what we call “heterogeneities” in materials are actually driving their mechanical properties. Heterogeneities of all kinds are generally incorporated in order to reach a good compromise in mechanical properties. This has been noticed since the bronze age as far as metallic alloys are concerned: pure metals are far too soft to be used with no additions. Actually, metallic alloys [1,2] may contain heterogeneities of all sizes ranging from the atomic scale (solute atoms, vacancies, ...) to scales which may be much larger (grains and their boundaries), through all kinds of intermediate scales (second phase precipitates, ...). On the contrary, polymers are used for their high rigidity and light weight, but they lack ductility. This is why soft rubber particles may be added [3,4]. Amorphous materials behave as homogeneous materials even at relatively small scales, but structural disorder may have important consequences at nanometric scales [5–7].

Understanding the local mechanisms of damage and fracture at such fine scales is not easy, and a large effort is devoted to perform *in situ* reliable observations. Several experimental techniques have been employed for that purpose: Scanning or Transmission Electron Microscopy have been used for several years, while the development of near field microscopy approaches is more recent. In parallel with the improvement of experimental devices, progress in computing has led to an important advance in the field. Nowadays, if a lot has been understood for metallic materials, it is not so for amorphous bodies, for which there is no equivalent to the theory of dislocations.

In any case, taking into account explicitly every single mechanism to build up a fracture theory of heterogeneous materials is fundamentally inconceivable, and the goal is indeed to include basic mechanisms into a statistical description. This may be straightforward for some properties such as elastic moduli – in most cases, a simple “law of mixtures” gives a fairly accurate result –, but when it comes to fracture-related properties, averaging is definitely not easy, and, sometimes, even counterintuitive. Think, for example, that one efficient way to stop a crack is to drill a hole in front of it: two “damages” in this case amount to canceling each other’s effect.

There are several sources of complication as soon as there is even a single crack in a sample. First, cracks act as stress concentrators, which means that there are strong stress gradients around them. Secondly, when dealing with a heterogeneous material containing elements with different breaking thresholds, one should expect the most brittle ones to crack first. This means that extreme statistics rule the phenomenon, and this is by no means easy to deal with, neither conceptually nor experimentally. Because of stress concentration and because secondary cracks nucleate at heterogeneities, it is impossible to replace a heterogeneous material by an “effective equivalent material” with simple average properties.

One of the aims of this review is to gather the most important results obtained during the past thirty years or so, which aim at building up a sound theory of fracture of heterogeneous media. Before examining the models, which is done in Sections 5 and 6, we provide the reader with basic notions of linear elastic fracture mechanics in Section 2. Because heterogeneities induce local stresses, they tend to distort the crack front, which results in further modifications of the stress field. They can even produce a local shear whereas the sample is loaded externally in pure tension. But of course, real materials are not linear elastic at all scales. Dissipative processes which usually occur in the vicinity of the crack front – plasticity, multiple cracking, etc. . . – and strongly alter the stress field, are also described in Section 2.

We focus in this review on experiments dealing with the morphology of cracks and fracture surfaces, starting in Section 3 with results concerning the morphology of profiles, whether these profiles are cracks through a thin sheet or the intercept of a vertical plane with the fracture surface resulting from the fracture of a bulk material. In both cases, we will report results showing that in general these lines have scale-invariant properties characterized by roughness exponents which define large universality classes among materials.

In Section 4, we will present more recent experimental results showing that these scaling properties are anisotropic, with exponents depending on the direction of observation, relative to the direction of crack propagation. Two classes of universality clearly emerge: one concerns observations performed at scales large enough so that the material can be considered as purely linear elastic, and the other deals with measurements performed with the so-called “Process Zone”, where all dissipative processes occur.

Several models have attempted to take heterogeneities into account by introducing a certain degree of randomness. Several of these models, their successes and their limitations, are summarized in Section 5. Section 6 is devoted to models which aim at predicting the in-plane and out-of-plane fluctuations of an elastic crack front which has to find its path through an array of microstructural obstacles. As we shall see, some of these models reproduce quite well experimental observations in the purely elastic regime, for what concerns both the morphology of the front and the one of the fracture surface it leaves behind in its wake, and the dynamics of its intermittent propagation. This shows that crack propagation in a disordered solid is a dynamic phase transition, the order parameter being the average crack velocity, and the control parameter being the external applied load. Finally, Section 7 is devoted to a discussion, where we have tried to make a list of still open questions.

## 2. Elements of fracture mechanics

Before tackling fracture of heterogeneous media, it is necessary to recall the basic notions of Linear Elastic Fracture Mechanics (LEFM). This continuum theory, born during the first half of the twentieth century, is at the origin of considerable progress in the understanding of structural failure.

### 2.1. Failure of ideal elastic materials

LEFM applies to homogeneous materials as long as they can be considered as linear elastic, i.e. when nonlinear and dissipative processes only concern a very limited volume of material around the crack tip, called the Fracture Process Zone (FPZ). We first recall some basic concepts (Section 2.1.1), apply them to the simple case of straight cracks progressing quasi-statically (Section 2.1.2), and then consider perturbations where cracks are slightly distorted (Section 2.1.3).

#### 2.1.1. Linear elastic fracture mechanics: Basic concepts

A crack in an ideally elastic solid, where the FPZ can be considered to have a size zero, will remain stable as long as the amount  $G$  of mechanical energy per unit area released by the solid as the crack propagates by an infinitesimal length does not overcome the energy per unit area dissipated to create two new fracture surfaces. The latter,  $\Gamma$ , is classically referred to as the *fracture energy* [8]. The so-called Griffith criterion for crack propagation then reads:

$$G \geq \Gamma. \quad (1)$$

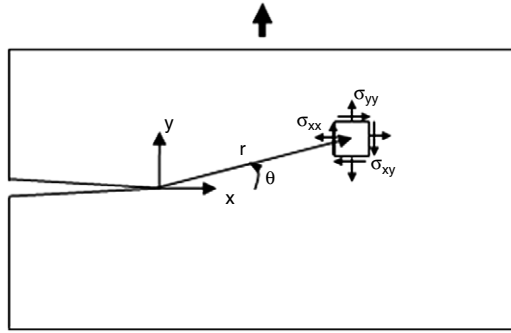


**Fig. 1.** Sketch and notation describing the stress field in the vicinity of a slit crack tip in a two-dimensional medium.

Once Griffith's criterion is fulfilled the crack starts to move;  $G = \Gamma$  corresponds to the onset of propagation. Under quasi-static conditions, the crack velocity is proportional to the excess elastic energy release [9], i.e. to the difference between the static energy release rate  $G$  – the amount of energy per unit area present at the tip of a static crack – and the fracture energy  $\Gamma$ :

$$\frac{1}{\mu}v = G - \Gamma \quad (2)$$

where  $\mu$  is the effective mobility of the crack front. When  $v$  becomes important, the quasi-static assumption stops being valid and  $v$  is given by balancing the mechanical energy flux into the process zone with the dissipation rate  $\Gamma v$ . This flux balance then takes the following form [9]:

$$GA(v) = \Gamma \quad (3)$$

where  $A(v)$  is a universal function of  $v$  and  $G$  is the mechanical energy released at the tip of a static crack. In first approximation,  $A(v)$  is shown to take the following form:

$$A(v) \approx 1 - \frac{v}{c_R} \quad (4)$$

and  $c_R$  is the Rayleigh wave speed, i.e. the speed of acoustic waves propagating along the surface of the considered material. Inverting this relation yields the following equation of motion for a dynamically moving crack:

$$v = c_R \left( 1 - \frac{\Gamma}{G} \right). \quad (5)$$

Experiments performed on nominally brittle materials are described well by this equation as long as crack growth is slow enough [10]. As a matter of fact, several discrepancies have been evidenced when the crack velocity is large enough [11–14]. This dynamic fracture regime is beyond the scope of the present review. The interested reader can refer to the reviews of Ravi-Chandar [15] and Fineberg and Marder [16] for details.

### 2.1.2. Straight cracks

Describing material failure within the LEFM theory requires the computation and comparison of two quantities (Eq. (1)): (i) the fracture energy  $\Gamma$  and (ii) the mechanical energy release rate  $G$ . What sets the value of  $\Gamma$  in a given material depends crucially on the complex damage and dissipative processes occurring within the FPZ, at the scale of the material microstructure. Several examples of such dissipative processes will be given in Section 2.2. No basic principle allows to predict its value from the knowledge of the chemical and the microstructural compositions. On the contrary, the second term depends on the stress and displacement fields outside the FPZ, and it can be computed using Linear Elasticity. Let us first consider the case of a straight crack embedded in a two-dimensional medium under tension, as depicted in Fig. 1. As first shown by Irwin, the stress field  $\sigma$  exhibits a square root singularity at the crack tip:

$$\sigma_{ij} \approx \frac{K}{\sqrt{2\pi r}} F_{ij}(\theta) \quad (6)$$

where  $r$  is the distance to the crack tip and  $\theta$  is the angle with respect to the crack, as depicted in Fig. 1. While the functional forms of  $F_{ij}(\theta)$  are universal, the prefactor  $K$ , called the *stress intensity factor* depends on the crack length, on the specimen geometry and on the applied tension. Note that Eq. (6) implies that  $K$  being the product of a stress by the square root of a length is expressed in MPa m<sup>1/2</sup>.

This notion can be generalized for any loading condition. In this respect, it is convenient to distinguish three basic modes, as depicted in Fig. 2: Mode I (tensile mode) corresponds to a crack propagating in a plane perpendicular to the uniaxial tensile

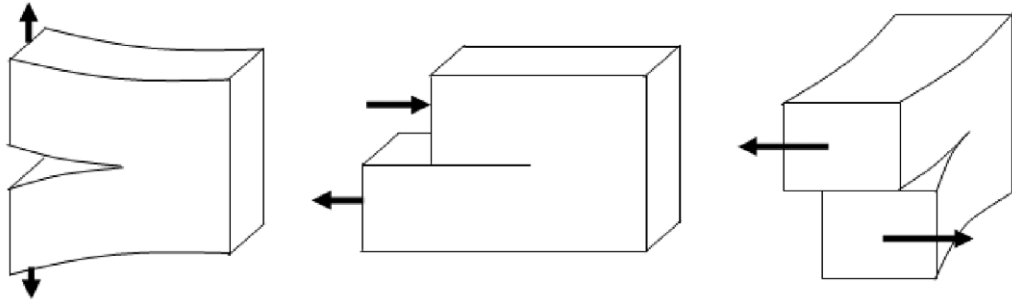


**Fig. 2.** The three modes of fracture: Tensile mode (Mode I), shearing mode (Mode II) and tearing mode (Mode III).

stress; mode II (shearing mode) corresponds to a shear of the crack walls in a direction normal to the crack front; and mode III (tearing mode) corresponds to a shear parallel with the crack front. Any set of loading conditions can be decomposed into a sum of these three basic modes. To leading order, the stress field in the vicinity of the crack tip can be written as:

$$\sigma_{ij} \approx \frac{1}{\sqrt{2\pi r}} \{ F_{ij}^I(\theta) K_I + F_{ij}^{II}(\theta) K_{II} + F_{ij}^{III}(\theta) K_{III} \} \quad (7)$$

where  $K_I$ ,  $K_{II}$  and  $K_{III}$  are called mode I, mode II and mode III stress intensity factors, respectively. The mechanical energy release rate  $G$  is then shown to be equal to:

$$G = \frac{K_I^2}{E'} + \frac{K_{II}^2}{E'} + (1 + \nu) \frac{K_{III}^2}{E'} \quad (8)$$

where  $\nu$  is the Poisson ratio of the material, and  $E'$  is either equal to the Young's modulus  $E$  in the plane stress situation – typically at the free surface of a three dimensional solid where the perpendicular components of the stress have to be zero – and  $E'$  is equal to  $E/(1 - \nu^2)$  in plane strain conditions – i.e. typically within the bulk of the specimen –.

Of the three modes, the first one is by far the most relevant to crack propagation in solids. As we shall see later, in virtue of the so-called *principle of local symmetry*, there is always a tendency for a brittle crack to seek an orientation that minimizes the tip shear loading in an isotropic solid. Therefore, in all the fracture processes to be discussed in this paper, we will consider solids loaded dominantly in tension where the local perturbations in modes II and III induced by microstructural processes will be subordinated to that of mode I. In that case, Eq. (8) reduces to:

$$G = \frac{K_I^2}{E'}. \quad (9)$$

For a crack of length  $a$  in an infinite medium, it can be shown that  $K_I$  is proportional to  $a^{1/2}$ , which means that the elastic energy release rate  $G$  is proportional to  $a$ .

Defining the fracture toughness  $K_{lc}$  of a material by  $K_{lc} = \sqrt{\Gamma E}$ , one can rewrite Griffith's criterion for crack propagation (Eq. (1)) as:

$$K_I \geq K_{lc}. \quad (10)$$

Linear elasticity also allows one to compute the next terms in the expansion of the stress field at the tip of a straight crack. The non-singular terms of the development become increasingly important farther from the crack tip, but they do not intervene in the computation of  $G$  given by Eq. (9). One has:

$$\sigma_{ij} \approx \frac{K_I}{\sqrt{2\pi r}} F_{ij}^I(\theta) + T_I G_{ij}^I(\theta) + A_I \sqrt{r} H_{ij}^I(\theta) + \dots \quad (11)$$

where  $F_{ij}^I(\theta)$ ,  $G_{ij}^I(\theta)$  and  $H_{ij}^I(\theta)$  are universal functions of  $\theta$ . As for  $K_I$ , the constants  $T_I$  (called  $T$ -stress) and  $A_I$  depend on the crack length, on the geometry of the specimen and on the loading conditions. These terms turn out to be important when one seeks to compute the local variation of stress intensity factors along the front of a slightly non-planar crack [17]. As it will be seen in the the following section, the non singular terms are involved in the calculation of the corrections to the stress intensity factors due to the presence of disorder.

### 2.1.3. Weakly distorted cracks

As a matter of fact, a crack propagating slowly enough in a homogeneous elastic material remains perfectly smooth. One can then determine – at least numerically – the values of the stress intensity factors along the crack front. In a heterogeneous material, defects induce distortions of the crack front, which in turn modify the values of the stress intensity factors along it. First order perturbation analysis has been used to relate the modifications of the stress-intensity factors to the deviations from straightness.

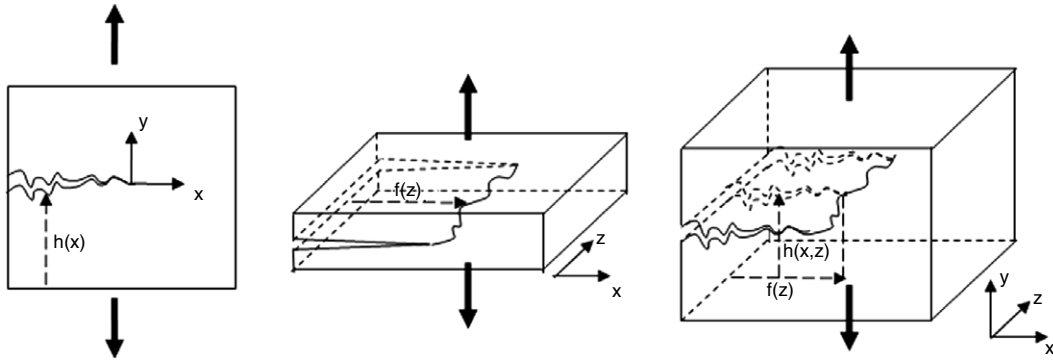


**Fig. 3.** Sketch and notations for distorted cracks in two-dimensional tensile geometry (a) two-dimensional interfacial geometry (b) and three-dimensional geometry (c).

Let us first consider the reference situation where a half-plane straight crack  $S_0 = \{\mathbf{r} = (x, y, z) \in \mathbb{R}^3 : x < 0, y = 0\}$  in an infinite body is loaded in tension, and let us call  $K_I^0(z)$  the local stress intensity factor at location  $z$  along the crack edge. Let us now perturb the situation as depicted in Fig. 3(b) by adding a small deviation  $f(z)$  to each point along the crack front:  $S_0 \rightarrow S = \{\mathbf{r} = (x, y, z) \in \mathbb{R}^3 : x \leq f(z), y = 0\}$ . The change in  $K_I(z) = K_I^0(z) + \delta K_I(z)$  induced by crack roughness can be computed using perturbation analysis. Meade and Keer [18], and Rice [19] have shown that, to first order in  $f$ :

$$K_I(z) \simeq K_I^0(z) + \frac{1}{\sqrt{2\pi}} PV \int_{-\infty}^{\infty} K_I^0(z') \frac{f(z') - f(z)}{(z' - z)^2} dz' + o(f^2) \quad (12)$$

where  $PV$  denotes the principal value of the integral. As we will discuss extensively in Section 6, this solution has been used for understanding the roughening of a crack front [20,21]. The resulting predictions were initially claimed to be in apparent disagreement with experimental observations [22,23]. This has led Adda-Bedia et al. [24] to derive a second order approximation for the local value of  $K_I(z)$ :

$$\begin{aligned} K_I(z) \simeq K_I^0(z) &+ \frac{1}{2\pi} PV \int_{-\infty}^{\infty} K_I^0(z') \frac{f(z') - f(z)}{(z' - z)^2} dz' \\ &+ \frac{1}{(2\pi)^2} PV \int_{-\infty}^{\infty} \int_{-\infty}^{\infty} K_I^0(z') \frac{[f(z') - f(z)][f(z'') - f(z')]}{(z' - z)^2(z'' - z')^2} dz'' dz' - \frac{1}{8} K_I^0(z) \left( \frac{\partial f}{\partial z} \right) + o(f^3). \end{aligned} \quad (13)$$

Another simple 2D situation of interest is the one depicted in Fig. 3(a), where an initially semi-infinite straight crack within a 2D elastic material is slightly distorted:  $S_0 \rightarrow S = \{\mathbf{r} = (x, y) \in \mathbb{R}^2 : x < 0, y = h(x)\}$ . The stress field in the vicinity of the distorted crack tip is then characterized by the stress intensity factors  $K_I$  and  $K_{II}$ . Asymptotic analysis has been used to relate their value to the crack distortion  $h(x)$  and to the reference value  $K_I^0$  of the mode I stress intensity factor for the reference situation  $S_0$ . It turns out [25,17] that the first order approximation of  $K_I$  and  $K_{II}$  requires a three term expansion of the stress field near the reference straight crack  $S_0$ , given by Eq. (11). It reads [17]:

$$\begin{aligned} K_I &= K_I^0 \\ K_{II} &= \frac{1}{2} K_I^0 \frac{dh}{dx} \Big|_{x=0} - \sqrt{\frac{\pi}{2}} A_I^0 h(0) - \int_{-\infty}^0 w(u) \frac{d}{dx}(h(x) T(x))|_u du \end{aligned} \quad (14)$$

where  $T(x)$  denotes the  $T$ -stress acting on the crack face in the reference straight situation  $S_0$ .  $w(u)$  is called a weight function, and depends on the geometry of the specimen. For an infinite plate, it is equal to:

$$w(u) = \frac{1}{\sqrt{-\pi u}}. \quad (15)$$

One can now look at the more complex 3D situation  $S = \{\mathbf{r} = (x, y, z) \in \mathbb{R}^3 : x < f(z), y = h(x, z)\}$  of a reference semi-infinite straight crack  $S_0 = \{\mathbf{r} = (x, y, z) \in \mathbb{R}^3 : x < 0, y = 0\}$  embedded into an isotropic linear elastic medium under tension  $K_I^0$  (Fig. 3(c)). Perturbation analysis can be used to compute the changes  $K_I(z) - K_I^0$ ,  $K_{II}(z)$  and  $K_{III}(z)$  in stress intensity factors at location  $\mathbf{M} = (x = f(z), y = h(x = f(z), z), z)$  as a function of both the in-plane  $f(z)$  and the out-of-plane  $h(x, z)$  distortions of the crack front. To linear order,  $K_I(z)$  depends on  $f$  only, and is given by Eq. (12), while  $K_{II}(z)$  and  $K_{III}(z)$  are functionals of  $h$  only [26,27,17]. These two last quantities read [17]:

$$K_{II} = -\sqrt{\frac{\pi}{2}} A_I^0 h(0, z) + \frac{1}{2} K_I^0 \frac{\partial h}{\partial x} \Big|_{(0,z)} + \frac{1}{\pi} \frac{2-3\nu}{2(2-\nu)} K_I^0 \int_{-\infty}^{\infty} \frac{1}{z-z'} \frac{\partial h}{\partial z} \Big|_{(0,z')} dz' + \Delta K_{II}^{\text{morphology}} \quad (16)$$

$$K_{III} = (1-2\nu) K_I^0 \frac{\partial h}{\partial z} \Big|_{(0,z)} + \frac{1}{\pi} \frac{\nu}{2-\nu} K_I^0 \frac{\partial h}{\partial z} \Big|_{(0,z)} + \Delta K_{III}^{\text{morphology}} \quad (17)$$

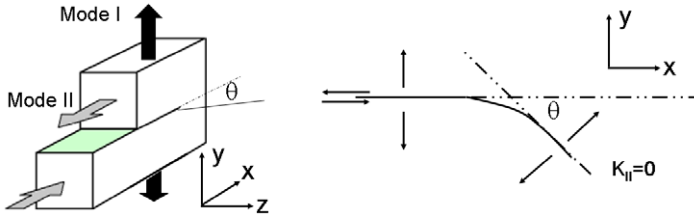


**Fig. 4.** Principle of local symmetry: A crack will propagate so that local shear vanishes at its tip, i.e.  $K_{II} = 0$ .

where  $\nu$  is the Poisson ratio, and the two quantities  $\Delta K_{II}^{\text{morphology}}(z)$  and  $\Delta K_{III}^{\text{morphology}}(z)$  depend on the two components of the  $T$ -stress acting on the crack surface in the reference straight situation  $S_0$  [17].

Eqs. (12)–(17) allow one to relate local loading perturbations along the crack front to the in-plane and out-of-plane distortions of the crack front within the *elastostatic* theory, i.e. when the velocity of the crack front is much smaller than the Rayleigh wave speed  $c_R$ . Analytical solutions in the framework of the full three dimensional elastodynamic theory were later established by Willis and Movchan [28,29]. They allowed Ramanathan and Fisher [30] and Morrissey and Rice [31,32] to show that in-plane and out-of-plane perturbations can propagate as waves along the crack front. This new kind of waves, referred to as *crack front waves*, propagate along crack fronts and can thus persist for quite a long time without geometric attenuation. The predictions of such crack front waves have gained a lot interest after Sharon et al. [33] have seemed to observe them experimentally: they investigated the response of a crack in soda-lime glass, the propagation of which is perturbed locally by scribing one face of the plate with a groove, and they observed tracks on the *post mortem* fracture surface, emerging from the groove, that they claimed to be the signature of crack front waves. Those were then suggested to be the possible source of crack surface roughening in brittle materials [34] or the key mechanism explaining the discrepancy between predicted crack velocities and experimentally observed ones [35]. However, subsequent experiments [36,37] allowed to revisit Sharon et al.'s experiments and reinterpret the observed post-mortem tracks as Wallner lines, i.e. undulations resulting from the interaction between the crack front and shear waves, and not the crack front waves predicted theoretically. At present, if the existence of crack front waves is theoretically proven, their experimental observation remains controversial [38,39].

#### 2.1.4. Crack path

To close this section devoted to fracture of linear elastic materials, one has finally to discuss how a moving crack chooses its path. Provided that the crack is quasi-static, i.e. that its growth rate is small with respect to the Rayleigh wave speed, the path followed by a crack in an elastic material obeys the so-called “Principle of Local Symmetry” (PLS) [40]. In 2D systems, the crack front is loaded in mode I + II and the PLS states that a crack extends so as to set the component of Mode II loading to zero (Fig. 4).

In 3D systems, the crack load can also contain a mode III part. In this case, the front should turn along the axis  $x$  parallel with the direction of propagation, which implies a *variable* tilted angle along the front. In this case, the crack front splits into multiple fronts to form “lances” [41], the physical origin and characteristic length scale of which still remains to be understood.

All these considerations, once again, only apply to the ideal case of a perfectly linear elastic material, or to a real material at much larger scales than the FPZ size. On the contrary, at smaller length scales, within the FPZ, various processes occur where most of the energy is spent without any crack progression. Within the FPZ, the material cannot be considered as linear elastic any longer, and as a consequence, as we shall see in Sections 3 and 4, the morphology and the dynamics of cracks are completely different.

## 2.2. Failure of real materials: mechanisms of energy dissipation

Indeed, failure of real materials usually does not occur as simply as successive breaking of atomic bonds at the crack tip, mainly because real materials contain “defects” which are more or less tough, and are likely to break at different load levels. Even in intrinsically brittle materials such as glass, wood, rocks or cement, the energy spent in the nucleation and growth of microfractures around the main crack tip represent a significant part of the total energy spent during the failure process. In the particular case of metallic materials, huge plastic deformations are due to the nucleation and movement of dislocations emitted at the crack tip. The energy dissipated in plastic deformation is actually much larger than the energy needed to create two fracture surfaces. The case which is closer to the ideal “homogeneous elastic” solid is a brittle perfect single crystal.

### 2.2.1. Fracture of single crystals: cleavage

Cleavage is the rapid propagation of a crack along a crystallographic plane which is usually of lower atomic density. When this plane is oriented well with respect to the loading direction, i.e. when a mode I crack can propagate within this plane, fracture occurs through the successive breaking of atomic bonds at the crack tip (see Fig. 5). Whenever this plane is not oriented well with respect to the tensile axis, crack propagation is preceded by the creation of defects.

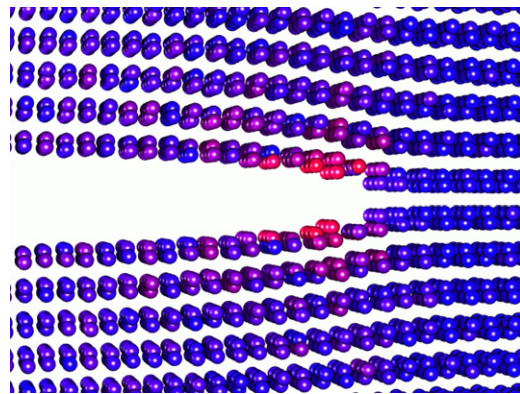


**Fig. 5.** Vicinity of a crack tip propagating in a single silicon crystal (Courtesy of M. Marder).

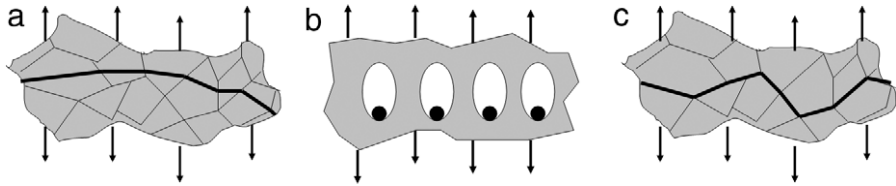


**Fig. 6.** Sketch of the various modes of failure within a polycrystalline metallic material: (a) Cleavage. (b) Ductile fracture. (c) Intergranular fracture.



**Fig. 7.** Vicinity of the crack tip in a Ti<sub>3</sub>Al-based alloy as observed in situ in Scanning Electron Microscopy (From [42]).

### 2.2.2. Fracture of metals: The importance of plasticity

Cleavage can also happen in metallic materials (see Fig. 6(a)). It may be brittle, or it can follow ductile fracture. It is most likely in the case of restricted plastic flow. For FCC metals, for example, there are several slip systems and fracture is ductile at all temperatures. On the contrary, BCC metals break in cleavage at low temperatures because of the limited number of slip systems.

Ductile crack growth proceeds through the initiation, growth and coalescence of voids ahead of a preexisting crack tip (see Figs. 6(b) and 7). Voids nucleate usually around second phase particles: either these particles break (as is the case in the Ti<sub>3</sub>Al-based alloy of Fig. 7), or there is a decohesion between the matrix and precipitate (this is the case for the AlSi alloy shown in Fig. 8). These voids grow as the crack blunts. Note that a blunt crack produces a maximum stress at a distance  $\sim$ twice the CTOD (Crack Tip Opening Displacement) from its tip, while a perfectly sharp brittle crack produces a singularity exactly at its tip.

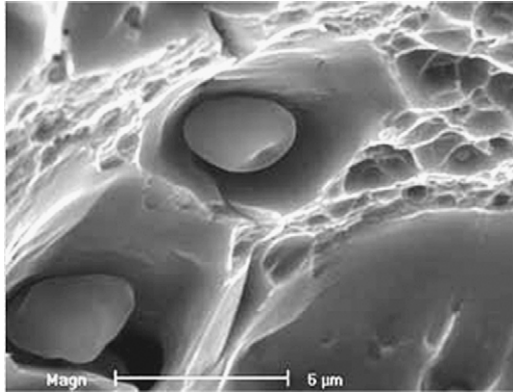


**Fig. 8.** Fracture surface resulting from the ductile failure of an AlSi specimen. Dimples form at the interface between precipitates and matrix (Courtesy C. Prioul).

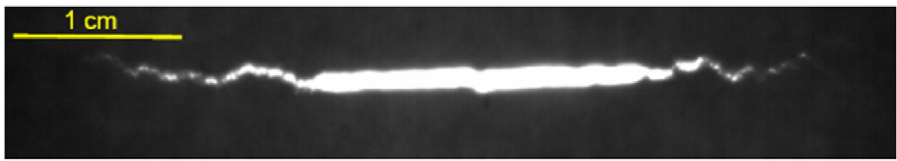


**Fig. 9.** Vicinity of the crack tip in a sheet of paper (Courtesy S. Santucci).

Void nucleation usually takes place within the plastic zone, the extent of which can be estimated by:

$$R_y = \frac{1}{\pi} \left( \frac{K_{lc}}{\sigma_Y} \right) \quad (18)$$

where  $K_{lc}$  and  $\sigma_Y$  denote the fracture toughness and the yield stress respectively.

Usually, the triaxiality is sufficient to ensure crack nucleation, and the critical steps are the growth and the coalescence of cavities, under further plastic strain and hydrostatic stress.

The third main mode of fracture of metals is intergranular failure (see Fig. 6(c)), which often happens when brittle precipitates form at grain boundaries.

### 2.2.3. Quasi-brittle fracture

Contrary to metallic alloys, quasi-brittle materials have poor or no intrinsic plasticity. However, they do undergo damage, and as far as the morphology of cracks is concerned (see Sections 3 and 4), this brittle damage has the same effect as plastic damage. In these quasi-brittle materials – wood, concrete, mortar, some rocks, granite in particular, paper... – microcracks initiate, grow and coalesce ahead of the crack tip, forming a damage zone of macroscopic extension (see Fig. 9 which shows the vicinity of a crack tip in paper). As long as this zone keeps extending, screening of the external stress field increases. This transient increase in resistance is usually called an “ $R$ -curve” behavior, which is depicted in Fig. 10. In Fig. 10(a), the perfectly brittle case is sketched. In this case, the resistance  $R = \Gamma$  (Eq. (1)) does not depend on crack length, while, as stated above,  $G$  varies linearly with  $a$ . Hence, the crack will propagate for a crack length  $a_1$  shorter than  $a_2$  if submitted to a stress  $\sigma_1 > \sigma_2$ .

In the case of multiple cracking ahead of the crack tip (as in the case of plasticity), the only energy spent is not  $2\Gamma$  any longer, and the resistance has to include damage formation. Hence, it increases as long as damage keeps forming, and becomes constant when the damaged zone size has reached its steady value. This case is depicted in Fig. 10(b): (1) for a load  $\sigma_1$  crack propagation starts for a crack length  $a = a_0$ , but a small increase in crack length results into a  $G < R$ . In this case, a small increase in stress would result into a small increase in  $a$ , but the situation remains stable; (2) depicts the critical situation reached when the stress becomes equal to a critical value for which  $a = a_c$ .

The concept of an “ $R$ -curve” is a useful one. However, one must keep in mind that it actually describes a transient state, and that the  $R$ -curve depends on the specimen geometry [43]. As we shall see in Section 3.3.4, this transient regime can actually be seen on the fracture surfaces, leading to a characteristic “anomalous” roughening to be described later.

Unlike in metallic materials where damage takes place within the plastic zone, heterogeneous materials with no intrinsic plasticity form damage (mostly in the form of multiple microcracking) due to large resistance fluctuations. At length scales much larger than the process zone size, such a material can be considered as linear elastic, while within the process zone, damage induces a non-linear elastic behavior.

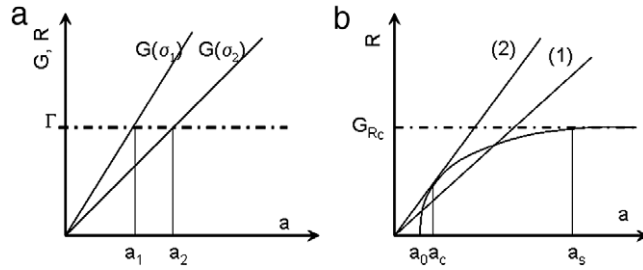


**Fig. 10.** (a) The resistance  $R = \Gamma$  is a constant, independent of crack length  $a$ . (b)  $R$ -curve effect: there is an increase in the resistance as long as the process zone keeps on extending. It reaches its steady value for crack length  $a = a_s$ . (1) Stable situation: for a load  $\sigma_1$ , crack propagation starts for a crack length  $a = a_0$ , but a small increase in crack length results into a  $G < R$ . (2) For a load  $\sigma_2 = \sigma_c$ , the critical situation is reached when the stress is equal to a critical value for which  $a = a_c$ .

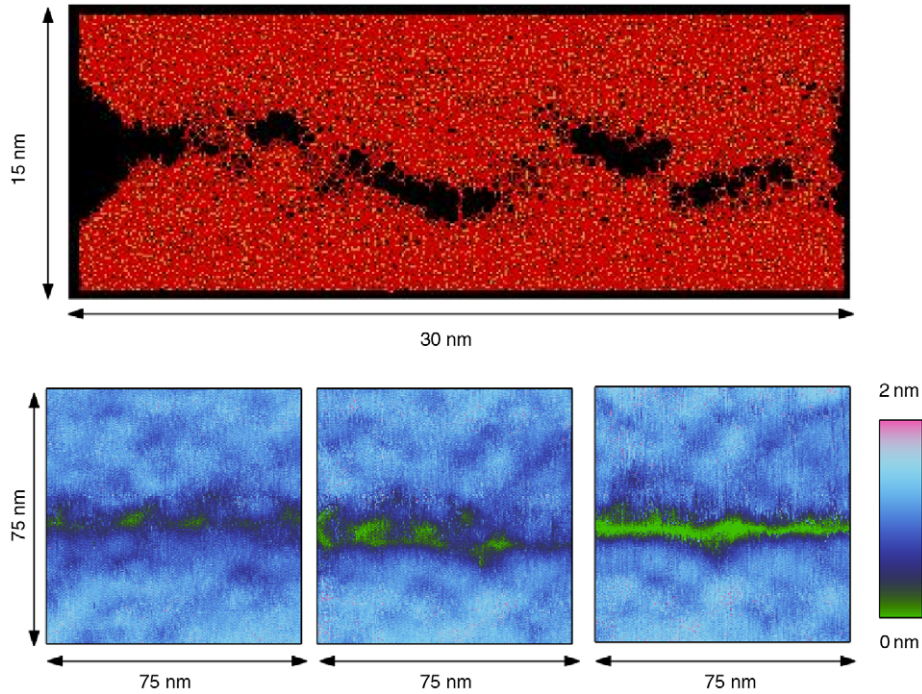


**Fig. 11.** Top: Snapshots of atoms as observed in a MD simulation of dynamic fracture in amorphous Silica (From [45]). Bottom: Sequences of three successive AFM snapshots showing the vicinity of the crack tip at the surface of an aluminosilicate glass specimen (from [7]) In both case, the crack progresses through the growth and coalescence of damage cavities.

#### 2.2.4. Fracture of glass: Brittle or quasi-brittle?

Glass is usually considered as the archetype of elastic materials. However, recent experiments [7,44] and Molecular Dynamics (MD) simulations [45] (see Figs. 11 and 12) have shown that due to its amorphous structure, glass is a quasi-brittle material. As a matter of fact, damage “nano-cracks” have been shown to open ahead of the crack tip. This result is still controversial [46–48]. However, despite the fact that many artifacts can pollute AFM measurements [49,50], it will be argued in the following that this quasi-brittle behavior also leaves a characteristic signature on the fracture surfaces.

### 3. Morphology of fracture profiles

For years, fracture surfaces obtained in three-dimensional materials could not be studied as such, because of the lack of experimental techniques able to provide reliable full three-dimensional data. Even after the development of AFM, stereo reconstruction from SEM images, and good resolution profilometry, the two-dimensional structure function of fracture surfaces was not studied before 2006 [51,52].

In this section, we will summarize the results obtained between 1984 [53] and 2006 [51,52]. They concern intrinsically 1-dimensional structures, especially fracture “profiles” which will be described at length in the following.

The simplest profile is the crack obtained by pulling on a sheet of paper, in a mode I configuration (see Fig. 9).

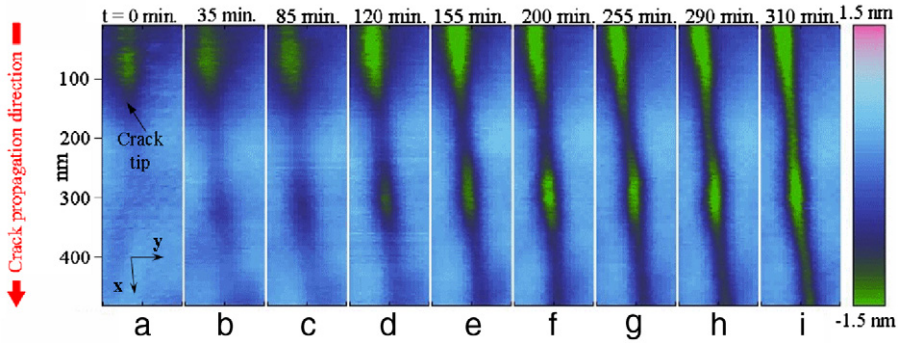


**Fig. 12.** Sequence of topographic AFM frames ( $470 \times 135 \text{ nm}^2$ ) in the vicinity of the crack tip, showing the propagation of a mode I crack along the x-axis. (a), (b) apparition of a nanometric damage cavity ahead of the crack tip, (c)–(f) growth of the cavity prior to crack propagation and (g), (h) coalescence of the cavity with the main crack (i) the crack has advanced through all the observable part of the sample (From [44]).

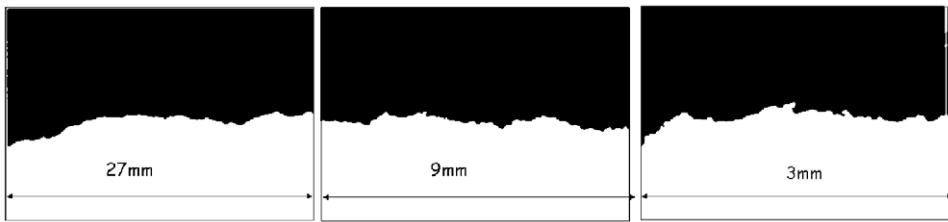


**Fig. 13.** Crack profiles in a sheet of paper observed at three different scales (Courtesy of Kertész et al., from [54]).

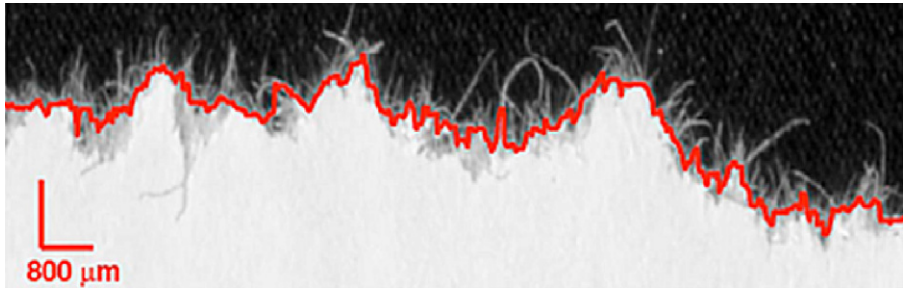


**Fig. 14.** Crack profile in a sheet of fax paper (Courtesy of Santucci et al., from [55]).

### 3.1. Fracture of a paper sheet

The first experiment of that type is due to Kertész and coworkers [54]. Fig. 13 shows such a profile observed at three different magnifications. The scale at which fibers are clearly pulling out of the crack (see Fig. 14) provides a natural limitation for the roughness analysis.

Salminen et al. [56] have used remarkably long samples: their profiles contain 160 000 points, each point corresponding to 0.042 mm. With this resolution, they cannot distinguish individual fiber ends sticking out of the crack line and therefore cannot see the small “overhangs” that the randomly oriented fiber ends create (see Fig. 14). They also note that line branching is moderate, i.e. of the order of 1 short (less than 10 mm) branches are found per 1 m of the backbone of the crack line.

On three different samples, they computed both:

- the second moment of height distributions  $\Delta h(\Delta x)$ :

$$\Delta h(\Delta x) = \langle (h(x + \Delta x) - h(x))^2 \rangle_x^{1/2} \quad (19)$$

where  $\langle \rangle_x$  denotes an average over all possible origins  $x$  of the window of width  $\Delta x$  extending between  $x$  and  $x + \Delta x$ .

- the following quantity:

$$Z_{\max}(\Delta x) = \langle \max\{h(x')\}_{x \leq x' \leq x + \Delta x} - \min\{h(x')\}_{x \leq x' \leq x + \Delta x} \rangle_x \quad (20)$$

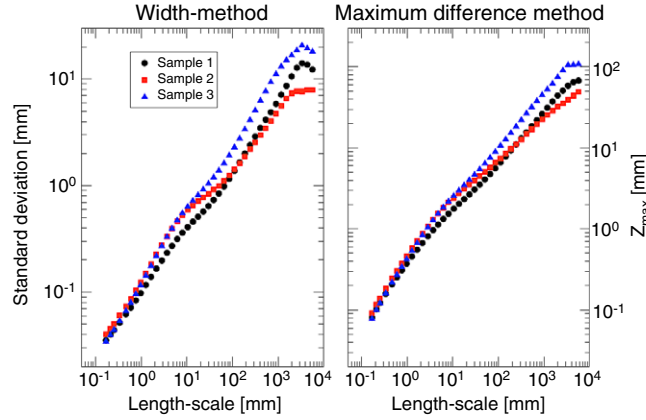


**Fig. 15.** Scaling properties of cracks in sheets of paper as measured using two methods: (a) standard deviation method and (b)  $Z_{\max}$  method. The power-law behavior suggests self-affinity with a roughness exponent  $\beta_{2D} \simeq 0.6$  (Courtesy of Salminen et al., from [56]).

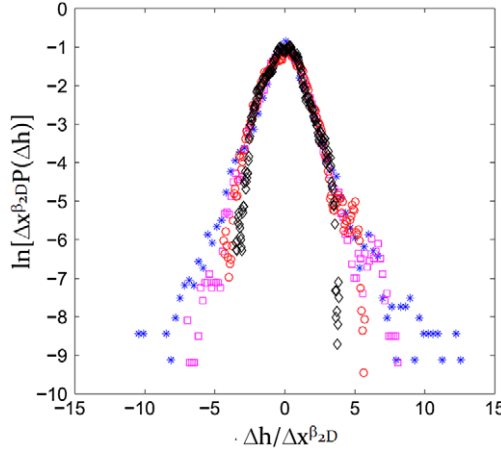


**Fig. 16.** Natural logarithm of the probability density  $P$  of the height increments  $\Delta h$  between two points of the crack line separated by a distance  $\Delta x$ . The different curves (different colors and symbols) correspond to different values of  $\Delta x$ . The rescaling ensures a perfect collapse of the curves in the central region for  $\beta_{2D} = 0.64$  (Courtesy of Bouchbinder et al., from [58]). (For interpretation of the references to colour in this figure legend, the reader is referred to the web version of this article.)

For a self-affine profile, both quantities scale with  $\Delta x$  as  $\Delta x^{\beta_{2D}}$ , where  $\beta_{2D}$  is the roughness exponent. The results of Salminen et al.'s analysis is shown in Fig. 15. The curves all seem to present two regimes, but on average, they suggest self-affinity with exponent  $\beta_{2D} \simeq 0.6$ . A similar value was measured by Santucci et al. [55]. This value is significantly smaller than the one measured by Kertész et al. [54], close to 0.7. Actually, Mallick and coworkers [57] evidenced a drop from  $\beta_{2D} \simeq 0.70$  to  $\beta_{2D} \simeq 0.64$  when the crack goes from subcritical to fast growth in paper sheets.

Salminen et al. [56] have also looked at the distribution  $P(\Delta h)$  of height differences  $\Delta h$ . More recently, Bouchbinder and coworkers [58] have shown that except for the tails of the distribution, one has (Fig. 16):

$$P(\Delta h) = \Delta x^{-\beta_{2D}} f\left(\frac{\Delta h}{\Delta x^{\beta_{2D}}}\right). \quad (21)$$

Santucci et al. [55] confirmed this result, showing that the perfect collapse of the curves (Fig. 16) corresponding to Eq. (21) occurs at length scales larger than  $\Lambda \simeq 800 \mu\text{m}$ , at which secondary cracks and overhangs cannot be distinguished (Fig. 14). At smaller length scales, the crack profiles cease to be self-affine, and present a multi-fractal character. Santucci et al. [55] computed the ratios of the moment of order  $k$  to the moment of order 2:

$$R_k(\Delta x) = \frac{\langle |h(x + \Delta x) - h(x)|^k \rangle^{1/k}}{\langle |h(x + \Delta x) - h(x)|^2 \rangle^{1/2}} \quad (22)$$

and plotted the ratio of  $R_k(\Delta x)$  to the value of the Gaussian ratio  $R_k^G$ :

$$R_k^G = \sqrt{2} \left( \frac{\Gamma(\frac{k+1}{2})}{\sqrt{\pi}} \right) \quad (23)$$

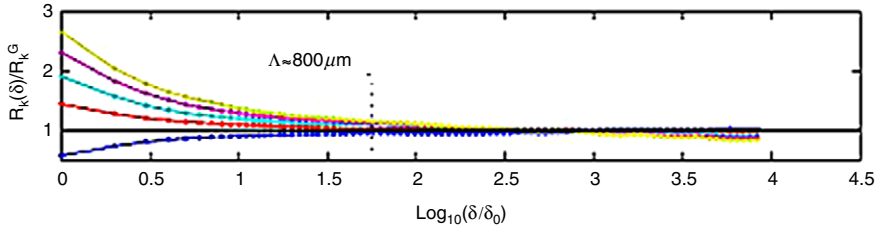


**Fig. 17.** Convergence of the moment ratios  $R_k$  as a function of  $\delta/\delta_0$  towards the Gaussian ratios  $R_k^G$  for the different orders  $k = 1, 2, \dots, 6$ .  $\delta_0$  is the pixel size. For each set, the individual lines visible at small scales, represent from below to above increasing  $k$  values. The various ratios  $R_k$  are averaged over five fracture fronts in paper. The crossover length scale  $A$  is estimated as the scale at which  $|1 - R_k/R_k^G| < 5\%$  for  $k = 1, 3$  (Courtesy of Santucci et al., from [55]).

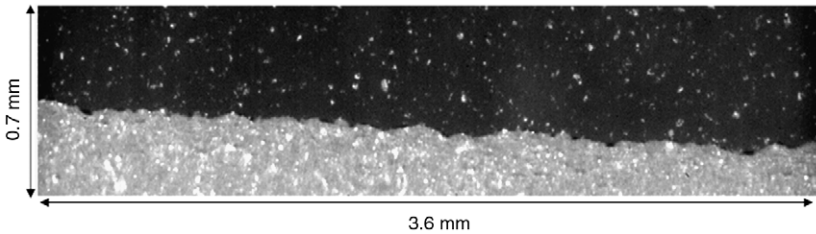


**Fig. 18.** Profile of an interfacial crack propagating along the weak heterogeneous plane between two Plexiglas plates (Courtesy of Måløy et al., from [59]).

as a function of  $\delta = \Delta x$  (see Fig. 17). It can be seen in this figure that  $R_k$  converges to the Gaussian value  $R_k^G$  at length scales larger than  $A$ .

### 3.2. Interfacial fracture

K.J. Måløy and J. Schmittbuhl have set up a very clever experimental system to induce and observe directly a crack progressing along a plane, in a block of polymethylmethacrylate. Fronts are directly observable because of the transparency of the material. The block is made with two plates of Plexiglas that are annealed together at  $\sim 200^\circ\text{C}$  under several bars of normal pressure. The annealing surface corresponds to a weak toughness plane. Before the merging process, random flaws are introduced artificially by sandblasting the surfaces with  $\sim 50 \mu\text{m}$  steel particles. With this surface treatment, the Plexiglas becomes unpolished and loses its transparency. Sandblasting creates height fluctuations which modify the toughness locally and make it fluctuate from place to place.

A mode I crack propagates within the weak sintering plane of the Plexiglas block when the two initial plates are separated with a mechanical press by imposing displacement. Typical crack velocities are within the range of  $10^{-7}$ – $10^{-5} \text{ m s}^{-1}$ . During its propagation, the front is pinned by local regions of higher toughness, and becomes rough. The geometry of the crack front is observed with a microscope mounted on a translation stage equipped with a high resolution digital camera (in its most recent version,  $3871 \times 2692$  pixels) which provides high resolution images. The front is defined as a contrast boundary between the cracked area which appears as nontransparent (i.e., unpolished) and the cracked area which is transparent (i.e., annealed). The kind of contrast obtained is shown in Fig. 18.

#### 3.2.1. Self-affine properties of the crack front

The scaling properties of the observed crack front were analyzed using various methods. For several years, measurements were restricted to relatively small length scales, i.e. below a few hundreds of micrometers. In this range of length scales, a roughness index of  $\zeta_{2D} \simeq 0.6$  was found consistently [22,23]. More recently however, a second self-affine regime characterized by an exponent  $\zeta_{2D} \simeq 0.4$  was shown to exist at larger length scales [60].

The main advantage of the experimental set-up imagined by Måløy and Schmittbuhl is that it allows for a direct observation of the crack dynamics (Fig. 19).

#### 3.2.2. Spatio-temporal evolution: avalanche dynamics

Måløy and coworkers [59] have imagined an original procedure in order to analyze the burst dynamics along the front, and the distribution of local waiting times.

To be able to follow the stable crack front for a long enough time (actually 12 s) and record a large number of images (up to 12 288), they have used a CMOS camera at a spatial resolution of  $1024 \times 512$  pixels, and an acquisition rate of 1000 fps. Experiments have been performed varying the acquisition hardware, the microscope magnification (pixel size of

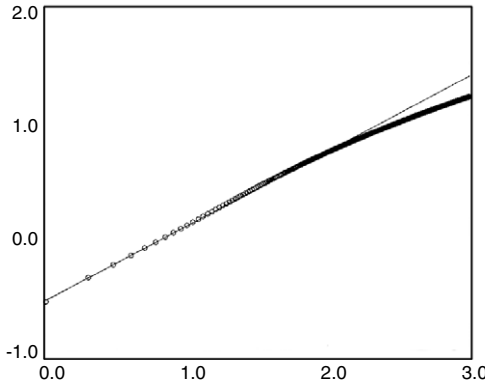


**Fig. 19.** Scaling properties of interfacial cracks propagating along the weak plane between two Plexiglas blocks as measured using the standard deviation method. The power-law behavior suggests self-affinity with a roughness exponent  $\zeta_{2D} \simeq 0.6$  up to a length scale of order  $\sim 200\text{--}250\ \mu\text{m}$  (Courtesy of Delaplace et al., from [23]).

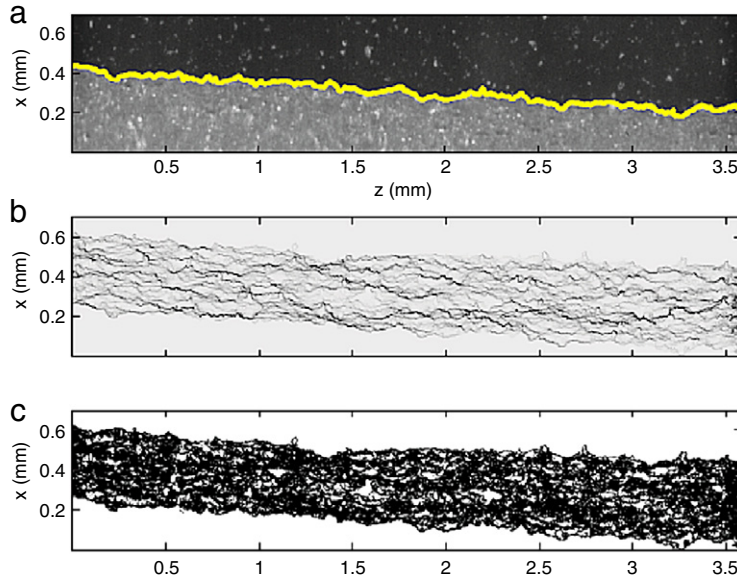


**Fig. 20.** (a) Typical example of a picture recorded by high speed camera during an experiment with an average crack front speed  $\bar{v} = 28.1\ \mu\text{m s}^{-1}$ , and a pixel size  $a = 3.5\ \mu\text{m}$ . The solid line represents the interface separating the uncracked region (in black) from the cracked part. (b) Gray scale map of the waiting time matrix deduced from 10 000 front positions recorded at a rate of 1000 fps. Darker parts show longer waiting times. (c) Spatial distribution of clusters (in white) corresponding to velocities 10 times larger than the average crack front speed (Courtesy of Måløy et al., from [59]).

a few micrometers, smaller than the irregularities due to sandblasting,  $\sim 20\ \mu\text{m}$ , and the average crack propagation speed ( $0.35\text{--}40\ \mu\text{m s}^{-1}$ ).

The fracture front lines extracted from image analysis of the digital pictures (Fig. 20(a)) are added to obtain a waiting time matrix  $W(z, x)$ , which has the dimension of the original image and an initial value equal to zero. If, at time  $t$ , the crack line actually passes through the point of coordinates  $(z, x)$ , then  $W(z, x)$  is incremented by one:  $W_t(z, x) = W_{t-1}(z, x) + 1$ . A gray scale map of the final waiting time matrix is shown in Fig. 20(b). Image recording is fast enough so that there are basically no zeros in the waiting time matrix  $W(z, x)$ . Then, a matrix  $V(z, x)$  of local normal velocities of the interface can be obtained from  $W(z, x)$ :

$$V(z, x) = \frac{1}{W(z, x)} \frac{a}{\delta t} \quad (24)$$

where  $\delta t$  is the time lag between two images.

Finally, Måløy et al. [59] estimated the probability distribution functions of both local waiting times  $w$  and local front velocities  $v$ . The velocity distribution  $P(v/\bar{v})$  is shown in Fig. 21 in a log-log scale. Data corresponding to different experimental conditions (different average crack speeds and different magnifications) collapse on the same master curve, and exhibit a clear power law behavior which will be interpreted in the last section of this review.

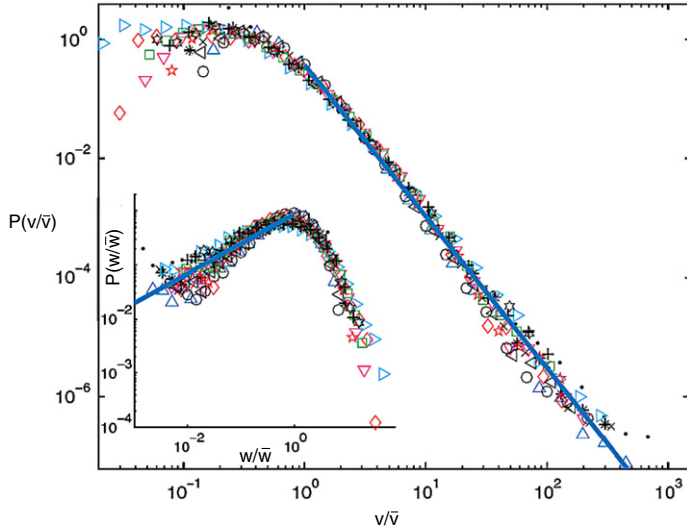


**Fig. 21.** Velocity distribution  $P(v/\bar{v})$  as a function of the rescaled velocity  $v/\bar{v}$  for different experimental conditions. A fit (solid line) to all data for  $v > \bar{v}$  has a slope  $-2.55$ . Inset shows the corresponding waiting time distribution  $P(w/\bar{w})$  as a function of the rescaled waiting time  $w/\bar{w}$ . The solid line is a fit of the data for  $w < \bar{w}$  with a slope  $0.55$  (Courtesy of Måløy et al., from [59]).

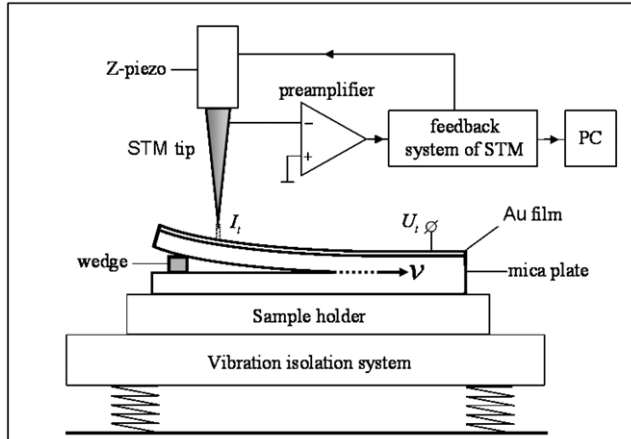


**Fig. 22.** Scheme of the experimental setup. The top surface of the mica plate is coated with a 150 nm-thick gold film to ensure electrical conductivity. The wedge ( $h = 0.25$  mm) is inserted into an initial notch. The vertical displacement of the top part of the mica plate caused by crack propagation is measured by feedback system of the STM (From [61]).

Another attempt to characterize the intermittent dynamics of interfacial crack propagation was proposed by Marchenko et al. [61]. In this work, the feedback system of a Scanning Tunneling Microscope (STM) was used to register fracture events at the nanoscale in mica for moderate loads and crack growth rates. A mica single crystal plate was cleaved by pushing a metallic wedge between the flakes [62]. The top surface of the mica plate was coated with a 150 nm-thick vacuum evaporated gold film to ensure electrical conductivity, so that an STM could be used to register the crack opening displacement during fracture (see Fig. 22). The crack tip position, and hence the crack velocity could be deduced from this measurement.

Two kinds of experiments were performed: (i) the crack was propagated through the ambient humid atmosphere; (ii) a drop of an inert liquid (tetradecane) was put at the crack tip, to prevent any water molecule from reaching it during propagation. The recorded signals were qualitatively different in the two cases, as shown in Fig. 23: while the crack tip position evolved continuously with time in case (i) (Fig. 23(a)), it was shown to progress through successive bursts in case (ii) (Fig. 23(b)). The cumulated probability distribution of crack velocities was also shown to be quite different in the two cases: while this distribution was found to be peaked exponentially when fracture occurred in humid air (i), velocities were shown to be power-law distributed when fracture was performed in a chemically inert n-tetradecane liquid (ii) (Fig. 23(c)). In case (ii), this observation was interpreted as the sign of crack pinning and depinning through bursts, while in case (i), the presence of water molecules induced stress corrosion, i.e. a creep-like steady motion of the crack tip. However, one cannot

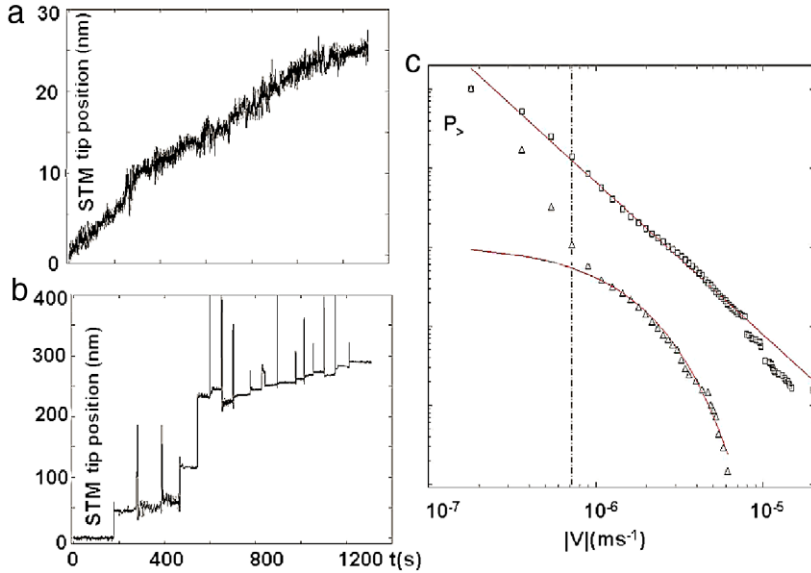


**Fig. 23.** Time variations of the vertical displacement of the STM tip: (a) crack propagation in air; (b) crack propagation in liquid n-tetradecane; (c) Cumulated probability distribution  $P(|v|)$  of the instantaneous velocity  $|v(t)|$  of the crack front in humid air (triangles) and chemically inert n-tetradecane (squares). The plain straight line is a power law fit corresponding to  $P(|v|) \propto |v|^{-2.9}$ . The plain curve line is an exponential fit corresponding to  $P(|v|) = \exp(-|v|/v_0)$ , with  $v_0 \simeq 10^{-6}$  m s<sup>-1</sup>. The vertical dashed line sets the noise level (From [61]).

exclude capillary effects due to the presence of a viscous fluid behind the crack tip, a region were pressure is extremely low [61].

### 3.3. Fracture of a three-dimensional solid

In a three dimensional solid, a meandering crack front leaves behind it a fracture surface composed of rough profiles which are the successive locations of its projection out of the mean fracture plane. These rough profiles have been extensively studied for the last twenty years or so, and the main results will be summarized in the following. Less effort was devoted to the study of the in-plane projection of a three dimensional fracture front, and the only such results we are aware of are summarized hereafter.

#### 3.3.1. In-plane crack roughness

Even in a transparent material, a direct visualization of the propagating 3D front seems to be an impossible task. Hence, the only viable idea was to “mark” the location of the crack front. In order to do so, the crack must be arrested, and the opening must be such that a gas or a liquid can penetrate and reach the front to “color” the fracture surface behind it. This is probably why the only two attempts we know of have been made on metallic alloys [63] for which crack tip plasticity ensures a sufficient opening.

A stable crack was grown in a commercial aluminum alloy and arrested at some point by partial unloading. Indian ink was injected into the crack and the sample was left to dry out before complete fracture was achieved. The resulting fracture surfaces were observed with a Scanning Electron Microscope (SEM) using both a secondary electron contrast and a backscattered electron contrast which enhances differences in the chemical composition. A typical micrograph is shown in Fig. 24. Typical dimples characterizing the unloading and reloading of a crack front in the considered material were observed to follow the frontier of the ink-marked domain. This clearly showed that the observed frontier indeed corresponded to the location of an arrested crack front, and not to a limit of penetration of the ink into the crack. Another experiment performed on a Ti<sub>3</sub>Al-based alloy consisted in oxidizing the sample before complete fracture. The difference in colors between the oxidized and non-oxidized surfaces allowed for a precise location of the arrested crack front in this case also [63]. In both cases, the height correlation analysis revealed a roughness exponent  $\zeta_{in-plane} \simeq 0.55–0.6$ , remarkably close to the roughness exponent measured at small length scales in interfacial fracture. We believe that this similarity is not by chance, and this will be discussed in Section 6.

#### 3.3.2. Out-of-plane roughness: A universal exponent?

The out-of-plane roughness of fracture surfaces was first studied quantitatively by B. Mandelbrot and coworkers [53] on steel. This first experiment, as well as many which followed in the early nineties studied the structure obtained when peaks are eroded. The protocol (sketched in Fig. 25) consists in (i) plating the surface with a different metal (either by vapor deposition [53] or by electro-chemical deposition [64], less directional); (ii) cutting and polishing the plated sample within

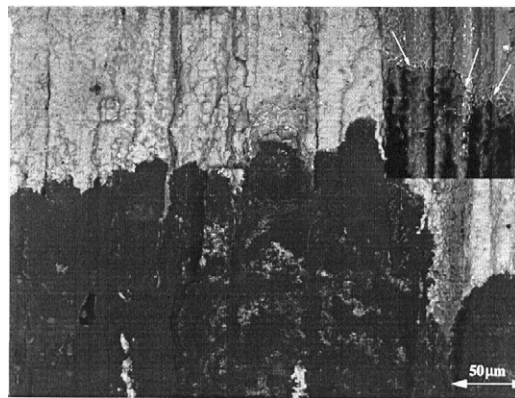


**Fig. 24.** A fracture front marked with Indian ink in the 8090 aluminium alloy, observed with a Scanning Electron Microscope (backscattered-electron contrast). The white arrow on the left indicates the direction of crack propagation (parallel with the length of the very elongated metallurgical grains). Inset: a fracture front marked with Indian ink, observed with a mixed signal (secondary and backscattered electrons) exhibiting dimples (indicated by white arrows) characteristic of an unloaded and reloaded crack front (From [63]).

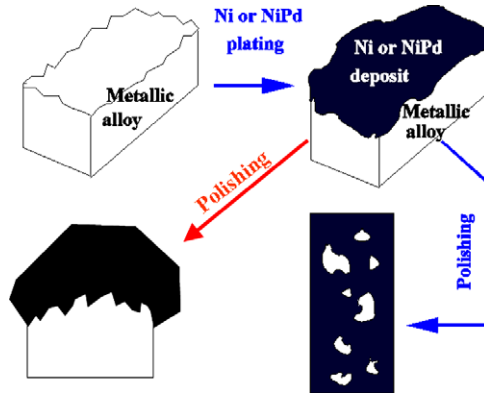


**Fig. 25.** Sketch of samples preparation. The metallic fracture surface is plated with a different alloy, and subsequently polished either within a plane parallel with the surface normal (left) or perpendicular to it (right). In the latter case, “islands” of the studied material appear in a “lake” of the plating alloy, while in the former one, the limit between the material under study and the plating is a fracture profile perpendicular to the direction of crack propagation.

a plane parallel with the mean fracture plane until “islands” of the underlying material appear in an “ocean” of plating; (iii) observing the structure of the islands, or, more precisely, the structure of their frontiers. Fig. 26 shows a SEM image of an aluminum alloy plated with nickel and subsequently eroded [64].

If the surface is isotropic and self-affine, then the ensemble constituted by all the frontiers of the islands is a fractal object with dimension  $d_F = 2 - \zeta$  [65]. Hence, its self-correlation function behaves as  $C(r) \propto r^{-\zeta}$  when averaged over all directions of the polishing plane. This is the method followed in [64] to study four samples made of the same aluminum alloy quenched more or less rapidly. Because a slower quench favors brittle precipitation at grain boundaries, fracture becomes more intergranular and the fracture toughness decreases. Although the four studied samples had fracture toughnesses ranging from 28 to 45 MPa $\sqrt{m}$ , no significant or systematic variation in  $\zeta$  could be observed, and we suggested that  $\zeta \sim 0.8$  might be a *universal* value, i.e. independent of the fracture mechanism and of the microstructure.

After a few pioneering experiments, fracture profiles – mostly perpendicular to the direction of crack propagation – were studied, with various techniques. By using a profilometer, Måløy and coworkers [66] studied six different brittle materials and showed that, within error bars,  $\zeta$  was constant, and that its value was very close to 0.8, as reported for the aluminum alloy studied in [64] and the steel studied in [53]. Fig. 27 shows the power spectra  $P(f)$  as a function of the frequency  $f$  for the six materials.

Metallic fracture profiles were observed mostly with SEM after the surface was plated and subsequently cut and polished within a plane perpendicular to the mean crack plane (Figs. 25 and 28), and sometimes with a combined use of SEM and AFM [67,68].

In two cases, the observed scaling domain was observed to span over five decades of length scales. Fracture profiles of a Ti<sub>3</sub>Al-based alloy [68] were shown to exhibit a roughness exponent  $\zeta \simeq 0.78$  within a scaling domain ranging from 5 nm to 0.5 mm. Let us note that in this case, 5 nm is the AFM resolution, while 0.5 mm is very close to the grain size. Fracture profiles



**Fig. 26.** “Islands” of aluminum alloy appear in dark within a light “ocean” of nickel.

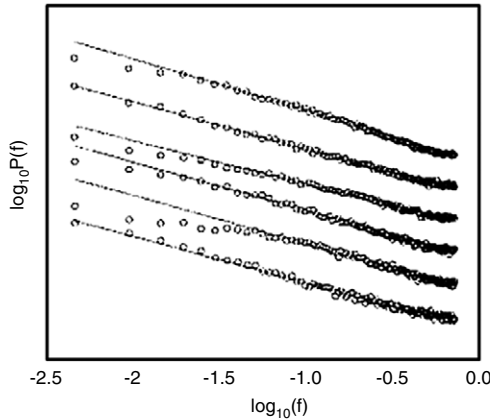


**Fig. 27.**  $\log_{10}$  of the power spectrum  $P(f)$  is plotted against  $\log_{10}$  of the frequency  $f$ . For a self-affine profile,  $P(f) \propto f^{-1-\zeta}$ . The fact that all the lines are parallel shows that  $\zeta$  does not depend on the material. As a matter of fact,  $\zeta \sim 0.8$  fits all the data quite well (Courtesy of Måløy, from [66]).

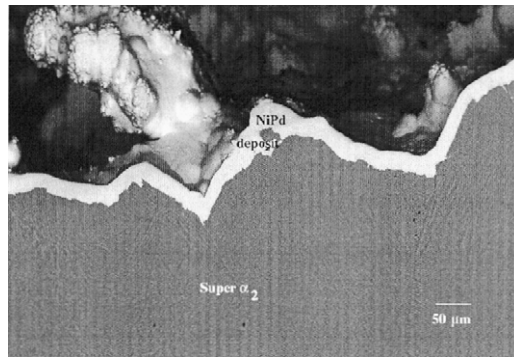


**Fig. 28.** A fracture profile (perpendicular to the direction of crack propagation) in a  $Ti_3Al$ -based alloy. The fracture surface is plated with NiPd. The deposit appears in very light gray above the alloy.

of an aluminum alloy [69] plated with nickel and observed with SEM were also shown to be characterized by a roughness index  $\zeta \simeq 0.77$  for length scales between 5 nm and 0.1 mm (see Fig. 29).

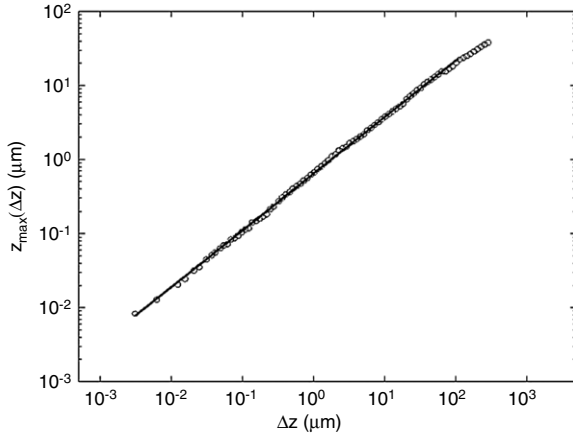


**Fig. 29.**  $Z_{\max}(\Delta z)$  (Eq. (20)) as a function of  $\delta z$ , on a log–log plot. The best fit is a single power law with exponent 0.77.

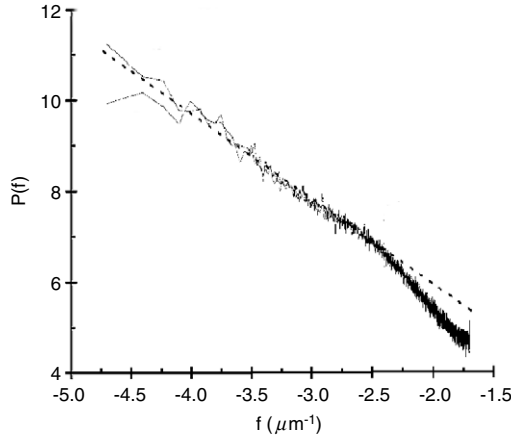


**Fig. 30.** Averaged power spectra computed from 20 profiles of 2048 points (the frequency  $f$  is expressed in  $\mu\text{m}^{-1}$ ). The roughness exponent found fitting the data in the low frequency part of the spectrum – i.e. at length scales larger than  $\sim 300 \mu\text{m}$ , which is of the order of the grain size – is equal to  $\zeta = 0.45$ . The two curves correspond to crack velocities  $5 \times 10^{-2} \text{ m/s}$  and  $3 \times 10^{-4} \text{ m/s}$  (Courtesy of Boffa et al. [72]).

Fracture surfaces of silicate glasses, the height of which fluctuates of a few nanometers over a few micrometers (they are flat on optical scales in the so-called “mirror zone”), were studied using Atomic Force Microscopy (AFM). They were shown to exhibit the same scaling behavior with exponent  $\zeta \simeq 0.8$  [67,68], but only up to a length scale of order  $\sim 100 \text{ nm}$ .

Rocks have also been extensively studied: J. Schmittbuhl and collaborators have looked at the fracture surfaces of granite with a mechanical profilometer [70] and found a scaling domain extending up to a few millimeters, characterized by a roughness exponent  $\zeta \simeq 0.8$ . However, some rocks, such as sandstone, were shown to exhibit roughness exponents significantly smaller than 0.8.

### 3.3.3. Exceptions: Small exponents

Boffa and coworkers [71,72] used a technique based on the measure of the length distribution of the shadows appearing under grazing illumination to show that although basalt fracture surfaces are self-affine with exponent  $\zeta \simeq 0.8$ , sandstone fracture surfaces actually exhibit a significantly smaller roughness index,  $\zeta \simeq 0.45$  (see Fig. 30).

Such a small exponent has since then been observed on another material [73–75], as shown in Section 4. It is interesting to see that this small exponent is measured in the case of sandstone, while the exponent measured on granite fracture surfaces [70] is close to 0.8. It will be argued in the following that the smaller exponent characterizes a rough crack in an elastic material, while the larger one corresponds to measurements within the FPZ: while sandstone can be considered as elastic at length scales larger than the grain size – precisely the domain where roughness measurements are performed –, granite fails in a quasi-brittle way at the scale of observations. And as a matter of fact, the transient roughening regime described hereafter in Section 3.3.4, which is observable only on quasi-brittle materials because of the large size of their FPZ, has been analyzed first in the case of granite [76].

The various measurements quoted up to now in this section are summarized in Table 1 in Section 4.

**Table 1**

Table of roughness exponents, measured by probing intrinsically one dimensional objects such as crack fronts, crack profiles or iso-level lines. This is a non-exhaustive list and other references can be found in [84,97].

Geometry	Probed objects	Material	Exponent	Scales	Refs.
Thin sheet	Crack lines	Paper	$\beta_{2D} = 0.6\text{--}0.7$	1 mm–1 m	[54,56,55]
			Multiaffine	$\leq 1 \text{ mm}$	[58,55]
Interfacial	Crack lines	PMMA	$\zeta' = 0.4$	$\geq 50 \mu\text{m}^a$	[55]
			$\zeta' = 0.6$	$\leq 50 \mu\text{m}^a$	[23,59]
3D in-plane 3D out-of-plane	Profiles	Al-, Ti- alloys	$\zeta' = 0.6$		[63]
	Level lines	Al-alloy	$\zeta = 0.8$	$\leq 100 \mu\text{m}$	[64,84]
	Profiles along front	Ti <sub>3</sub> Al-alloy	$\zeta = 0.78$	5 nm–0.5 mm <sup>b</sup>	[67,68]
		Al-alloy	$\zeta = 0.77$	3 nm–0.1 mm <sup>b</sup>	[69]
	Brittle solids	Brittle solids	$\zeta = 0.8$		[66]
		Mortar	$\zeta = 0.8$		[85]
	Steel	$\zeta = 0.4$	$\leq 1 \text{ mm}$		[93]
		$\zeta = 0.8$	$\geq 1 \text{ mm}$		
	Granite	$\zeta = 0.8$	$\sim 1\text{--}16 \mu\text{m}$ to 1 mm <sup>c</sup>		[94]
		$\zeta = 0.78\text{--}0.85$			[95]
	Glass	$\zeta = 0.8$	$\leq \sim 100 \text{ nm}$		[67,68,44]
	Phase-separated glasses	$\zeta = 0.8$	$\leq \text{grain size}$		[96]
		Logarithmic	$\geq \text{grain size}$		[96]
	Sintered glass	$\zeta = 0.4$	$\geq \text{grain size}$		[73]
	Sandstone	$\zeta = 0.4\text{--}0.5$			[71,72,75]

<sup>a</sup> Interfacial failure: 50 μm corresponds to the size of heterogeneities introduced within the PMMA by sandblasting the surfaces.

<sup>b</sup> Metallic alloys: the upper limit of the scaling domain is of the order of the size of the metallurgical grain, which represents the largest heterogeneity in this case.

<sup>c</sup> Steel: the upper limit of the 0.8 scaling domain depends on temperature, following the evolution of the plastic zone size.

Note that this small exponent should not be confused with the roughness exponent close to 0.5 which was observed at small length scales on metallic fracture surfaces as well as on fracture surfaces of float glass, which contains sodium [77,67,68]. We believe (see Section 6) that the two exponents might have different origins. The crossover between the “0.5-small scales” and the “0.8-large scales” regimes [68] was shown to decrease with the mean crack velocity  $V$  as  $1/V$ , and subsequently interpreted as the size of damage cavities or cracks. More recently [78], fracture surfaces of a Zr-based metallic glass were shown to exhibit also a roughness exponent close to 0.5: in this case, fracture was shown to occur as the coalescence of neighboring damage cavities. In this case, the fracture surfaces are isotropic, and they reveal a strong multifractal character observed first on branched fracture surfaces in polycrystalline Ni<sub>3</sub>Al [79].

Finally, the evolution of an initial straight notch into a rough crack front was also studied. This transient regime, which results in particular into the “R-curve” behavior, has already been discussed for quasi-brittle fracture in Section 2.2.3. As long as the FPZ keeps on extending, the morphology of the crack keeps evolving until it reaches its steady rough state.

### 3.3.4. Transient regime: From a straight notch to a rough front

Several experiments were actually performed on wood. While Engøy and coworkers [80] observed a roughness index close to 0.7 along profiles perpendicular to the direction of crack propagation which was also in this case, the direction of the fibers, S.Morel and collaborators [81–83] always reported a roughness index closer to the widely observed 0.8 [84]. However, S. Morel et al. mostly focused on the transient regime corresponding to the development of the FPZ. In order to understand how a straight notch becomes a rough crack, they analyzed the evolution of the morphology of profiles perpendicular to the direction of crack propagation with their distance to the initial notch. It has been found on several species of wood [81–83], on granite [76] and on mortar [85] that the upper bound of the “0.8” regime,  $\xi(x)$  depends on the distance  $x$  of the considered profile to the initial straight notch as a power law. Hence, two different exponents are needed to describe height fluctuations in this transient regime: one is what we have defined up to now as the roughness exponent, 0.8, and was renamed *local* roughness exponent in this context; the other one characterizes the evolution of  $\xi(x)$  with  $x$  and is called the *global* roughness exponent  $\zeta_{\text{global}}$ . Height fluctuations  $\Delta h(l)$  estimated over a window of size  $l$  along the  $z$  axis and at a distance  $x$  from the initial notch are said to exhibit *anomalous* scaling properties:

$$\Delta h(l, x) \simeq A \begin{cases} l^\zeta \xi(x)^{\zeta_{\text{global}} - \zeta} & \text{if } l \ll \xi(x) \\ \xi(x)^\zeta & \text{if } l \gg \xi(x) \end{cases} \quad (25)$$

where  $\xi(x) = Bx^{1/\kappa}$  depends on the distance  $x$  to the initial notch and characterizes the crossover length along the  $z$  axis. For length scales smaller than  $\xi(x)$ , the surface is self-affine, and characterized by the local roughness exponent  $\zeta \simeq 0.8$ .

In this case, the amplitude of roughness increases as a function of  $x$  until the self-affine correlation length  $\xi(x)$  reaches the system size  $L$ . This happens at a certain distance  $x_{\text{sat}} = (L/B)^\kappa$  from the notch:  $\xi(x \gg x_{\text{sat}}) = L$ . Thus, the first growth regime (i.e. for  $x \ll x_{\text{sat}}$ ) is followed by a stationary regime (for  $x \gg x_{\text{sat}}$ ) where the roughness amplitude remains constant and where the global roughness (i.e. measured over the system size  $L$ ) is driven by the *global* roughness exponent  $\zeta_{\text{global}}$ :  $\Delta h(L, x \gg x_{\text{sat}}) \sim L^{\zeta_{\text{global}}}$ . The main consequence of an anomalous scaling is that, in this saturation regime, the magnitude

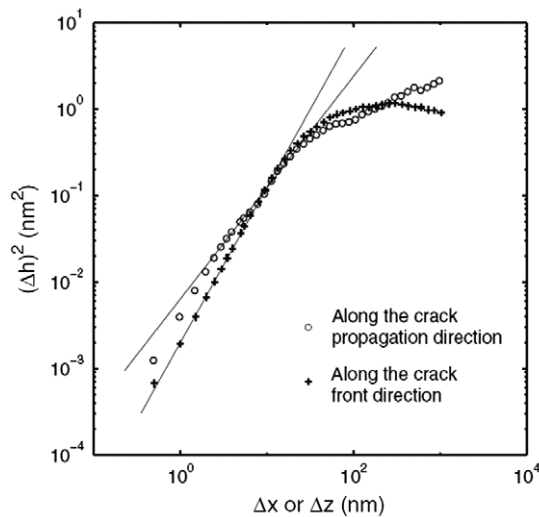


**Fig. 31.** Height-height correlation function calculated along the propagation direction and the crack front direction on a fracture surface of silica glass (crack velocity  $10^{-11} \text{ ms}^{-1}$ ). The straight lines are power law fits with exponents  $\zeta \simeq 0.8$  along the crack front direction (+) and  $\beta \simeq 0.6$  along the direction of crack propagation (o) (From [52]).

of the local roughness (i.e. measured on windows  $l \ll L$ ) is not only a function of the window size but also of the system size  $L$ :  $\Delta h(l, x \gg x_{\text{sat}}) \sim l^\zeta L^{\zeta_{\text{global}} - \zeta}$ . A more “classical” Family-Vicsek type of scaling would correspond to:  $\zeta_{\text{global}} = \zeta$ .

This does not seem to be the case for granite and for wood. Furthermore, unlike the “local” roughness index 0.8, the global roughness exponent is material-dependent, and a value  $\zeta_{\text{global}} = 1.2$  was reported for granite [76], while  $\zeta_{\text{global}} = 1.35$  and 1.60 for pine and spruce respectively were measured by Morel et al. [81]. Note that the so-called dynamic exponent  $\kappa$ , as well as the prefactors  $A$  and  $B$  seem also to be material-dependent. More recently, it has been shown that for mortar [85], one has  $\zeta \simeq 0.77$ ,  $\zeta_{\text{global}} \simeq 1.3$ , and  $\kappa \simeq 4.7$ , with a crossover length (upper bound of the scaling domain) at saturation  $\xi_{\text{sat}} \simeq 10.7 \text{ mm}$ .

#### 4. Morphology of fracture surfaces

Only recently was the full structure function of fracture surfaces computed for various materials. This was made possible by the development of several experimental techniques which allow one to go beyond the study of single profiles. Interest for the two-dimensional structure of fracture surfaces was triggered mostly by the idea that line models (see Section 6) could be relevant in the case of fracture, as suggested first by Bouchaud et al. [86]. These models suggest in particular an anisotropy of the surface produced by the growth of a front. Such anisotropy was observed on the fracture surfaces of an aluminum alloy and of amorphous silica.

##### 4.1. Anisotropy of fracture surfaces

Fracture surfaces of the commercial 7475 aluminum alloy were obtained from compact tension specimens first precracked in fatigue. In the tensile fracture zone, the fracture surface has been observed with an SEM at two tilt angles. A high resolution elevation map has been produced from the stereo pair using the cross-correlation-based surface reconstruction technique described in [87]. The reconstructed image of the topography represents a rectangular field of  $565 \mu\text{m} \times 405 \mu\text{m}$  (512 by 512 pixels).

On the other hand, stress corrosion fracture of pure amorphous silica samples was performed in controlled conditions in order to obtain mean crack velocities [7,88] ranging from  $10^{-11}$  to  $10^{-6} \text{ m/s}$ . The topography of the resulting fracture surfaces was then determined with an AFM. To ensure that there was no bias due to the scanning direction of the AFM tip, each image was scanned in two perpendicular directions, and the analyses presented hereafter were performed on both images. These images represent a square field of  $1 \mu\text{m}^2$  (1024 by 1024 pixels).

In both cases, height fluctuations along profiles parallel with the direction  $x$  of crack propagation and perpendicular to it ( $z$  direction) were analyzed and shown to scale quite differently.  $\Delta h(\Delta x)$  and  $\Delta h(\Delta z)$  are plotted against  $\Delta x$  and  $\Delta z$  in Figs. 31 and 32 for silica and the 7475 aluminum alloy respectively. In both cases, the best fits are power laws for  $\Delta h(\Delta x)$  and  $\Delta h(\Delta z)$ ; but if along the  $z$  axis, an exponent  $\zeta \simeq 0.8$  is recovered, as expected, a significantly smaller exponent  $\beta \simeq 0.6$  is observed along the  $x$  axis.

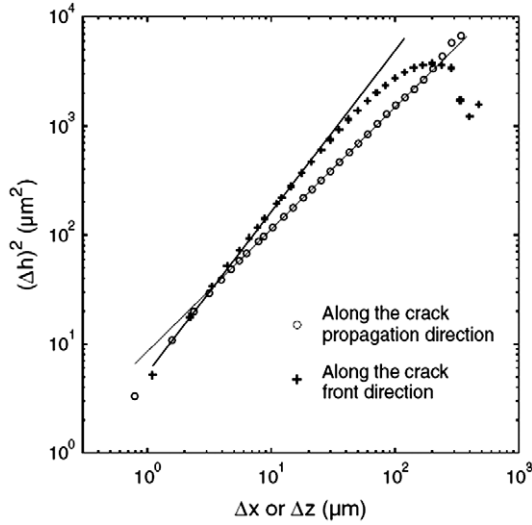


**Fig. 32.** Same for the 7475 aluminum alloy (velocity is not measured) (From [52]).

#### 4.1.1. Two-dimensional structure function

This anisotropy led us to determine the full two-dimensional structure function:

$$\Delta h(\Delta z, \Delta x) = \langle (h(z + \Delta z, x + \Delta x) - h(z, x))^2 \rangle_{z,x}. \quad (26)$$

This quantity being a function of two variables,  $\Delta x$  and  $\Delta z$ , it can be plotted for example as a function of  $\Delta z$  for various fixed values of  $\Delta x$ : these curves can be seen in the inset of Fig. 33. One can make them all collapse on the same master curve by dividing  $\Delta h$  and  $\Delta z$  by  $\Delta x^\beta$  and by  $\Delta x^{1/\kappa}$ , with a good choice of exponents  $\beta$  and  $\kappa$ . This means of course that  $\Delta h(\Delta z, \Delta x)$  obeys the following scaling law:

$$\Delta h(\Delta z, \Delta x) = \Delta x^\beta f\left(\frac{\Delta z}{\Delta x^{1/\kappa}}\right). \quad (27)$$

If  $\Delta z$  tends to zero, then we want to recover the 1D structure function corresponding to profiles parallel with the  $x$  axis, hence we know that  $f(u)$  has to tend to a constant when  $u$  tends to 0. In the same way, we want  $\Delta h(\Delta z, \Delta x = 0) \propto \Delta z^\zeta$ . Hence  $f(u) \sim u^\zeta$  when  $u \gg 1$ , and the exponent  $\kappa$  must be equal to:

$$\kappa = \frac{\zeta}{\beta}. \quad (28)$$

This specific scaling is the so-called Family–Vicsek scaling [89].

The same kind of scaling, involving the same exponents  $\zeta \simeq 0.75$ ,  $\beta \simeq 0.6$  and  $\kappa = \zeta/\beta \simeq 1.25$  has been observed for other materials: pure amorphous silica [52] for crack velocities ranging from  $10^{-11}$  to  $10^{-6} \text{ ms}^{-1}$ , mortar [51] within the steady-state regime, and quasi-crystals [90]. Despite the similarity in the structure functions, scaling is observed at very different length scales, depending on the material: typically over a range 1–100  $\mu\text{m}$  for the metallic alloy, 1–100 nm for silica [52], 0.1–10 mm for mortar [85,51], and 0.1 Å–3 nm for an i-AlPdMn quasi-crystal [90].

In order to compare the structure functions despite these huge differences in length scales, Ponson and collaborators [90] rescaled  $\Delta x$  and  $\Delta z$  to the surface topographies  $\ell_x$  and  $\ell_z$  respectively.  $\ell_x$  and  $\ell_z$  are the typical distances at which the local slopes along a profile parallel with the  $x$  or to the  $z$  axis respectively become of order unity. Eq. (27) then writes:

$$\Delta h(\Delta z, \Delta x) = \ell_x \left( \frac{\Delta x}{\ell_x} \right)^\beta f\left( \frac{\Delta z/\ell_z}{(\Delta x/\ell_x)^{1/\kappa}} \right). \quad (29)$$

When this rescaling is done, all the curves relative to different materials collapse on the same master curve, as shown in Fig. 34.

This result strongly suggests the universality of the structure function, and, as we will see in Section 6, the relevance of models of elastic lines pulled through randomly distributed obstacles. This universality was however questioned recently by Bouchbinder and coworkers [91], who proposed that the anisotropy evidenced by Ponson et al. [52] is entirely due to the breaking of isotropy by the initial conditions (long notch, or precrack). Their analysis, which mixes the parallel and perpendicular scaling regimes and exponents, results quite naturally in measuring nonuniversal apparent exponents. A study in progress seems to indicate that in brittle fracture, even when cylindrical samples with no notch are broken in tension, the fracture surfaces exhibit anisotropy: exponents  $\beta \sim 0.6$  and  $\zeta \sim 0.8$  are measured on profiles which lie along

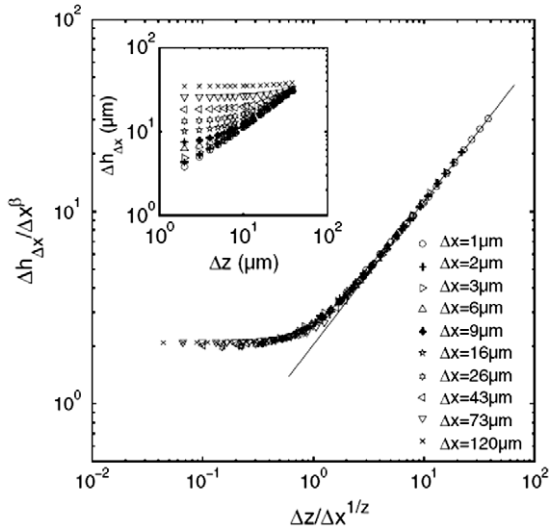


**Fig. 33.** Aluminum alloy. The inset shows  $\Delta h(\Delta z, \Delta x)$  plotted against  $\Delta z$ : the various curves correspond to different values of  $\Delta x$ . The data collapse was obtained by dividing  $\Delta h$  and  $\Delta z$  by  $\Delta x^\beta$  and by  $\Delta x^{1/\kappa}$ , using the values:  $\kappa = 1.26$  and  $\beta = 0.58$ , hence  $\zeta = 0.75$  (From [52]).

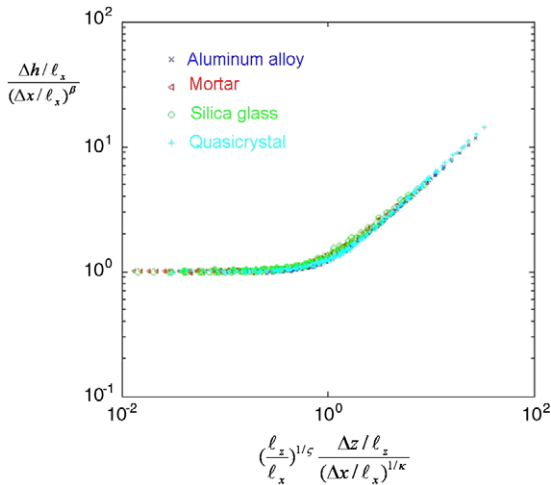


**Fig. 34.** Scaling function  $f(u)$  measured on four different materials, glass, metallic alloy, and mortar (From [90]).

two perpendicular directions [92]. This might be due to the overtaking of one of the damage penny shape cracks over the others: the largest crack leading to complete failure then imposes its direction of propagation. Things might be very different in ductile fracture, as was observed in [78].

As already mentioned in the previous section, materials such as sintered glass [73] or sandstone [71,73] exhibit a roughness index  $\zeta \simeq 0.5$ , significantly smaller than the value  $\zeta \simeq 0.8$  quoted above. These fracture surfaces were shown to exhibit little anisotropy, but the same type of structure function.

#### 4.1.2. Two classes of universality

Ponson and coworkers [74] actually analyzed the structure function of fracture surfaces of sintered glass beads [73] and Fontainebleau sandstone [75]. A Family–Vicsek type of collapse is obtained for sintered glass beads with different diameters and porosities, when the following set of exponents is chosen:  $\zeta = 0.40$ ,  $\beta = 0.49$ , and hence  $\kappa = 0.81$  (see Fig. 35).

Actually, sintered glass and sandstone seem to define a second universality class: for these materials, the structure function exhibits the same type of Family–Vicsek scaling, but with a different set of exponents. Let us however recall that these observations are performed at a scale larger than the grain size in all these cases. At this scale, both kinds of material can be considered as perfectly elastic. For what concerns the sintered glass, where both the grain boundaries and the grain interiors are vitreous, damage may not occur at scales larger than a few hundreds of nanometers, as shown in Section 2.2.4. for silicate glasses: this scale is orders of magnitude smaller than the considered grain size. In Section 6, when discussing

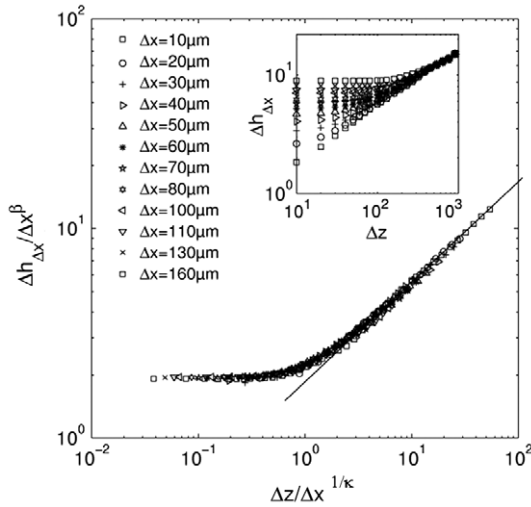


**Fig. 35.** Scaling function  $f(u)$  measured for a bead diameter of 120  $\mu\text{m}$  and a porosity of 26% (Courtesy of Laurent Ponson [74]).

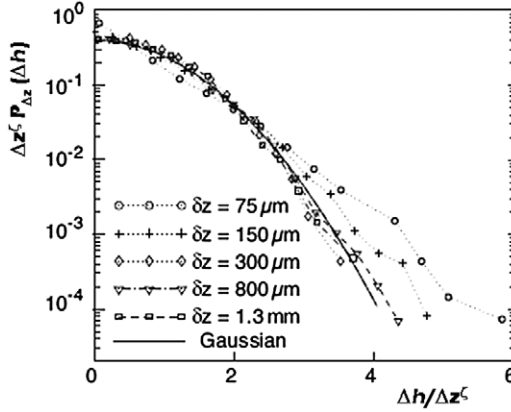


**Fig. 36.** Probability density  $P_{\Delta z}(u)$ , where  $P_{\Delta z}$  is the rescaled probability distribution function  $P$  of height differences:  $P_{\Delta z}(\Delta h) = \Delta z^{-\zeta} P(\Delta h/\Delta z^\zeta)$ , in a semilogarithmic representation for  $75 \mu\text{m} \leq \Delta z \leq 1.3 \text{ mm}$ . Here  $u = \frac{\Delta h}{\ell} \left(\frac{\ell}{\Delta z}\right)^\zeta$ , with  $\ell = 35 \mu\text{m}$  and  $\zeta = 0.43$ . For clarity, only positive  $u$  are displayed. Continuous line: Gaussian distribution  $\frac{1}{\sqrt{2\pi}} \exp^{-x^2/2}$  (Courtesy of Laurent Ponson [74]).

models, we will come back to this assumption of two universality classes, one arising at scales such that the material can be considered to be linear elastic, and the other one corresponding to scales smaller than the FPZ size. Table 2 below summarizes the observations reported in both cases.

Finally, it is worth noticing that although they seem to belong to different universality classes, the probability distribution of height differences is perfectly Gaussian both in silica glass, in sintered glass and in sandstone [74,75] (see Fig. 36). How the probability distribution differs from a Gaussian for other materials when studied within the FPZ should provide interesting clues for further modeling.

In order to explain this rich variety of morphologies, which however seem to fit in well defined universality classes, several models have been imagined. The common characteristic of the very different models that we are now going to describe is that they include explicitly the disordered nature of materials. However, before discussing the various models, we summarize in the table below the various roughness exponents measured on cracks and on fracture surfaces.

## 5. Statistical models of fracture

Several types of statistical models, aiming at modeling failure of heterogeneous materials at various length and time scales have been built in order to go beyond mean field descriptions. In this section, we will briefly describe the most commonly used, insisting on their successes and limitations.

Molecular Dynamics (MD) simulations have been proposed in order to take into account the structure of materials at a near-atomic scale. The greatest success of these models resides in providing a detailed description of fracture and

**Table 2**

Table of roughness exponents, measured by analyzing the full structure of fracture surfaces.

Material	$\zeta$	$\beta$	Scales	Refs.
Quasicrystal	0.76	0.65	0.6 Å–2.5 nm	[90]
Silica	0.77	0.61	1–100 nm	[52,51]
Al-based alloy	0.75	0.58	0.1–300 μm	[52,51]
Mortar	0.71	0.59	50 μm–~1 mm	[51]

damage spreading mechanisms at this scale, which are usually impossible to observe experimentally. Furthermore, they also help understanding the origin of stress heterogeneities which control these mechanisms, and are essentially linked to the amorphous structure of the considered materials.

### 5.1. Molecular dynamics simulations

The principle of MD simulations is to follow the trajectory of each atom by solving Newton's law in classical mechanics. Because of their very nature, these simulations are run in parallel. At each time step – of the order of one femto-second – the position and the velocity of each atom are recorded, as well as the force acting on it. Because it represents a huge amount of information and elementary calculations, these simulations are restricted both in space and time. Hence they are generally used to describe the fracture of materials which are disordered on the nanometer scale, i.e. to amorphous materials, for which they have been extremely successful. The size of the systems as well as the length of the simulations (1 ns is nowadays what can be reached) depend obviously on the characteristics of the computer used, on algorithmic performance, but also on the type of interatomic potential.

The crucial ingredients of these models are indeed the interatomic potentials. The simplest two-body interatomic potential is the widely used Lennard-Jones (LJ) interaction potential, which consists of a hard sphere repulsion at small distance and of an attractive part exhibiting a minimum for a given interparticle distance.

#### 5.1.1. Fracture of bidimensional Lennard-Jones glasses

LJ potentials in two dimensions are not aimed at describing in detail real materials, but rather at retaining the essential features of non-crystalline solids. To avoid crystallization, one has to consider at least two types of particles.

Although rather simple, LJ potentials have been shown to be able to reproduce a huge variety of material behaviors. Falk [98] has compared the fracture behavior of systems using either the classical LJ potential or a variation of it. He has shown that both brittle and ductile behaviors can be recovered. With the slightly modified LJ potential, cracks remain atomically sharp, and progress through successive breaking of bonds at their tips, while with the classical LJ, the crack tip blunts significantly. In this simulation, the stress remains high while voids nucleate ahead of the tip (see Fig. 37). This is very close to what has been observed in some AFM experiments [7,88,44] briefly described in Section 2.2.4.

But although AFM experiments are far from having the spatial resolution required to understand the origin of damage formation, MD simulations can provide a detailed description of the mechanisms involved. Structural rearrangements, which typically occur at a very low rate in amorphous systems, have been shown [99,100] to arise as a response of the glass to an externally applied shear. Because the structure is amorphous, even the stress field produced by a purely mode I crack may induce local shear stresses, and, as a result, trigger structural reorganizations. It has been shown in Falk's simulations [101,98] that some groups of molecules move in ways that cannot be described by linear strain tensors. These rearrangements are localized: small regions that Argon [102] first referred to as "shear transformation zones" (STZs) deform in the direction of the applied shear stress. Once deformed, these regions are deactivated; that is, they are "jammed" and cannot deform further in the same direction, but they can return to their previous orientations when the stress is reversed. In mode I fracture, STZs may cause a directional bias in the structural rearrangements and produce macroscopic strains, which, in turn, affect the characteristics of crack propagation.

In order to identify these local rearrangements from a set of molecular positions and subsequent displacements, Falk [101] proposes to compute the closest possible approximation to a local strain tensor, in the neighborhood of any particular molecule. The local strain is determined by minimizing the mean square difference between the actual displacements of the neighboring molecules relative to the central one, and the relative displacements that they would have if they were in a region of uniform strain. These heterogeneous deformations are shown in Fig. 37, where dark regions have undergone the highest amount of non-affine rearrangement.

LJ glasses have also been used by Leonforte et al. [5] to study the stress and strain fields due to a point source force acting on a bidimensional amorphous material. They demonstrate that the average stresses and displacement fields compare well with the predictions from classical isotropic elasticity, and this already for small distances from the source and for small system sizes. Contrasting to this, large stress (and, hence, strain) fluctuations are found to decrease exponentially with distance, up to surprisingly large length scales,  $\approx 30$  atomic sizes. These stress and strain fluctuations might be interpreted as a signature of the "intrinsic" disorder of amorphous systems at the origin of the controversial existence of damage spreading in glasses [7,46].

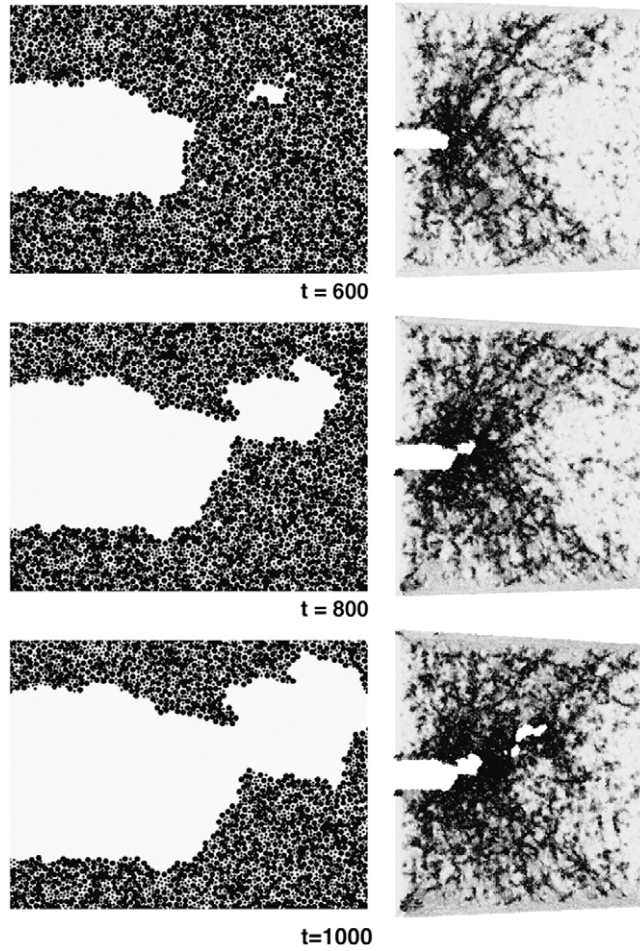


**Fig. 37.** Left: three successive snapshots of the vicinity of a crack tip growing within a Lennard-Jones glass. The dark zones correspond to the Shear Transformation Zones where plastic deformations are localized. Right: zoom at the atomic scale (Courtesy of M. Falk (from [101]).

LJ potentials have thus revealed very useful to understand the physics of fracture of amorphous systems on a very general basis. However, more elaborate potentials have been used in order to describe more realistically silicate glasses, amorphous ceramics or nanophase materials.

### 5.1.2. Fracture and damage of silicate glasses and ceramics

As far as pure a-SiO<sub>2</sub> is concerned [103], Kalia, Vashishta and coworkers use a two- and three-body potential [104]. The two-body interaction comprise Coulomb interaction due to charge transfer between Si and O, steric repulsion, and charge-dipole interactions to include electronic polarizability effects. The three-body covalent interactions involve the variations of Si-O bond lengths and Si-O-Si and O-Si-O bond angles. Starting from the melt thermalized at high temperature for a very large ( $\approx 10^5$ ) number of time steps (each time step is  $\approx 10^{-15}$  s), the system is cooled and thermalized several times before it reaches the desired temperature. The structure of the simulated glass compares remarkably well to the structure obtained from neutron diffraction [104]. However, at distances larger than a few nanometers, the structure of simulated glass is likely to be closer to the structure of a liquid than to the structure of a real glass, due to the very high cooling rate imposed numerically.

Fracture of notched samples containing up to 130 million atoms were fractured by pulling away frozen upper and lower layers [45]. The crack propagates through the nucleation, growth and coalescence of damage cavities, as shown in Fig. 11 [45,105]. The same fracture mode is actually shown to occur in other amorphous materials, such as Si<sub>3</sub>N<sub>4</sub>. Further simulations on nanophase Si<sub>3</sub>N<sub>4</sub> [106] have shown that a damage of the same nature develops within the amorphous boundaries prior to failure (see Fig. 38).

This fracture mode was first observed on amorphous silicon nitride [107]. Thin samples ( $220 \times 220 \times 20 \text{ \AA}^3$ ) were broken in mode I. Damage secondary cracks were shown to open in front of the main crack like in the cases quoted above. The crack was shown to exhibit two kinetic regimes: a slower one (average velocity  $\sim 640 \text{ m s}^{-1}$ ) corresponding to the small

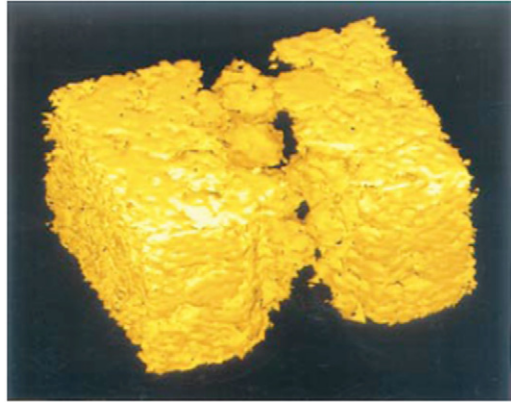


**Fig. 38.** Damage in nanophase  $\text{Si}_3\text{N}_4$  just before it fractures under an applied strain of 30% (Courtesy of R.K. Kalia (from [106])).

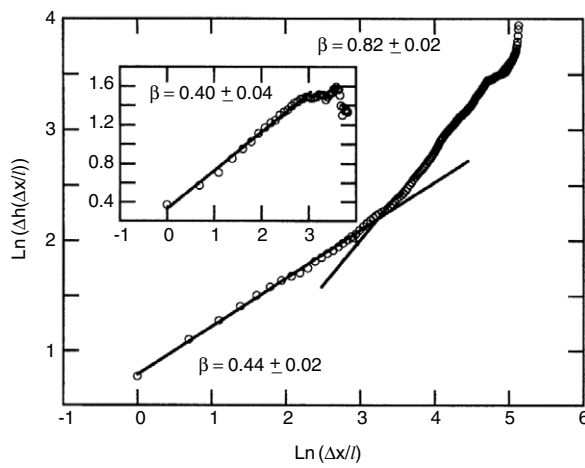


**Fig. 39.** The roughness of cracks in thin films of amorphous  $\text{Si}_3\text{N}_4$  was analyzed in the direction  $x$  of crack propagation, using the quantity  $\Delta h(\Delta x)$  defined in Eq. (19) ( $\ell = 1 \text{ \AA}$ ). Two regimes were observed, with roughness indices  $\beta \simeq 0.4$  and  $\beta \simeq 0.8$ , separated by a crossover length  $\sim 25 \text{ \AA}$ . Inset: Roughness of a damage crack, which exhibits the same small roughness exponent as the one observed at small scales (Courtesy from Nakano [107]).

scales continuous progression, and a more rapid one (average velocity  $\sim 1630 \text{ m s}^{-1}$ ) corresponding, at larger scales, to the coalescence phase. The roughness of the obtained fracture surfaces was analyzed in the direction of propagation of the crack. It was shown that it exhibits two regimes separated by a crossover length  $\sim 25 \text{ \AA}$  which corresponds rather well to the mean size of cavities at coalescence (see Fig. 39). This was compared to the results obtained by Bouchaud et al. at small scales/low velocity on metallic and soda lime glass fracture surfaces [77,67,68] (see Section 3.3.3 for discussion), and the small scale regime was actually claimed to correspond to the roughness of damage cracks, which grow slowly. This interpretation fits the one given in [78] where exponents  $\beta = \zeta \simeq 0.5$  were observed on a metallic glass fracture surface obtained by the coalescence of damage cavities. In this small scale regime, no anisotropy is expected (nor observed experimentally) since it relates to scales at which there is no favored direction. At scales larger than the cavity size, however, anisotropy is observed experimentally [52], and a value  $\beta \simeq 0.6$  is expected (see Table 2), while Nakano et al. [107] report a  $\beta \simeq 0.8$ .

Very recently, the same group studied the atomistic mechanisms of void growth and coalescence [108,109], which obviously cannot be accessed experimentally. In general, MD simulations can provide very useful qualitative guides for experiments on glasses. However, because of the limitations of the numerically accessible timescales – the maximum duration of a numerical experiment being, as already said, of the order of a few nanoseconds –, a direct comparison with observations is tricky. Glasses are quenched at rates which are orders of magnitude higher than the experimental ones. They are also deformed at rates which are much higher than experimentally accessible. Furthermore, in the field of the stress corrosion of glass [110,111], water plays a major role [112–114], and MD simulations using effective interatomic potentials cannot take into account the hydrolysis chemical reaction which results into bond breaking in the silica network and in the water molecule [115]. However, MD simulations allow one to observe in real time damage and fracture processes at the nanoscale, without all the limitations encountered in real experiments. The fracture modes observed both in dynamic fracture simulations and ultra-slow subcritical crack growth are remarkably similar, although the space and time scales of

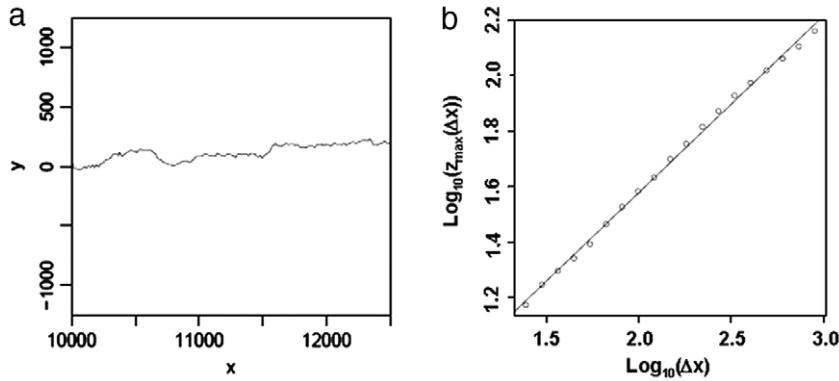


**Fig. 40.** (a) Simulated crack using conformal mapping algorithm for stress field computation. (b) Variation of  $z_{\max}(\Delta x) = \langle \max(h(t))_{t \in [x, x+\Delta x]} \rangle_x$  with  $\Delta x$  showing a power-law dependence involving an exponent  $\beta_{2D} = 0.64$ .

the experiments are much larger than their numerical counterparts. This suggests a particularly interesting spatio-temporal scaling [116,117,105].

The importance of damage and its influence on the roughness of cracks has also been emphasized in bidimensional studies due to Bouchbinder and collaborators [118,119]. They have proposed a non-perturbative solution to the problem of the stress field generated by a rough crack which is summarized in the following section.

### 5.2. Non-perturbative semi-analytic solution in two-dimensions: Iterated conformal mapping

The method developed by Bouchbinder et al. [119] is based on iterated conformal mappings which authorize the calculation of stresses and strains around a crack of arbitrary shape, for arbitrary loads at infinity. The starting point is a crack for which the conformal map from the exterior of the unit circle to the exterior of the crack is known. Then the crack is grown by little steps in desired directions, and the conformal map from the exterior of the unit circle to the exterior of the resulting crack is computed at all times.

Having the stress field around the crack, one can determine the plastic zone, the material being supposed to yield, according to the Huber-von Mises criterion, when the deviatoric stress exceeds a material-dependent threshold  $\sigma_Y$  defined as the yield stress. It is assumed that along the yield curve, which is the periphery of the plastic zone, a void can be nucleated with a given probability. This void is used as a pointer that directs further crack growth. The method of iterated conformal mappings is employed to make a growth step to coalesce the tip with the void. While the crack is supposed to propagate slowly enough to be governed by a quasi-static stress field, the coalescence step occurs on a shorter time scale. Bouchbinder et al. consider the formation and coalescence of a single void [118], while Afek et al. [120] extend the method to two voids. These models lead to rough cracks exhibiting *persistence*, i.e. long range positive correlations, as seen in experiments [84], and in MD simulations [107] at large enough scales. Furthermore, the predictions of this model compare quantitatively to experimental observations on cracks in a thin sheet: the roughness index predicted by this model is indeed  $\beta_{2D} \simeq 0.64$  (see Fig. 40), very close to the value measured by several authors on crack lines in paper [54,56,121], as shown in Section 3.1.

This method, however, is restricted to bidimensional problems. “Mean field” approaches, in which the space dimensionality does not play a role, were the first to be proposed in order to assess the influence of disorder in the failure of materials, while the interplay between stress enhancement at the crack tip, long-range elastic interactions, the irreversible character of the breaking phenomenon and material disorder makes failure modeling an extremely complicated problem. In “mean field” approaches, the method consists in evaluating the mean stress acting locally on a given element. We will restrict ourselves to the description of a very popular one, initially proposed by Pierce [122], because this model depicts fracture as a critical phenomenon, although not a dynamic phase transition, as the one we will propose in Section 6.

### 5.3. A “mean field” approach to failure: Fiber bundle models

This model consists in schematizing materials as a set of brittle fibers loaded in parallel. The failure threshold of each fiber is chosen at random, and a rule is chosen for load redistribution after each breaking. Fiber Bundle Models (FBM) have been used to address the macroscopic stress/strain constitutive laws of damageable materials, the size scaling of material strength, and the statistics of microfracturing events preceding the ultimate failure. In particular, FBM predicts power-law distributed avalanches of fibers breaking prior to the final failure.

The shape of the constitutive stress-strain law, the size scaling in strength and the exponent characterizing the scale-free distribution of avalanches of microcracks depend on the distribution of fiber thresholds. The interested reader may refer to the recent reviews of Hemmer et al. [123] and Kun et al. [124] for an extended presentation. The simplest case is the Equal Load Sharing Fiber Bundle Model (ELS-FBM) depicted in Fig. 41, in which:

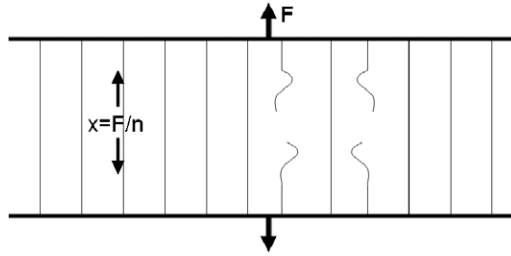


**Fig. 41.** Sketch of the Equal Load Sharing Fiber Bundle Model (ELS-FBM). A system of  $N$  parallel fibers with random breaking thresholds  $x_c$  is loaded with a gradually increasing force  $F$ . At different times, some fibers are then broken. Assuming equal sharing of  $F$  among the remaining fibers, each of them carries a load  $x = F/n$  where  $n$  denotes the number of remaining intact fibers.

- (i) Each fiber is linear elastic with a unitary Young's modulus up to a critical threshold  $x_c$  randomly distributed according to the distribution  $p(x_c)$
- (ii) At a given time  $t$ , each of the  $n$  remaining intact fiber carries the same fraction  $x = F/n$  of the global load  $F(t)$ .

This case can be seen as a mean-field approximation and allows for a complete analytic treatment [125,126,123]. Let us consider an ELS-FBM initially composed of  $N$  fibers. When loaded by a given force  $F$ , the number of intact fibers is given by:

$$n = N(1 - P_>(F/n)) \quad (30)$$

where  $P_>(x) = \int_0^x P(x)dx$  is the cumulative distribution of fiber thresholds  $x_c$ . For the sake of simplicity, we consider a uniform distribution in  $[0, 1]$  and  $P_>(x) = x$ . The results derived below remain valid for most distributions  $P(x)$ . The constitutive law relating the stress  $\sigma = F/N$  to the strain  $\epsilon = F/n$  can then be easily deduced:

$$\sigma = \epsilon(1 - \epsilon) \quad (31)$$

and the fraction  $\rho = n/N$  of intact fibers can be related to  $\sigma$  using Eq. (30):

$$\rho = \frac{1}{2} + \left(\frac{1}{4} - \sigma\right)^{1/2}. \quad (32)$$

The fraction  $\rho$  decreases as the overall stress  $\sigma$  applied to the ELS-FBM increases, up to a critical point  $\{\rho_c = 1/2, \sigma_c = 1/4\}$ . For larger values of  $\sigma$ , no real solution exists, which indicates the onset of catastrophic failure.

It is then interesting to look at the fluctuations induced by the randomness of fiber thresholds. For an ELS-FBM, the fibers break one after the other, starting from the one with the smallest failure threshold to the one with the largest one. At a force  $x$  per surviving fiber, the total force applied on the bundle is:

$$F(x) = Nx(1 - n(x)). \quad (33)$$

**Fig. 42** shows an example of variation of  $F$  as a function of  $x$  for a uniform distribution  $p$  of thresholds. This curve is non-monotonic and shows a sequence of increasing and decreasing segments. The latter are actually non-physical, since in real experiments the force  $F$  applied to a material can only be a steadily increasing function of time. The experimentally relevant function is  $F_{real}(x)$ , the so-called least monotonic increasing function no less than  $F(x)$  (see Fig. 42(a)). The horizontal plateau in  $F_{real}(x)$  correspond to avalanches of fibers breaking. One can then show [125,126,123] that the size  $\Delta$  of these avalanches is power-law distributed with an exponent  $-\eta = -5/2$ , independent of the threshold distribution  $p(x)$  (see Fig. 42(b), (c)). Note finally that if the experiment is stopped before final failure, so that the force per fiber  $x$  is smaller than  $x_c$ , the size distribution  $p(\Delta)$  is found to take the following scaling form:

$$p(\Delta) \propto \Delta^{-\eta} G(\Delta^\nu(x_c - x)) \quad (34)$$

with  $G$  a Gaussian function, and two exponents  $\eta = 5/2$  and  $\nu = 1/2$  [123]. This suggests that the breakdown process in ELS-FBM is similar to a critical phenomenon with a critical point located at the onset of total failure [123].

To go beyond mean field approaches, de Arcangelis and her collaborators [127] introduced the “Random Fuse Models” (RFM) – defined hereafter –, which have spurred since then an enormous interest.

#### 5.4. Random fuse models

Aimed at simulating quasi-static fracture processes, these models consist in exploiting the analogy between scalar mode III elasticity and electricity. The disordered material is sketched as a network of fuses with randomly distributed breakdown thresholds (see Fig. 43(a)). In RFM, the goal is not really to reproduce the failure of real materials, but to reproduce qualitatively its main features in a *model* material, keeping only the two main ingredients characterizing materials failure, i.e. the randomness of the material microstructure and the long-range coupling that accompanies load redistribution.

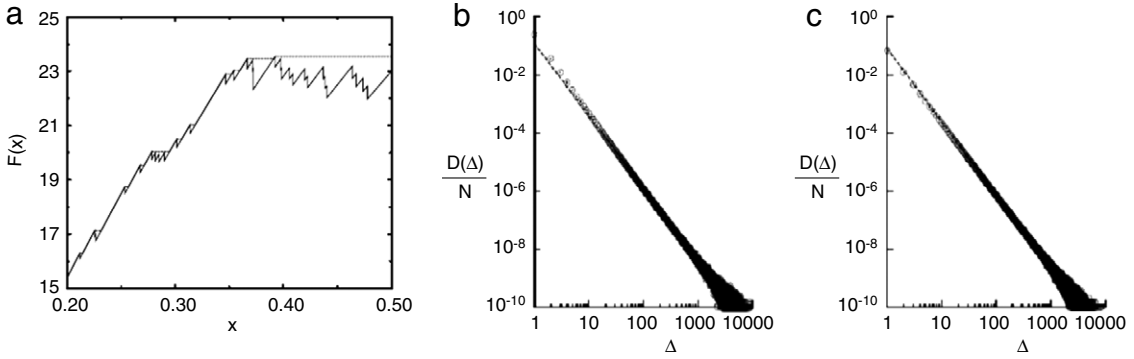


**Fig. 42.** (a) Variation of the global force  $F$  applied to an ELS-FBM. Avalanches are shown as horizontal lines. The burst distribution  $D(\Delta)/N$  is plotted on figure (b) and (c) for uniform distribution and the Weibull distribution with index 5, respectively. The dotted line represents the power-law with exponent  $-5/2$  (Courtesy of A. Hansen, from [123]).

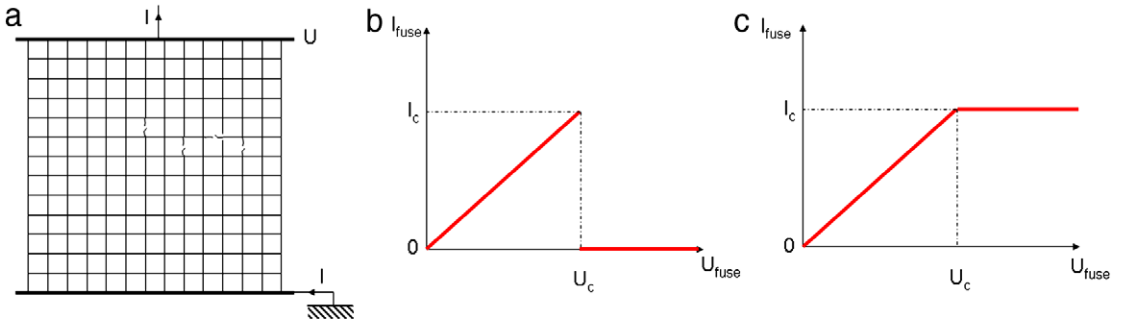


**Fig. 43.** (a) Random Fuse Networks with a square lattice geometry. Each of the bonds of the network is a fuse with unique electrical conductance and a breaking threshold randomly assigned. The behavior of the fuse is linear up to the breaking threshold  $\{I_c, U_c\}$ . Above this threshold, the current  $I_{\text{fuse}}$  (b) drops to zero in the perfectly brittle case or (c) remains constant  $I_{\text{fuse}} = I_c$  in the perfectly plastic case.

An example of Random Fuse Network is represented in Fig. 43(a). The voltages at each node and the currents crossing each element are found so that Kirchhoff and Ohm's laws are satisfied everywhere. In this class of models, current and voltage are the analogue of stress and strain, respectively. Each element of the network consists in a fuse which is removed from the system when the crossing current reaches a randomly assigned critical value. The  $I$ - $V$  characteristic of the fuses is chosen to model the local rheology of the elements constituting the micro-structure (see e.g. [128,129] for reviews). Two limiting cases can be considered:

- The *perfectly brittle* case where the behavior of the fuse is linear with unitary electrical conductance up to the random breaking threshold and drops to zero above (see Fig. 43(b)).
- The *perfectly plastic* case where the behavior of the fuse is linear with unitary electrical conductance up to the random breaking threshold and remains constant above (see Fig. 43(c)).

It has also been proposed to interpolate between these perfect responses: instead of removing a fuse once the voltage at its bounds reaches a threshold as in the perfectly brittle case, one can simply reduce its conductivity by a factor  $1 - D$  where  $D$  refers to damage [130,131]. This allows reproducing an effectively plastic  $I$ - $V$  curve.

Fig. 44 presents successive snapshots of a perfectly brittle 2D RFM “loaded” by setting the voltage of the lower horizontal line of nodes to zero, and the upper horizontal line of nodes to a constant increasing value  $U$ . In the initial stages, stress concentration is screened by disorder and fuses break randomly throughout the network. In the last stages, one micro-crack dominates and the fuse breakdowns localize around one rough line.

The  $I$ - $V$  curves in RFM play the same role as the constitutive stress-strain relationship in real materials. Fig. 45(a) displays an example of such  $I$ - $V$  curve in the 2D square RFM presented in Fig. 44. One can see the signature of damage accumulation in the non-linearity of this curve. Complete failure proceeds through successive “avalanches”, where load redistribution provokes the rapid breakdown of several neighboring fuses. The peak current  $I_c$  corresponds to the network's breakdown. Appropriate rescaling for  $I$  and  $V$  was looked for in order to find a constitutive law for RFM independent of the system size  $L$  [132,133,129]. It was found [129] that rescaling  $I \rightarrow IL/N_e$  and  $U \rightarrow U/L$  allows one to get a perfect collapse in the  $I$ - $V$  response, independently of the size of the system, up to the peak load  $I_c$  corresponding to the RFM breakdown.

The breakdown statistics and its variation with the lattice size have given rise to many works [134–136]. Recent large scale simulations revealed that the peak current  $I_c$  obeys a log-normal statistics in both two [135] and three

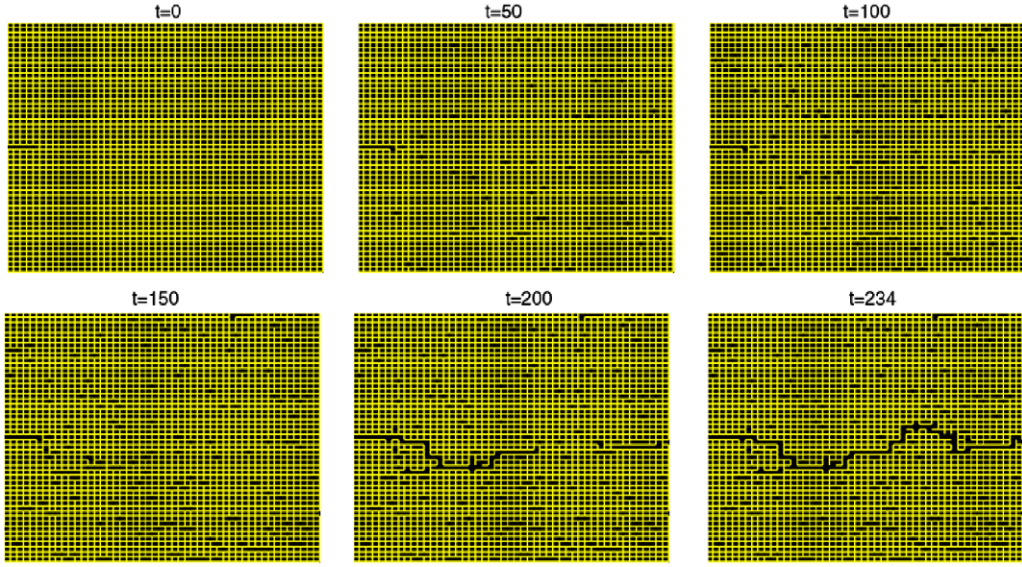


**Fig. 44.** Successive snapshots showing damage spreading in a 2D RFM square lattice before its ultimate failure. An initial 10 sites long pre-crack was introduced on the left.

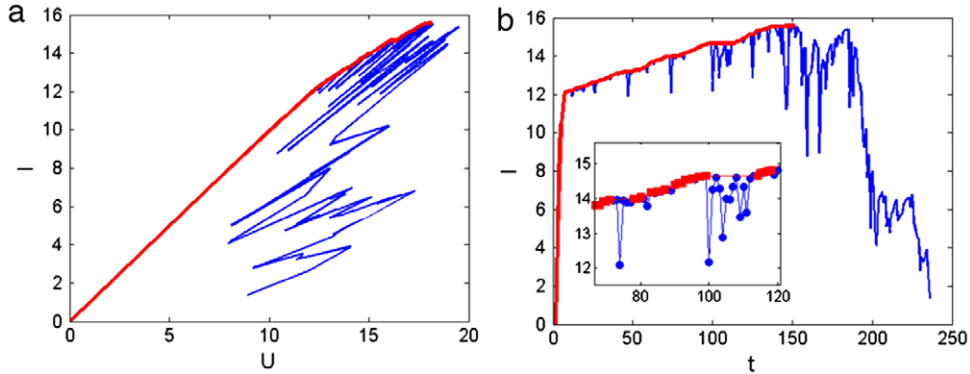


**Fig. 45.** (a) Variation of current  $I$  (a) as a function of voltage  $U$  and (b) as a function of time. The inset shows a zoom and the various points correspond to the fuse breakdown. The red squares and the blue circles represent “primary” broken bonds and “avalanches” broken bonds, respectively. The red thick line shows the envelope of steps at increasing currents. (For interpretation of the references to colour in this figure legend, the reader is referred to the web version of this article.)

dimensions [136]. The mean value of the peak current is found to scale with the lattice size  $L$  as  $\bar{I}_c \propto L^\alpha$ , with  $\alpha \simeq 0.96$  in 2D [135] and  $\alpha \simeq 1.96$  in 3D [136], independently of the lattice geometry.

#### 5.4.1. Damage precursors: avalanches

The size  $s$  of the avalanches (number of broken bonds) which can be seen in Fig. 45 have been studied extensively in two dimensional models [137–139], and shown to be power-law distributed up to a cut-off depending on the system size  $L$ :

$$P(s, L) = s^{-\tau} g(s/L^D) \quad (35)$$

where  $D$  is the fractal dimension of the avalanches, and  $g$  is a rapidly decaying function.

Surprisingly enough, the value of the exponent  $\tau$  seems to vary with the nature of the lattice in two dimensions: equal to 3.05 for a triangular lattice [138], it is equal to  $\sim 2.75$  for a diamond lattice [138], and to  $\sim 2.5$  for a square lattice [137]. The fractal dimension  $D$  is estimated to lie between 1.1 and 1.18. These values are only slightly greater than unity, indicating that cracks are nearly linear. In three dimensions, the non-universality does not seem to exist, and the avalanche size distribution is characterized by an exponent  $\tau \simeq 5/2$ , while the fractal dimension is  $D = 1.5$  [139].

As we shall see in the following, both in 2 and in 3 dimensions, these results are qualitatively very close to the prediction of Fiber Bundle Models (FBM), a mean-field theory reviewed below, in Section 5.4.2. In 3D, the value of  $\tau$  is remarkably close to the FBM prediction.

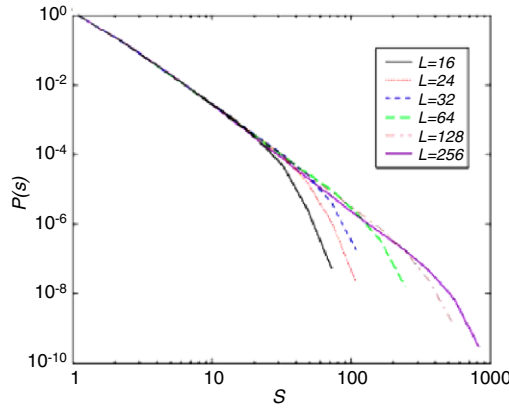


**Fig. 46.** Cumulative distribution of the the “avalanche” size before the ultimate RFM failure for various sizes. The exponent is found to be  $\tau = 3.05$  (triangular lattice) (Ref. [138]).

These avalanches in RFM are to be linked with the acoustic emission (AE) generated by the microfracturing events preceding or accompanying material failure, and, at much larger scale, with the seismic activity associated with earthquakes. In both cases, the cumulative distribution in energy are found to obey a power-law characterized by an exponent  $b$  typically lying between  $b = 1.3$  and  $b = 1.6$  [140,141]. It is then tempting to relate the exponent  $\tau$  to  $b$ . This has been done by Minozzi et al. [142] who have characterized the statistics of AE produced by micro-cracks in a *dynamic* lattice model. It was found that:

$$b = 1 + \frac{\tau - 1}{2} \quad (36)$$

$\tau = 5/2$  corresponds to  $b = 1.75$ . However, this figure is quite different from the one found experimentally, for which a value  $b \simeq 1.4\text{--}1.5$  is reported [140,143]. It was suggested [144] that residual stresses which are not taken into account by models play an important role.

Besides the kinetics of fracture, the morphology of cracks produced by RFM has also been extensively studied [145–149, 138,150,151]. In the following section, we review the main results (Fig. 46).

#### 5.4.2. Crack surfaces in perfectly plastic RFM: A minimum energy surface

In the case of RFM with perfectly plastic fuses, it was conjectured [145,152] that the crack line (2D case) or the crack surface (3D case) can be mapped to a directed polymer (2D case) [153] or a minimum energy surface (3D case). The 2D crack line is then expected to display a self-affine exponent equal to  $\beta_{2D} = 2/3$  [154], while the 3D fracture surface is isotropic and characterized by a roughness exponent  $\zeta_{3D} = \beta_{3D} \simeq 0.42$  [155] in three dimensions. The latter value is quite close to the one reported from observations performed either on metallic glasses [78] or on metallic materials and soda glass [67,68,156] at very small length scales. Fracture being an irreversible phenomenon, it is actually interesting to note that an equilibrium ansatz cannot apply at all scales. However, it can concern small enough length scales and result from a quasi-static, very slow process [147].

#### 5.4.3. Crack surfaces in brittle RFM: A gradient percolation process

It was suggested [157] that, for brittle fracture surfaces, the observed large-scale self-affine scaling properties are due to a damage coalescence process leading to failure. This process is described by a stress-weighted percolation phenomenon in a self-generated quadratic damage gradient. Then, the resulting roughness exponent can be related to the exponent  $\nu$  describing the divergence of the correlation length  $\xi \propto (p - p_c)^{-\nu}$  where the density of broken bonds  $p$  is reaching the critical value  $p_c$  in standard percolation problems. The argument is the following: if the disorder in the breaking thresholds is very broad, the RFM will behave as a regular percolation process, and the final crack will be fractal, with a width proportional to the system size and a resulting roughness exponent equal to one. However, for a narrow threshold distribution, damage will localize over a width  $l_y$  (see Fig. 47). Scaling arguments [157] allow one to relate the crack width to this damage width as  $w \propto l_y^{2\nu/(1+2\nu)}$ , and then to the system size  $L$  as  $w \propto L^{2\nu/(1+2\nu)}$ . This suggests that the observed large-scale self-affine roughness exponent  $\zeta$  is given by  $\zeta = 2\nu/(1+2\nu)$ .

In standard scalar percolation,  $\nu = 4/3$  and  $\nu \simeq 0.88$  in 2 and 3D respectively. This leads to  $\beta_{2D} = 8/11 \simeq 0.73$  and  $\zeta_{3D} = \beta_{3D} \simeq 0.64$  respectively. It is worth emphasizing that the argument developed in [157] is general and can be extended to real elastic 3D brittle fracture. In elastic percolation problems,  $\nu$  is expected to be equal to:  $\nu = 2$  [159–161], which leads to  $\zeta_{3D} = \beta_{3D} = 4/5$  in excellent agreement with the ubiquitous value  $\zeta_{3D} \approx 0.8$  reported experimentally and discussed extensively in Sections 3 and 4.

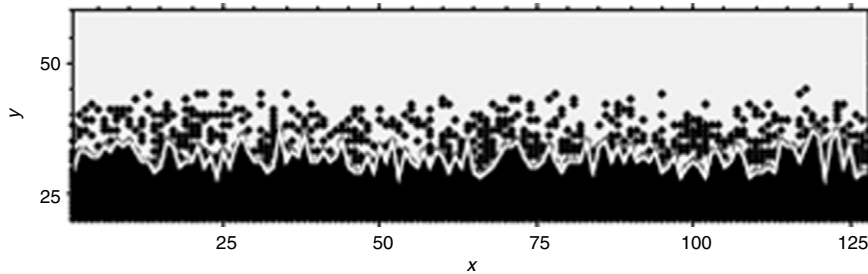


**Fig. 47.** Crack front generated by a stress-weighted percolation model for a  $128 \times 128$  system. The fracture is propagating from bottom to top. The broken springs are black dots. The crack front is drawn as a white line (Courtesy of Schmittbuhl and Hansen [158]).

#### 5.4.4. Crack surfaces in brittle RFM: Numerical results

The morphology of cracks has also been investigated numerically [138,145–151]. As in experiments, – and as expected from the previous theoretical arguments –, cracks are found to exhibit self-affinity. In two dimensions, the (local) roughness exponent  $\beta_{2D}$  is found to be universal,  $\beta_{2D} = 0.65 – 0.70$  [145,138], independent of the lattice topology, the presence or not of a preexisting initial notch and of the disorder in breaking thresholds [138,151] (Fig. 48). Actually, and this is in contrast with experimental observations, the roughness of 2D cracks generated with fuse models do not depend either on the presence of damage [162].

In three dimensions, the roughness exponents are found to be equal to:  $\zeta_{3D} = \beta_{3D} \simeq 0.42$  [147,148,150]. Contrary to what is observed experimentally, there is no anisotropy in the exponents [150]. Note that the only roughness index is very close to the minimum surface exponent expected in perfectly plastic RFM, which suggests that the analogy conjectured in the case of RFM with perfectly plastic fuses [145,152] can probably be extended to the case of brittle RFM. This remains however controversial [146,147], and the small size of the simulated 3D samples introduces a large degree of uncertainty.

As far as a comparison between experiments and simulations is concerned, one might also object that it is risky, because experiments are performed in mode I, while RFM correspond to scalar, mode III fracture. However, recent simulations on a beam model supposed to be equivalent to tensorial mode I elasticity [163] show that in this case also, 2D cracks have a roughness index close to:  $\beta_{2D} \simeq 0.64$ . These cracks do not exhibit anomalous scaling, and when overhangs are removed, they are nowhere multi-affine, and the probability distribution of their height differences is a Gaussian for all window sizes.

It is then interesting to compare the roughness exponents measured in RFM simulations to the ones observed experimentally. In 2D, the RFM roughness exponent  $\beta_{2D} = 0.71$  is very close to the one observed experimentally in quasi-two-dimensional materials, as reported and discussed in Section 3.1. On the contrary, in three dimensions, the RFM roughness indices  $\beta_{3D} = \zeta_{3D} \simeq 0.42$  are significantly smaller than the values  $\zeta_{3D} \simeq 0.8$  and  $\beta_{3D} \simeq 0.6$  observed experimentally in a wide range of materials, as discussed extensively in Section 4. On the other hand, it is pretty close to the  $\zeta_{3D} \simeq 0.4$  observed in ductile fracture in metallic alloys [68] broken in fatigue at ultra-slow velocity or metallic glasses [78]. RFM may be a relevant model for this class of failure.

Let us finally mention that large scale numerical simulations revealed the existence of anomalous scaling in both 2D and 3D RFM. In other words, the global roughness exponent  $\zeta^{\text{glob}} = 0.87$  that characterizes the scaling between the crack roughness and the system size differs from the local one discussed in the two preceding paragraphs. In 2D, this global roughness exponent is found to be  $\beta_{2D}^{\text{glob}} = 0.87$  [138,151] while in 3D,  $\zeta_{3D}^{\text{glob}} = 0.5$ . In both cases, the exponents were found to be independent of the disorder. The origin of this anomalous scaling remains unclear. It seems to be intrinsic to the scalar character of RFM since it disappears in Random Beam Models [163]. Experimentally, as discussed in Section 3, anomalous scaling was observed only within transient regimes where roughness has to develop from a straight notch [81,82,85].

As it could be seen throughout this section, these statistical models succeed in reproducing qualitatively most of the features observed in the failure of heterogeneous media reported in Sections 3 and 4. However, the agreement remains only qualitative. Moreover, these models rely on important simplifications which makes quantitative comparisons with experiments rather difficult.

## 6. Models of an elastic front propagating through randomly distributed obstacles

Another approach – pioneered by Gao and Rice [164] – consists in extending the “standard” LEFM of homogeneous materials to the case of heterogeneous media by considering that the crack front propagates through a random field of local fracture toughnesses  $K_{lc}$ . Gao and Rice [164] have computed corrections to the mode I stress intensity factor along a 2D front due to its in-plane fluctuations resulting from local variations in toughness. But the first attempt to derive from such a model predictions concerning the morphology of a 3D fracture front, and hence the morphology of the fracture surface itself, as the trace left behind by the propagating front is due to Bouchaud and coworkers [86]. This model will be discussed below.

In all the further generalizations of Gao and Rice’s bidimensional model [164], the distribution of local fracture toughnesses is assumed to be sufficiently narrow so that the first-order perturbative analysis presented in Section 2.1.3 can be used to link the local values of the stress intensity factors along the crack front to the crack front shape. Then, the local

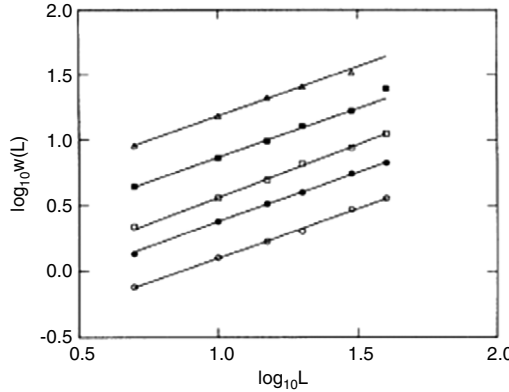


**Fig. 48.** Width of the final crack ignoring its branchings  $w$  as a function lattice size  $L$  for various distribution of threshold currents.

perturbation  $\delta K_I(z)$  of the mode I stress intensity factor depends only on the in-plane coordinate  $f(z, t)$  of the front, while the mode II and III perturbations,  $\delta K_{II}(z)$  and  $\delta K_{III}(z)$  respectively, depend only on the out-of-plane coordinate  $h(z, x = f(z, t))$  (cf. Section 2.1.3 and Fig. 3). This property, which only exists for the first-order perturbative solution, will be shown to be extremely convenient.

### 6.1. Equation of motion: Interfacial crack front

As a matter of fact, this means that one can analyze the mode I perturbation of a 3D crack front as if it were reduced to its 2D projection onto the fracture plane. In other words, the motion of a real 3D crack front can be reduced to the one of a planar crack front propagating within a 2D material depicted in Fig. 49(a). This problem was addressed by Schmittbuhl et al. [20] and Ramanathan et al. [21].

Under quasi-static conditions, the local velocity of a point  $M(z, x = f(z, t))$  of the front is proportional to the excess energy locally released  $G(M) - \Gamma(M)$  (Eq. (2)). Material heterogeneities are then modeled by introducing a random component to the fracture energy:  $\Gamma(M) = \Gamma^0(1 + \eta(z, x))$  where  $\eta$  is a meanless delta-correlated random term. This induces distortions of the front, which in turn generate a perturbation in  $G(M)$  [19,164]:  $G(M) = G^0 \left(1 + \frac{1}{2\pi} \int \frac{f(z') - f(z)}{(z' - z)^2} dz'\right)$  where  $G_0$  denotes the reference mechanical energy release rate which would result from the same loading with a straight front located at the same mean position. The equation of motion then writes [164,20,21]:

$$\frac{1}{\mu} \frac{\partial f}{\partial x} = (G_0 - \Gamma_0) + \frac{G_0}{2\pi} \int \frac{f(z') - f(z)}{(z' - z)^2} dz' + \eta(z, f(z, t)). \quad (37)$$

This equation has been extensively studied. It was shown to describe systems as diverse as interfaces in disordered magnets [165,166] or contact lines of liquid menisci on rough substrates [167–169].

It was shown to exhibit a so-called depinning transition, which belongs to the category of *dynamic phase transitions* for which the order parameter is the average velocity  $\bar{v} = \langle \frac{\partial f}{\partial x} \rangle$ , equal to zero in the stable phase where the elastic line is at rest, and equal to a finite value in the propagating phase where the front moves (see Fig. 49(b)). What controls this transition is the “force”  $F = G_0 - \Gamma_0$  (Fig. 49(b)). When  $F$  is smaller than a certain threshold  $F_c$ , the front is trapped by the material heterogeneities and its velocity is zero everywhere. For  $F$  larger than  $F_c$ , the line is depinned from the last metastable state, and moves with a non-zero average velocity.

#### 6.1.1. Velocity evolution as a function of the loading

A key feature of this kind of equation is that the depinning transition at  $F_c$  belongs to the realm of collective critical phenomena characterized by universal scaling laws [170] independent of the microscopic and macroscopic details, i.e. of the material microstructure and the loading conditions. In particular, when  $F$  approaches  $F_c$  from above, the average velocity is expected to vanish as:

$$\bar{v} \propto (F - F_c)^\theta \quad (38)$$

where  $\theta$  is called the velocity exponent. This exponent was estimated using Functional Renormalization Group (FRG) methods and found to lie between  $\theta = 0.78$  (to first order) [167] and  $\theta = 0.59$  [171] (to second order). Numerical estimations lead to  $\theta = 0.63$  [172]. This behavior was recently observed experimentally in Botucatu sandstone [173,174] where, above a given threshold in mechanical energy release rate  $G_c$ , the average crack growth velocity was found to evolve as  $(G - G_c)^\theta$  with  $\theta \simeq 0.80 \pm 0.15$  (see Fig. 50(b)).

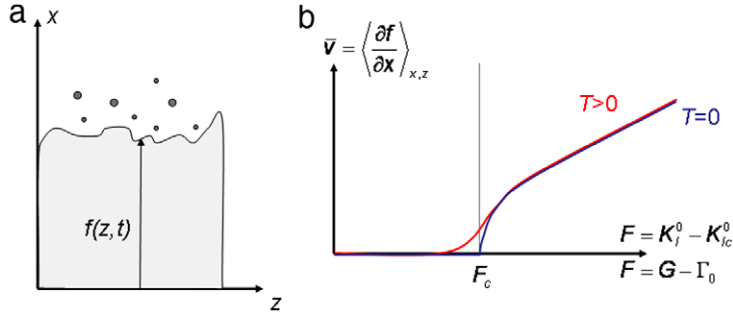


**Fig. 49.** (a) Sketch and notations for a planar crack propagation through a random field of fracture toughnesses. (b) Pinning/depinning transition at zero temperature (blue) or finite temperature (red). The control parameter in this system is the force  $F = K_l^0 - K_{lc}^0$  (resp.  $F = G^0 - \Gamma^0$ ) defined as the difference between the constant stress intensity factor  $K_l^0$  (resp. the constant mechanical energy release rate  $G^0$ ) that would result from the same loading with a straight crack front located at the same mean position and the mean value of the local toughness  $K_{lc}^0$  (resp. the mean value of the fracture energy  $\Gamma_0$ ). The order parameter is the mean value of the velocity  $\bar{v} = \langle \partial f / \partial x \rangle_{z,t}$  averaged over all  $z$  and  $t$ . (For interpretation of the references to colour in this figure legend, the reader is referred to the web version of this article.)

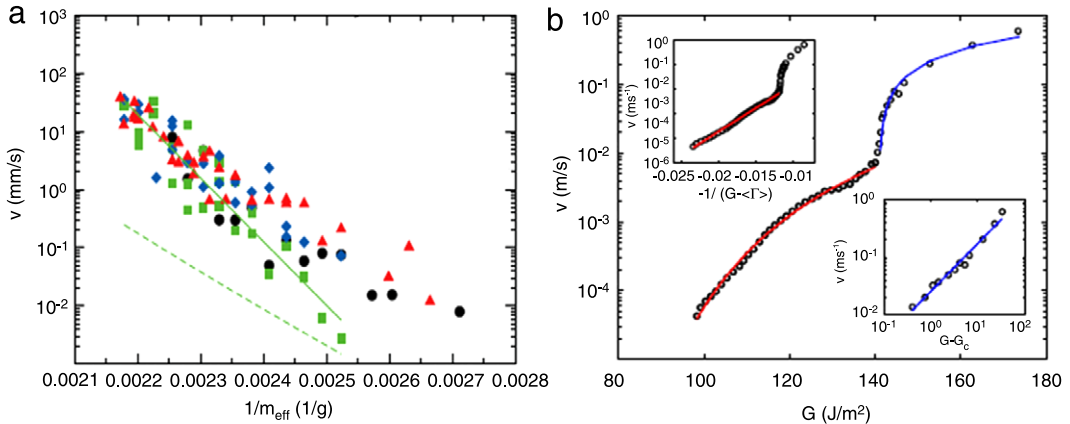


**Fig. 50.** (a) Crack velocity  $v$  as a function of the inverse of the applied mass  $m_{eff}$  in paper peeling experiments. The line indicates an exponential decay  $v \propto \exp(C/m_{eff})$  and the four sets (circle, rectangle, diamond, triangle) correspond to different experiments (Courtesy of Kovisto et al., from [177]). (b) Crack velocity  $v$  as a function of the mechanical energy release  $G$  in Botucatu sandstone. When  $G < G_c$   $v \propto \exp(C/(G - \Gamma^0))$  (top-left inset) while for  $G > G_c$ ,  $v \propto (G - G_c)^\theta$  with  $\theta \approx 0.81$  (Courtesy of Ponson, from [174]).

Strictly speaking, the pinning/depinning scenario presented above with a front perfectly trapped for  $F$  smaller than  $F_c$  only holds at zero temperature. At finite temperature  $T > 0$ , thermally activated processes can enable a subcritical crack propagation. In this so-called creep regime, the front velocity is expected to scale as [175,176]:

$$\bar{v} \propto \exp\left(-C\left(\frac{F_c}{F}\right)^\mu\right) \quad (39)$$

with  $\mu = 1$ . This subcritical creep law describes rather well experiments of paper peeling [177] and subcritical crack growth in sandstone [173,174] (see Fig. 50).

### 6.1.2. Effective toughness distribution

The arguments that have led to Eq. (37) can be rewritten by considering the local balance between the mode I stress intensity factor and the local toughness  $K_{lc}$ . One then gets:

$$\frac{1}{\mu} \frac{\partial f}{\partial x} = (K_l^0 - K_{lc}^0) + \frac{K_{l0}}{2\pi} \int \frac{h(z) - h(z')}{(z - z')^2} dz' + \eta(z, f(z, t)) \quad (40)$$

where  $K_l^0$  denotes the constant stress intensity factor that would result from the same loading with a straight crack front at the same mean position, and  $K_{lc}^0$  the mean value of the local toughness. This equation also exhibits a depinning transition when the “force”  $F = K_l^0 - K_{lc}^0$  reaches the threshold value  $F_c$ . Universality close to the transition at  $F = F_c$  was used [178,179] to determine the statistics  $p(K_c, L)$  of the effective macroscopic toughness  $K_c = F_c + K_{lc}^0$  seen by a crack front of length  $L$  at the onset of propagation. The main results are:

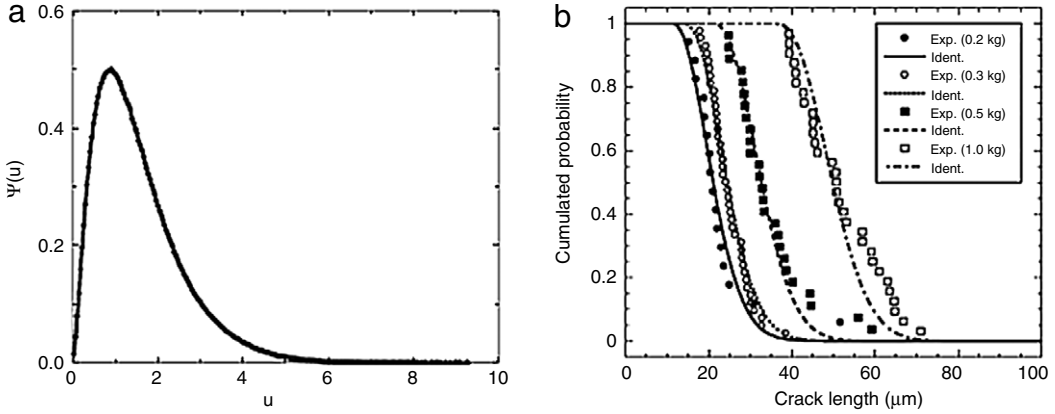


**Fig. 51.** (a) Universal distribution  $\Psi(u)$  of the reduced toughness  $u = L^{1/v} (K_c^* - K_c)$  expected in depinning scenario such as the one described by Eq. (40). The quantities  $L$  and  $K_c$  refer to the length of the crack front and the effective toughness of the material. The value  $K_c^*$  is the deterministic value of this effective toughness in case of an infinite crack front (b) Cumulative probability as a function of the crack radius in indentation experiments performed in Alumina at various force  $F$ . The symbols corresponds to experimental points while the lines corresponds to theoretical predictions (Courtesy of Charles et al., from [179]).

- As  $L$  tends to infinity,  $p(K_c, L)$  tends to a Dirac distribution and the heterogeneous material converges toward a homogeneous one characterized by a deterministic fracture toughness  $K_c^*$ .
- For a crack front of finite length  $L$ ,  $K_c$  is always smaller than  $K_c^*$ . In other words, the apparent toughness depends explicitly on the crack length, which is analogue to an  $R$ -curve effect (Section 2.2.3).
- For a crack front of finite length  $L$ , the standard deviation  $\sigma(L) = (\langle K_c^2 \rangle - \langle K_c \rangle^2)^{1/2}$  vanishes with  $L$  as  $\sigma(L) \propto L^{-1/v}$  where the exponent  $v \simeq 1.64$  is universal.
- For large enough  $L$ , the reduced toughness  $u = L^{1/v} (K_c^* - K_c)$  is observed to follow a universal distribution  $\Psi(u)$  represented in Fig. 51(a).

These results were used [180] to predict the statistics of crack arrest lengths in various brittle materials for various indentation forces, and shown to describe the data fairly well (Fig. 51(b)).

#### 6.1.3. Displacement-imposed quasi-static failure: Intermittency and crackling noise

In the equation of motion presented in Eq. (45), the effective force  $F$  acting on the front was constant since  $G^0$  – or  $K_0$  – was assumed to be constant. One can imagine a different situation where the loading conditions are such that  $G^0$  increases slowly with time and decreases with the mean crack length  $\langle f(z, t) \rangle_z$ . This situation is the one encountered in the experiment described in Section 3.2 where a crack front is constrained to propagate along the weak heterogeneous interface between two Plexiglas block by lowering the bottom part at constant velocity [22,23,66].

Then, the effective force  $F(t, \{f\})$  is not constant anymore: when  $F(t, \{f\}) < F_c$ , the front remains pinned and  $F(t, \{f\})$  increases with time. As soon as  $F(t, \{f\}) > F_c$ , the front propagates,  $F(t, \{f\})$  increases, and, as a consequence,  $F(t, \{f\})$  is reduced until the front is pinned again. This retroaction process keeps  $F(t, \{f\})$  always close to the depinning transition  $F_c$  and the system remains at criticality during crack propagation, as for self-organized-critical systems [181]. As a result, the crack is found [182] to exhibit an intermittent crackling dynamics and to progress through scale-free (both in space and time) avalanches characterized by universal distributions (see Fig. 52). This approach succeeds in reproducing quantitatively the dynamics observed recently during the slow propagation of a crack along a weak heterogeneous plane of a transparent Plexiglas block [59].

#### 6.1.4. In-plane roughness predictions

Let us finally note that Eq. (40) – or (37) – predicts that the morphology of the crack front exhibits self-affine scaling features. Different scaling regimes, characterized by different roughness exponents  $\zeta_{2D}$  are observed, depending on the value of the force  $F$  [183]:

- for  $F = 0$ , the front is self-affine with a roughness exponent  $\zeta_{2D} = \zeta_{eq} = 1/3$  over the whole range of length scales.
- for  $F = F_c$ , the front is self-affine with a roughness exponent  $\zeta_{2D} = \zeta_{dep}$  over the whole range of length scales. The depinning exponent  $\zeta_{dep}$  was estimated using FRG methods and found to be between  $\zeta_{dep} = 0.33$  [167] (first order) and  $\zeta_{dep} = 0.47$  [171] (second order). It was also precisely evaluated to  $\zeta \simeq 0.388 \pm 0.002$  using numerical simulations [184].
- as  $F$  goes far beyond  $F_c$ , the front is not self-affine anymore and exhibits logarithmic correlations [167].
- for  $0 < F < F_c$ , one expects to observe two regimes [183]: a small length scales regime where the roughness exponent has the equilibrium value  $\zeta_{eq}$ , and a large length scales regime where the roughness exponent is  $\zeta_{dep}$ . The crossover length  $L_{opt}$  separating these two regimes scales as  $F^{-1/(1-\zeta_{eq})}$ .

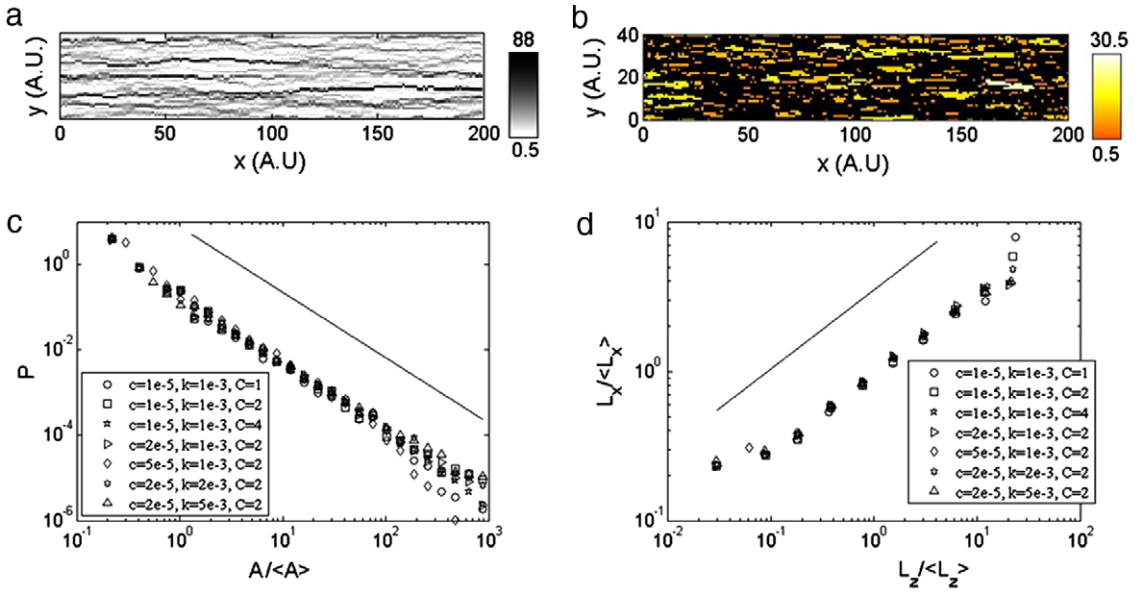


**Fig. 52.** (a) Typical gray scale map of the waiting time matrix  $w(x, y)$  obtained from the solution of Eq. (45). (b) Spatial distribution of avalanches corresponding to zones with velocities larger than a given threshold. The avalanches duration is given by the clusters color according to the colorscale given in inset. The distribution of the cluster area  $A$ , the scaling between the width  $L_x$  and the length  $L_z$  of the avalanches are plotted in (c) and (d) respectively (From [182]).

**Table 3**

Summary of the various self-affine regimes predicted for in-plane crack fronts by Eq. (37) or Eq. (40).

Force	$\zeta'$	Crossover length
$F = 0$	$\zeta_{eq} = 1/3$	
$0 < F < F_c$	$\zeta_{eq}$ for $z < L_{opt}$ $\zeta_{dep}$ for $z > L_{opt}$	$L_{opt} \propto F^{-1/(1-\zeta_{eq})}$
$F = F_c$	$\zeta_{dep} \simeq 0.4$	
$F_c < F$	$\zeta_{dep}$ for $z < \xi$ $\log$ for $z > \xi$	$\xi \propto (F - F_c)^{-\nu}$

- for  $F > F_c$ , one expects to observe two regimes [185]: a small length scales regime where the roughness exponent is  $\zeta_{dep}$ , and a large length scales regime with logarithmic correlations. The crossover length  $\xi$  separating these two regimes scales as  $(F - F_c)^{-\nu}$ .

Table 3 summarizes these results.

The experimental measurements of in-plane roughness reported in Sections 3.2 and 3.3 were performed for  $F$  very close to  $F_c$ . One would therefore expect to observe a self-affine front characterized by a roughness exponent  $\zeta' = \zeta_{dep} \simeq 0.388$ . This value is significantly smaller than the  $\zeta' \simeq 0.5\text{--}0.6$  reported experimentally both for interfacial fracture [22,23] and for the 2D projection of a 3D crack front [63]. However, recent experiments performed by Santucci and coworkers report a roughness exponent  $\zeta' \simeq 0.35$  at large scale, in agreement with the predictions of Eq. (49). The apparent discrepancy between experiments [63,22,23] and theory is then attributed to the fact that measurements were performed at small scales, below the characteristic scale  $\Lambda$  of the disorder term  $\eta$  in Eq. (45), while predictions of Eq. (45) are relevant for scales larger than  $\Lambda$  (see Section 3.1).

Let us now turn to the out-of-plane meandering of a three-dimensional crack front.

## 6.2. Morphology of fracture surfaces: Three-dimensional crack front

The first model is due to Bouchaud and coworkers [86], who proposed to cast the fracture surface as the trace left by an elastic line moving within a 3D disordered landscape. This phenomenological approach is described hereafter.

### 6.2.1. A phenomenological model derived from symmetry principles

Following the work of Ertas and Kardar on the motion of a vortex line in superconductors [186], Bouchaud et al. suggested that the simplest nontrivial equation that can be derived for the motion of a crack front reads:

$$\frac{\partial f}{\partial t} = V + \gamma \frac{\partial^2 f}{\partial z^2} + \frac{\lambda_{xx}}{2} \left( \frac{\partial f}{\partial z} \right)^2 + \frac{\lambda_{xy}}{2} \left( \frac{\partial h}{\partial z} \right)^2 + \eta_x(z, t),$$

$$\frac{\partial h}{\partial t} = \gamma \frac{\partial^2 h}{\partial z^2} + \lambda_y \left( \frac{\partial f}{\partial z} \right) \left( \frac{\partial h}{\partial z} \right) + \eta_y(z, t) \quad (41)$$

where  $f(z, t)$  is the in-plane component of the crack front at location  $z$  and time  $t$ , and  $h(z, t) \equiv h(z, f(z, t))$  is the out-of-plane component of the crack front (see Fig. 3).  $V$  is the nominal crack velocity,  $\gamma$  a line tension and  $\eta_x(z, t), \eta_y(z, t)$  thermal noise terms encoding the local disorder of the material. The non-linear terms  $\lambda$  account for the fact that the local velocity depends on the local direction of the crack and are chosen to respect the symmetry of the system.

This set of two coupled Langevin equations leads to a Family-Viseck anisotropic self-affine scaling for both  $f(z, t)$  and  $h(z, t)$  [186]. From the relation between  $h(z, x)$  and  $f(z, t)$  and  $h(z, t)$ , one can then show that  $h(z, x)$  obeys also a Family-Viseck anisotropic self-affine scaling:

$$\Delta h(\Delta z, \Delta x) = \Delta x^{\zeta/\kappa} f(\Delta z / \Delta x^{1/\kappa}) \quad (42)$$

where  $f(u) \sim \begin{cases} 1 & \text{if } u \ll c \\ u^\zeta & \text{if } u \gg c \end{cases}$

where the exponents  $\zeta$  and  $\kappa$  are the roughness and the dynamic exponents respectively. Their values were estimated numerically [186]. They depend on the parameters  $\{\lambda\}$ . In particular, for  $\lambda_{xy} \ll \lambda_{xx}, \lambda_y, \zeta \simeq 0.75$  and  $\kappa \simeq 1.5$ , in very good agreement with the experimental values reported in Section 4.1.2.

Let us note finally that Eq. (41) describes the motion of an elastic line within a disordered material at *finite velocity*. As  $V$  vanishes, one would expect [68,84] the thermal random terms  $\eta_{x,y}(z, t)$  to become quenched noise:  $\eta_{x,y}(z, x) = f(z, t), y = f_\perp(z, t)$  and then to observe another set of exponents  $\zeta_{dep} = 0.5$  and  $\kappa_{dep} \simeq 2.3$ . To be more precise, two scaling regimes are expected for fracture surfaces in this scenario: a large length-scale regime where  $\zeta = 0.75$  and  $\kappa = 1.5$ , and a small length-scale regime where  $\zeta = 0.5$  and  $\kappa = 1.3$ . The crossover  $\xi$  between the two scales as  $V^{-1}$ . This kind of behavior is compatible with experimental observations on metallic alloys broken under fatigue [68,84]. It may also have been observed in a soda-lime silicate glass broken under stress corrosion [68,156] – where it is generally admitted that a clear threshold exists – but it was not seen in pure amorphous silica [52,187] – where there is no stress corrosion threshold –. However, the validity of roughness measurements at small scales using Atomic Force Microscopy was recently questioned, because of artifacts due to the finite size of the tip [50]. An alternative interpretation was proposed recently in [78], which has been discussed in Sections 3.3 and 5.1.2.

### 6.2.2. Path equations within a linear elastic description: 2D case

The main weak point identified in this phenomenological approach is that Eq. (41) is local, i.e. the rate of propagation at a given point  $z$  depends only on the front geometry – position, slope, curvature... – at the same point. This is not justified in elastic fracture mechanics, although it will be argued later that screening of long range elastic interactions by damage – and, in particular, by plasticity – may significantly alter the non-local elasticity of the crack front and lead back to an ordinary type of elasticity, as the one used in Bouchaud et al.'s model [86].

A more rigorous approach is to derive a linear elastic stochastic description of crack paths in the spirit developed in Section 6.1. Let us first consider the simpler case of a 2D tensile crack such as the one depicted in Fig. 3(a). In virtue of the principle of local symmetry (see Section 2.1.4), the path chosen by a crack propagating in an elastic isotropic material is the one for which the net mode II stress intensity factor should vanish at each time  $t$  of the propagation. Two contributions should be taken into account in the evaluation of  $K_{II}$ . The first contribution reflects the heterogeneous nature of the material. This contribution is modeled by a quenched uncorrelated random field:

$$K_{II}^{(1)} = K_I^0 \eta(x) \quad (43)$$

where  $K_I^0$  denotes the reference mode I stress intensity factor which would result from the same loading with a straight front at the same mean position. The second contribution  $K_{II}^{(2)}$  is induced by the crack roughness  $h(x)$ . To first order,  $K_{II}^{(2)}$  is given by Eq. (14). Finally, making  $K_{II}^{(1)} + K_{II}^{(2)} = 0$  leads to the following path equation:

$$\frac{1}{2} \frac{dh}{dx} = -\sqrt{\frac{\pi}{2}} \frac{A_I^0}{K_I^0} h(x) + \frac{T}{K_I^0} \int_{-\infty}^x \frac{1}{\sqrt{x-u}} \frac{dh}{dx} \Big|_u du + \eta(x). \quad (44)$$

This equation leads to logarithmically rough cracks in 2D brittle materials, in apparent disagreement with the experimental observations reported in Section 3.1. A slightly modified version of this description was proposed by Katzav and coworkers [188]. They consider that the crack propagates smoothly by satisfying the principle of local symmetry until it meets a heterogeneity which induces a random change in the fracture toughness and a random shear perturbation. Calling  $\ell$  the mean distance between heterogeneities,  $K_I^0 \eta_I(x)$  and  $K_{II}^0 \eta_{II}(x)$  the fields of random perturbations in toughness and shear at heterogeneities, the equation of path then reads:

$$\ell \frac{d^2}{dx^2} h = \frac{d\eta_{II}}{dx} + \frac{d\eta_I}{dx} \left( \frac{1}{2} \frac{dh}{dx} + \sqrt{\frac{\pi}{2}} \frac{A_I^0}{K_I^0} h(x) - \frac{T}{K_I^0} \int_{-\infty}^x \frac{1}{\sqrt{x-u}} \frac{dh}{dx} \Big|_u du \right). \quad (45)$$

Katzav et al. [188] have solved numerically – and analytically in the case  $T = 0$  – this equation. They showed that the resulting crack profile  $h(x)$  exhibits roughness with a small-scale apparent self-affine regime with exponent  $\beta_{2D} = 0.5$  and departs from self-affinity at large length-scales. Note that both Eqs. (44) and (45) lead to crack paths with negative correlations, while in experiments, a roughness exponent  $\beta_{2D} > 0.5$  is reported (see Table 2), indicating persistence. This problem was first addressed by Bouchbinder et al. [119,118], who have shown that the presence of a FPZ of finite size is essential to produce positive correlations (see Section 5.2). It is worth emphasizing that in this case, the presence of positive correlations does not depend on the FPZ size and that the scaling domain extends much beyond it.

### 6.2.3. Path equations within a linear elastic description: 3D case

The previous approach can be easily extended to the 3D linear elastic case by assuming that, as for a 2D tensile crack, the chosen path is the one for which  $K_{II} = 0$  at all times and locations. Several contributions should be included into  $K_{II}$ ; the first one is due to the heterogeneous nature of the material and is modeled by a quenched delta-correlated random field  $\eta$ :

$$K_{II}^{(1)}(z, t) = K_I^0 \eta(z, x = f(z, t), y = h(z, x = f(z, t))) \quad (46)$$

where  $K_I^0$  is the reference mode I stress intensity factor which would result from the same loading with a straight front at the same mean position. The second contribution  $K_{II}^{(2)}$  arises from the coupling of the singular mode I component of the stress field of the unperturbed crack with the crack roughness  $h(z, x)$  behind the crack front. To first order in  $h$ , this contribution is given by Eq. (15). Considering small roughness with respect to the specimen size  $L$ , i.e.  $\partial h / \partial x \ll 1$  and  $\partial h / \partial z \ll 1$ , this second contribution is found [26] to reduce to:

$$K_{II}^{(2)}(z, t) = -\frac{1}{2} K_I^0 \frac{\partial h}{\partial x} \Big|_{(x=f(z,t),z)} + \frac{1}{\pi} \frac{2-3\nu}{2(2-\nu)} K_I^0 \int_{-\infty}^{\infty} \frac{1}{z-z'} \frac{\partial h}{\partial z} \Big|_{(x=f(z',t),z')} dz' \quad (47)$$

where the reference  $x = 0$  has been placed at the crack tip. Finally, a third contribution  $K_{II}^3 = K_{II}^0 = \text{constant}$  is added to take into account the unavoidable misalignment in the loading system. Finally, making the net mode II stress intensity factor  $K_{II}^1 + K_{II}^2 + K_{II}^3$  vanish at each location  $z$  leads to [187]:

$$\frac{\partial h}{\partial x} = \frac{K_{II}^0}{K_I^0} + \frac{1}{\pi} \frac{2-3\nu}{2(2-\nu)} K_I^0 \int_{-\infty}^{\infty} \frac{h(z) - h(z')}{(z-z')^2} dz' + \eta(z, x, h(z, x)). \quad (48)$$

The form taken by this equation is very similar to that of Eq. (40) which describes the in-plane fluctuations of the crack front. Two main differences are however worth being discussed. The first one comes from the absence of explicit time  $t$  in Eq. (48). This means that the scaling properties of fracture surfaces will not depend on the crack velocity, contrary to those of an interfacial crack front – or those predicted in the phenomenological approach of Section 6.2.1. The second main difference resides in the 3D nature of the stochastic term  $\eta(z, x, h(z, x))$  which actually makes Eq. (49) extremely difficult – if not impossible – to solve. Two limit cases can however be considered.

The first limit consists [21] in considering very smooth fracture surfaces so that the 3D stochastic term  $\eta(z, x, y = h(z, x))$  reduces to an effective “thermal” term  $\eta(z, x)$ . Fracture surfaces are then predicted to exhibit logarithmic scaling. This prediction seems in apparent disagreement with the experimental observations reported in Sections 3 and 4. However, observations performed by Dalmas and coworkers [96] on nanoscale phase separated glasses reveals logarithmic roughness at large length scales (typically larger than the size of the crystalline grains).

The second approximation consists [187] in writing  $\eta(z, x, y = h(z, x))$  as the sum of two 2D terms:  $\eta(z, x, y = h(z, x)) = \eta(z, x) + \eta(z, y = h(z, x))$ . The morphology of the fracture surface  $h(x, z)$  is then given by the motion of the elastic string  $h(z)$  that “creeps” – the  $x$  coordinate playing the role of time – within a random potential  $\eta(z, h(z, x))$  due to the “thermal” fluctuations  $\eta(z, x)$ . The fracture surface  $h(z, x)$  then obeys a Family-Viseck anisotropic self-affine scaling (Eq. (42)) with  $\zeta \simeq 0.4$  and  $\kappa \simeq 0.8$ , in perfect agreement with the observations reported for glassy ceramics and sandstone (see Section 4.1.2).

The values of roughness and dynamic exponents  $\zeta \simeq 0.75$  and  $\kappa \simeq 1.2$  reported for a wide range of materials (see Sections 3.3 and 4.1.1) can now be discussed. In all these materials, the surfaces were observed at *small* length scales, i.e. below a cutoff length of e.g. a few nanometers in quasicrystals [90], a few tens of nanometers in glass [68,187,96], a few hundreds of micrometers in metallic alloys [52], a few millimeters in wood [81,51], a few tens of millimeters in mortar [85, 93]. We have urged [187] that this upper cutoff length be set by the size of the FPZ. Strong arguments in favor of this interpretation have been shown in oxide glasses [187], quasicrystals [90] and mortar [93]. Work in progress [94] seems to indicate that it is also true in metallic alloys: Compact Tension specimens were broken at various temperatures, ranging from 20 to 148 K – this allows one to tune the plastic zone size, from 20  $\mu\text{m}$  to 1 mm. On all the corresponding fracture surfaces, profiles parallel with the initial notch were shown to exhibit a self-affine regime with roughness exponent  $\zeta \simeq 0.75$  bounded by an upper length scale very close to the plastic zone size. Since the scaling characterized by  $\zeta \simeq 0.75$  and  $\kappa \simeq 1.2$  is observed below the process zone size, it cannot be described by the Linear Elastic stochastic equation proposed in this section. One has then to resort to alternative models such as e.g. the stress-weighted percolation models presented in Section 5.4.3 to account for crack propagation at the scale of the FPZ.

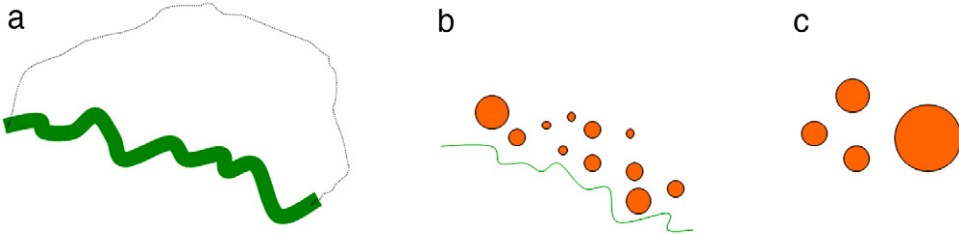


**Fig. 53.** Sketch of the various regimes of roughness observed on a fracture surface. (a) At scales larger than the FPZ size, fracture can be considered as linear elastic and the stochastic model discussed in Section 6 applies, predicting in particular roughness indices  $\zeta \approx 0.4$ ,  $\beta \approx 0.5$  and  $\zeta' \approx 0.4$ ; (b) At intermediate scales, within the FPZ, fracture surfaces are anisotropic and measurements reveal roughness indices  $\zeta \approx 0.75$ ,  $\beta \approx 0.6$  and  $\zeta' \approx 0.6$ ; (c) At the scale of a damage void, where there is no more the notion of an existing crack front, one has  $\zeta = \beta \approx 0.5$ , and the surface is multi-affine. Only in case (a) do we have a theoretical model which explains the observations.

## 7. Discussion

After more than twenty years of debate about the results of delicate experiments aiming at the determination of the morphology of fracture surfaces, it was finally shown that fracture of a three-dimensional solid – whether failure occurs because of crack propagation through a weak plane or not – is indeed a dynamic phase transition, at least in the linear elastic case. As a matter of fact, we have shown (Section 6) [74,182] that the morphology and the dynamics of the in-plane projection of a perfectly elastic crack front are ruled by a stochastic equation describing the vicinity of a depinning transition. This transition separates a pinned phase, where the average velocity of the crack is zero, from a propagating phase, where the crack progresses with finite velocity. It is controlled by the applied mode I stress intensity factor, the critical value of which is the material fracture toughness. The order parameter of this transition is in fact the average velocity of the crack.

We have also shown [187] that for an elastic body, the out-of-plane trajectory is also ruled by a stochastic equation describing the vicinity of a depinning transition. In this case however, time does not play an explicit role, and the order parameter is the average slope of the fracture surface in the direction of crack propagation. What controls the transition is in this case the amount of external shear (ratio of the applied mode II and mode I stress intensity factors), the critical value of this quantity being zero (pure external mode I). This of course justifies the very existence of critical exponents such as the roughness index, and strongly supports the idea of their universality, first proposed twenty years ago [64].

The results of our statistical models were shown to fit the experimental observations performed on materials fulfilling their basic assumptions, i.e. performed at scales large enough so that linear elasticity is a reasonable premise [73,75,93].

However, when materials are observed within the Fracture Process Zone, where dissipative processes of different kinds (plasticity, microcracking, void formation...) become important, these models fail to predict the values of the observed exponents. Nevertheless, at these smaller scales, the structure of the fracture surfaces is similar to what it is in the linear elastic regime, and roughness indices have universal values. In this regime, where fracture surfaces are anisotropic [52], there is no theory yet able to explain the observations, but great hopes rely on models mixing the elastic lines approach and the percolation gradient model [157].

Finally, there is a third regime which can be observed at the scale of a damage cavity in ductile fracture [107,68,78]: in this region, fracture surfaces are isotropic, since any notion of a crack front, and, hence, of a preferred direction, is lost. Fig. 53 is a sketch summarizing the observations performed at various length scales.

Let us note that the crossover between the elastic large scales regime ((a) in Fig. 53) and the intermediate scales regime ((b) in Fig. 53) was claimed to be the size of the largest heterogeneities both for fracture of 3D samples of partially demixed glass [96] and for interfacial fracture in PMMA [55]. Although this is not what was found in steel [94], this interpretation is compatible with experiments on other metallic alloys [67,69] for which, as already mentioned, the upper bound of this regime was found to be of the order of the metallurgical grains. In principle, it is also compatible with the results obtained on mortar fracture surfaces, for which the crossover length was found to be  $\sim 1$  mm [93]. However, in this case, the crossover length was observed to grow, as does the FPZ, which is expected to be of the same order of magnitude.

It is worth emphasizing that progress has been achieved in the understanding of the origin of scaling in fracture mostly thanks to a comparison of different materials [52,51]. Great improvements are also due to the results of the Oslo interfacial fracture experiment [22,23,59,66], where the whole dynamics of crack propagation could be analyzed and compared to the predictions of models. Unfortunately, the Oslo setup seems to be quite unique, and no similar possibility has emerged yet for a three-dimensional system.

Of course, universality is more intuitively understandable when the linear elastic regime of fracture is concerned: in this regime, by definition, differences between materials and the way they fracture are irrelevant. Note that, in this regime, the mechanically relevant disorder should be accessible through an inversion of Eq. (48): knowing the external loading (i.e.  $K_0^I$  and  $K_0^{II}$ ) and the Poisson coefficient  $\nu$ , and by measuring  $h$ , one can access the noise term  $\eta(z; x; h)$ .

The central question which remains open is to understand the universality for fracture within the FPZ, where dissipation mechanisms are very different for different materials. As already discussed in the past [42,34,7,119], as long range elastic

interactions are screened out by damage, one gets into a different universality class, whatever the nature of damage. Universality should persist.

A clue is that if the non-local elastic term in Eq. (49) is replaced by a term which reflects shorter range elastic interactions, i.e. if Eq. (49) is replaced by the following equation:

$$\frac{\partial h}{\partial x} = \frac{K_L^0}{K_I^0} + \frac{1}{\pi} \frac{2-3\nu}{2(2-\nu)} K_I^0 \int_{-\infty}^{\infty} \frac{h(z) - h(z')}{(z-z')^\alpha} dz' + \eta(z, x, h(z, x)) \quad (49)$$

which was studied by Tanguy et al. [189], there is a solution giving  $\zeta \simeq 0.8$  and  $\kappa \simeq 1.2$  if the exponent  $\alpha$  is chosen to be larger than 2 (actually close to the value 2.5). This of course does not constitute a proper model, this  $\alpha$  value being chosen *ad hoc*, it does not have a proper physical meaning, but it is a hint to interpret the measured values of exponents as a result of a modification of the nature of the line tension of the crack front due to screening by damage. Coupled equations describing on one hand crack propagation within an evolving stress field due to damage expansion, and on the other hand damage growth ahead of the moving front should be solved to get a proper description of the phenomenon. As already mentioned, another way is being investigated by A. Hansen, based on the gradient percolation model [157].

On the other hand, an experimental investigation of the extension fluctuations of a crack front similar to the one achieved in [169] for a contact line could be set both for interfacial and full 3D fracture. Measurements of the center-of-mass time fluctuations of the position of the crack front should allow for the determination of the renormalized disorder correlator. A comparison with the prediction of the Functional Renormalization Group should provide a better understanding of the underlying physical processes in the elastic domain. In reverse, within the FPZ, a study of this correlator might provide clues for future theoretical descriptions. Finally, one can learn the size of the fracture process zone, and within it, the local direction of crack propagation from the study of a fracture surface. This can be used for expertise purposes, but also as a tool to understand better complex fracture problems such as stress corrosion for example. Furthermore, fracture can now be used as an interesting diagnosis of problems which are not fully understood, and, for example, it can help in revealing correlations in a glass structure [190].

## Acknowledgements

We are particularly indebted to L. Ponson, to whom several of the important results reviewed here are due. We wish to thank also all our collaborators. E.B. is grateful to J.-P. Bouchaud for his constant support.

## References

- [1] D. François, A. Pineau, A. Zaoui, Comportement mécanique des matériaux, volume I : élasticité plastique, Hermès, 1991.
- [2] D. François, A. Pineau, A. Zaoui, Comportement mécanique des matériaux, Hermès, 1995.
- [3] L. Corté, F. Beaume, L. Leibler, Crystalline organization and toughening: example of polyamide-12, *Polymer* 46 (2005) 2748–2757.
- [4] L. Corté, L. Leibler, Analysis of polymer blend morphologies from transmission electron micrographs, *Polymer* 46 (2005) 6360–6368.
- [5] F. Leonforte, A. Tanguy, J.P. Wittmer, J.L. Barrat, Continuum limit of amorphous elastic bodies ii: linear response to a point source force, *Phys. Rev. B* 70 (2004) 014203.
- [6] F. Leonforte, A. Tanguy, J.-P. Wittmer, J.-L. Barrat, Inhomogeneous elastic response of silica glass, *Phys. Rev. Lett.* 97 (5) (2006) 055501.
- [7] F. Célarié, S. Prades, D. Bonamy, L. Ferrero, E. Bouchaud, C. Guillot, C. Marliere, Glass breaks like metal, but at the nanometer scale, *Phys. Rev. Lett.* 90 (2003) 075504.
- [8] A.A. Griffith, J. Waltamm Jr., The theory of rupture, in: C.B. Biezeno, J.M. Burgers (Eds.), *Proc. First Internat. Congr. Appl. Mech.*, 1924, p. 55.
- [9] L.B. Freund, *Dynamic Fracture Mechanics*, Cambridge University Press, 1990.
- [10] H. Bergkvist, Some experiments on crack motion and arrest in polymethylmethacrylate, *Eng. Fracture Mech.* 6 (1974) 621–626.
- [11] J.-F. Bouquet, S. Ciliberto, Interaction of sound with fast crack propagation, *Phys. Rev. Lett.* 80 (1998) 341–344.
- [12] E. Sharon, J. Fineberg, Confirming the continuum theory of dynamic brittle fracture for fast cracks, *Nature* 397 (1999) 333–335.
- [13] J. Scheibert, C. Guerra, F. Clari, D. Dalmas, D. Bonamy, Brittle/quasi-brittle transition in the dynamic fracture of nominally brittle materials: an energetic signature, *Phys. Rev. Lett.* 104 (2010) 045501.
- [14] A. Livne, E. Bouchbinder, I. Svetlizky, J. Fineberg, The near-tip fields of fast cracks, *Science* 327 (2010) 1359.
- [15] K. Ravi-Chandar, Dynamic fracture of nominally brittle materials, *Int. J. Frac.* 90 (1998) 83–102.
- [16] J. Fineberg, M. Marder, Instability in dynamic fracture, *Phys. Rep.* 313 (1999) 1–108.
- [17] A.B. Movchan, H. Gao, J.R. Willis, On perturbations of plane cracks, *Int. J. Solids Struct.* 26 (1998) 3419–3453.
- [18] K.P. Meade, L.M. Keer, Stress-intensity factor for a semi-infinite plane crack with a wavy front, *J. Elasticity* 14 (1984) 79–92.
- [19] J.R. Rice, 1st-order variation in elastic fields due to variation in location of a planar crack front, *J. Appl. Mech.* 52 (1985) 571–579.
- [20] J. Schmittbuhl, S. Roux, J.P. Vilotte, K.J. Måløy, Interfacial crack pinning: effect of nonlocal interactions, *Phys. Rev. Lett.* 74 (1995) 1787–1790.
- [21] S. Ramanathan, D. Ertas, D.S. Fisher, Quasistatic crack propagation in heterogeneous media, *Phys. Rev. Lett.* 79 (1997) 873.
- [22] J. Schmittbuhl, K.J. Måløy, Direct observation of self-affine crack propagation, *Phys. Rev. Lett.* 78 (1997) 3888–3891.
- [23] A. Delaplace, J. Schmittbuhl, K.J. Måløy, High-resolution description of crack front in heterogeneous plexiglas block, *Phys. Rev. E* 60 (1999) 1337–1343.
- [24] M. Adda-Bedia, E. Katzav, D. Vandembroucq, Second-order variation in elastic fields of a tensile planar crack with a curved front, *Phys. Rev. E* 73 (2006) 035106.
- [25] B. Cotterell, J.R. Rice, Slightly curved or kinked cracks, *Int. J. Frac.* 16 (1980) 155–169.
- [26] H. Larralde, R.C. Ball, The shape of slowly growing cracks, *Europhys. Lett.* 30 (1995) 87–92.
- [27] R.C. Ball, H. Larralde, 3-dimensional stability analysis of planar straight cracks propagating quasi-statically under type-i-loading, *Int. J. Fract.* 71 (1995) 365–377.
- [28] J.R. Willis, A.B. Movchan, Dynamic weight functions for a moving crack. i. mode i loading, *J. Mech. Phys. Solids* 43 (1995) 319–341.
- [29] J.R. Willis, A.B. Movchan, Three dimensional dynamic perturbation of a dynamic propagating crack, *J. Mech. Phys. Solids* 45 (1997) 591.
- [30] S. Ramanathan, D.S. Fisher, Dynamics and instabilities of planar tensile cracks in heterogeneous media, *Phys. Rev. Lett.* 79 (1997) 877.
- [31] J.W. Morrissey, J.R. Rice, Crack front waves, *J. Mech. and Physics of Solids* 46 (1998) 467–487.
- [32] J.W. Morrissey, J.R. Rice, Perturbative simulations of crack front waves, *J. Mech. and Physics of Solids* 48 (2000) 1229–1251.

- [33] E. Sharon, G. Cohen, J. Fineberg, Propagating solitary waves along a rapidly moving crack front, *Nature* 410 (2001) 68–71.
- [34] E. Bouchaud, J.P. Bouchaud, D.S. Fisher, S. Ramanathan, J.R. Rice, Can crack front waves explain the roughness of cracks? *J. Mech. Phys. Solids* 50 (2002) 1703–1725.
- [35] E. Sharon, G. Cohen, J. Fineberg, Crack front waves and the dynamics of a rapidly moving crack, *Phys. Rev. Lett.* 88 (8) (2002) 085503.
- [36] D. Bonamy, K. Ravi-Chandar, Interaction of shear waves and propagating cracks, *Phys. Rev. Lett.* 91 (2003) 235502.
- [37] D. Bonamy, K. Ravi-Chandar, Dynamic crack response to a localized shear pulse perturbation in brittle amorphous materials: on crack surface roughening, *Int. J. Fract.* 134 (2005) 1–22.
- [38] E. Sharon, G. Cohen, J. Fineberg, Comment on: “interaction of shear waves and propagating cracks”, *Phys. Rev. Lett.* 93 (2004) 099601–1.
- [39] D. Bonamy, K. Ravi-Chandar, Reply on: interaction of shear waves and propagating cracks, *Phys. Rev. Lett.* 93 (2004) 099602.
- [40] R.V. Goldstein, R.L. Salganik, Brittle fracture of solids with arbitrary cracks, *Int. J. Frac.* 10 (1974) 507–523.
- [41] E. Sommer, Formation of fracture ‘lances’ in glass, *Eng. Frac. Mech.* 1 (1969) 539–540.
- [42] E. Bouchaud, F. Paun, Fracture and damage at a microstructural scale, *Comp. Sci. Eng.* September–October (1) (1999).
- [43] S. Morel, G. Mourou, J. Schmittbuhl, Influence of the specimen geometry on r-curve behavior and roughening of fracture surfaces, *Int. J. Frac.* 121 (2003) 23–42.
- [44] S. Prades, D. Bonamy, D. Dalmas, E. Bouchaud, C. Guillot, Nano-ductile crack propagation in glasses under stress corrosion: spatiotemporal evolution of damage in the vicinity of the crack tip, *Int. J. Solid Struct.* 42 (2005) 637–645.
- [45] C.L. Rountree, R.K. Kalia, E. Lidorikis, A. Nakano, L. Van Bruntzel, P. Vashishta, Atomistic aspects of crack propagation in brittle materials: multimillion atom molecular dynamics simulations, *Ann. Rev. Mater. Res.* 32 (2002) 377–400.
- [46] J.P. Guin, S.M. Wiederhorn, Fracture of silicate glasses: Ductile or brittle? *Phys. Rev. Lett.* 92 (2004) 215502/1–4.
- [47] J.P. Guin, S.M. Wiederhorn, Surfaces formed by subcritical crack growth in silicate glasses, *Int. J. Fract.* 140 (2006) 15–26.
- [48] K. Han, M. Ciccotti, S. Roux, Measuring nanoscale stress intensity factors with an atomic force microscope, *Eur. Phys. Lett.* 89 (2010) 66003.
- [49] S. Wiederehorn, J. Lopez-Cepero, J. Wallace, J.-P. Guin, T. Fett, Roughness of glass surfaces formed by sub-critical crack growth, *J. Non-Cryst. Solids* 353 (2007) 1582–1591.
- [50] F. Lechenault, G. Pallares, M. George, C. Rountree, E. Bouchaud, M. Ciccotti, Effects of finite probe size on self-affine roughness measurements, *Phys. Rev. Lett.* 104 (2010) 025502.
- [51] L. Ponson, D. Bonamy, H. Auradou, G. Mourou, S. Morel, E. Bouchaud, C. Guillot, J.-P. Hulin, Anisotropic self-affine properties of experimental fracture surfaces, *Int. J. Frac.* 140 (2006) 27–37.
- [52] L. Ponson, D. Bonamy, E. Bouchaud, 2d scaling properties of experimental fracture surfaces, *Phys. Rev. Lett.* 96 (2006) 035506.
- [53] B.B. Mandelbrot, D.E. Passoja, A.J. Paullay, Fractal character of fracture surfaces of metals, *Nature* 308 (1984) 721–722.
- [54] J. Kertész, V.K. Horvath, F. Weber, Self-affine rupture lines in paper sheets, *Fractals* 1 (1993) 67–74.
- [55] S. Santucci, K.J. Måløy, A. Delaplace, J. Mathiesen, A. Hansen, J. Bakke, J. Schmittbuhl, L. Vanel, P. Ray, Statistics of fracture surfaces, *Phys. Rev. E* (2007) 75:016104–1–016104–6.
- [56] L.I. Salminen, M.J. Alava, K.J. Niskanen, Analysis of long crack lines in paper webs, *Eur. Phys. J. B* 32 (2003) 369–374.
- [57] N. Mallick, P.-P. Cortet, S. Santucci, S.G. Roux, L. Vanel, Discrepancy between subcritical and fast rupture roughness: a cumulant analysis, *Phys. Rev. Lett.* 98 (2007) 255502.
- [58] E. Bouchbinder, I. Procaccia, S. Santucci, L. Vanel, Fracture surfaces as multiscaling graphs, *Phys. Rev. Lett.* 96 (5) (2006) 055509.
- [59] K.J. Måløy, S. Santucci, J. Schmittbuhl, R. Toussaint, Local waiting time fluctuations along a randomly pinned crack front, *Phys. Rev. Lett.* 96 (2006) 045501.
- [60] S. Santucci, M. Grob, A. Hansen, R. Toussaint, J. Schmittbuhl, K.J. Måløy, Fracture roughness scaling: a case study on planar cracks, 2010. [arXiv:1007.1188v1 \[cond-mat.mtrl-sci\]](https://arxiv.org/abs/1007.1188v1).
- [61] A. Marchenko, D. Fichou, D. Bonamy, E. Bouchaud, Time resolved observation of fracture events in mica crystal using scanning tunneling microscope, *Appl. Phys. Lett.* 89 (2006) 093124.
- [62] J.-W. Obreimoff, The splitting strength of mica, *Proc. Roy. Soc. Lond. A* 127 (1930) 290–297.
- [63] P. Daguer, E. Bouchaud, G. Lapasset, Roughness of crack front pinned by microstructural obstacles, *Europhys. Lett.* 31 (1995) 367–372.
- [64] E. Bouchaud, G. Lapasset, J. Planes, Fractal dimension of fractured surfaces: A universal value? *Europhys. Lett.* 13 (1990) 73–79.
- [65] J. Feder, *Fractals*, Plenum, 1988.
- [66] K.J. Måløy, A. Hansen, E.L. Hinrichsen, S. Roux, Experimental measurements of the roughness of brittle cracks, *Phys. Rev. Lett.* 68 (1992) 213–215.
- [67] P. Daguer, S. Hénaux, E. Bouchaud, F. Creuzet, Quantitative analysis of a fracture surface by atomic force microscopy, *Phys. Rev. E* 53 (1996) 5637.
- [68] P. Daguer, B. Nghiem, E. Bouchaud, F. Creuzet, Pinning and depinning of crack fronts in heterogeneous materials, *Phys. Rev. Lett.* 78 (1997) 1062–1065.
- [69] M. Hinojosa, E. Bouchaud, B. Nghiem, Long distance roughness of fracture surfaces in heterogeneous materials, in: G.E. Beltz, R.L. Blumberg Selinger, M.P. Marder, K.-S. Kim (Eds.), *Materials Research Society Proceedings*, MRS Fall Meeting 1998, vol. 539, 1999, pp. 203–208.
- [70] J. Schmittbuhl, F. Schmitt, G. Scholz, Scaling invariance of crack surfaces, *J. Geophys. Res.* 100 (1995) 5953–5973.
- [71] J.M. Boffa, C. Allain, J.-P. Hulin, Experimental analysis of fracture rugosity in granular and compact rocks, *Eur. Phys. J. AP* 2 (1998) 281–289.
- [72] J.-M. Boffa, C. Allain, J.-P. Hulin, Experimental analysis of self-affine fractured rock surfaces through shadow length measurements, *Physica A* 278 (2000) 65–86.
- [73] L. Ponson, H. Auradou, P. Vié, J.P. Hulin, Low self-affine exponents of fractured glass ceramics surfaces, *Phys. Rev. Lett.* 97 (2006) 125501.
- [74] L. Ponson, Crack propagation in disordered materials: how to decypher fracture surfaces, *Annales de Physique* 32 (2007) 1.
- [75] L. Ponson, H. Auradou, M. Pessel, V. Lazarus, J.P. Hulin, Failure mechanisms and surface roughness statistics of fractured fontainebleau sandstone, *Phys. Rev. E* 76 (2008) 036108.
- [76] J.M. López, J. Schmittbuhl, Anomalous scaling of fracture surfaces, *Phys. Rev. E* 57 (1998) 6405–6408.
- [77] E. Bouchaud, S. Naveos, From quasi-static to rapid fracture, *J. Phys. I France* 5 (1995) 547.
- [78] E. Bouchaud, D. Boivin, J.-L. Pouchou, D. Bonamy, B. Poon, G. Ravichandran, Fracture through cavitation in a metallic glass, *Europhys. Lett.* 83 (2008) 66006.
- [79] E. Bouchaud, G. Lapasset, J. Planes, S. Navéos, Statistics of branched fracture surfaces, *Phys. Rev. B* 48 (1993) 2917–2928.
- [80] T. Engoy, K.J. Måløy, A. Hansen, S. Roux, Roughness of two-dimensional cracks in wood, *Phys. Rev. Lett.* 73 (1994) 834.
- [81] S. Morel, J. Schmittbuhl, J.M. López, G. Valentin, Anomalous roughening of wood fractured surfaces, *Phys. Rev. E* 58 (1998) 6999–7005.
- [82] S. Morel, J. Schmittbuhl, E. Bouchaud, G. Valentin, Scaling of crack surfaces and implications for fracture mechanics, *Phys. Rev. Lett.* 85 (2000) 1678–1681.
- [83] S. Morel, E. Bouchaud, G. Valentin, Size effect in fracture: roughening of crack surfaces and asymptotic analysis, *Phys. Rev. B* 65 (2002) 104101.
- [84] E. Bouchaud, Scaling properties of cracks, *J. Phys. Condens. Matter* 9 (1997) 4319–4344.
- [85] G. Mourou, S. Morel, E. Bouchaud, G. Valentin, Anomalous scaling of mortar fracture surfaces, *Phys. Rev. E* 71 (2005) 016136–1–016136–7.
- [86] J.P. Bouchaud, E. Bouchaud, G. Lapasset, J. Planes, Models of fractal cracks, *Phys. Rev. Lett.* 71 (1993) 2240–2243.
- [87] J.J. Ammann, E. Bouchaud, Characterization of self-affine surfaces from 3d digital reconstruction, *Eur. Phys. J. B Appl. Phys.* 4 (1998) 133–142.
- [88] F. Célarié, S. Morel, D. Bonamy, A. Dickelé, E. Bouchaud, C. Guillot, C. Marlière, Surface fracture of glassy materials as detected by real-time atomic force microscopy (afm) experiments, *Appl. Surf. Sci.* 212 (2003) 92–96.
- [89] F. Family, T. Vicsek, *Dynamic of Fractal Surfaces*, World Scientific, 1991.
- [90] L. Ponson, D. Bonamy, L. Barbier, Cleaved surface of i-alpdmn quasicrystals: influence of the local temperature elevation at the crack tip on the fracture surface roughness, *Phys. Rev. B* 74 (2006) 184205.
- [91] E. Bouchbinder, I. Procaccia, S. Sela, Disentangling scaling properties in anisotropic fracture, *Phys. Rev. Lett.* 95 (2005) 255503.

- [92] G. Pallares, L. Ponson, S. Chapuliot, E. Bouchaud, (Unpublished).
- [93] S. Morel, D. Bonamy, L. Ponson, E. Bouchaud, Transient damage spreading and anomalous scaling in mortar crack surfaces, Phys. Rev. E 78 (2008) 016112–1–016112–5.
- [94] C. Guerra-Amaro, D. Bonamy, S. Chapuliot, E. Bouchaud, Process zone size determination from the morphology of steel fracture surfaces (Unpublished).
- [95] J. Schmittbuhl, S. Gentier, S. Roux, Field-measurements of the roughness of fault surfaces, Geophys. Lett. 20 (1993) 639–641.
- [96] D. Dalmas, A. Lelarge, D. Vandembroucq, Crack propagation through phase-separated glasses: effect of the characteristic size of disorder, Phys. Rev. Lett. 101 (2008) 255501.
- [97] E. Bouchaud, The morphology of fracture surfaces: a tool for understanding crack propagation in complex materials, Surf. Rev. Lett. 10 (2003) 797–814.
- [98] M.L. Falk, Molecular-dynamics study of ductile and brittle fracture in model noncrystalline solids, Phys. Rev. B 60 (1999) 7062–7070.
- [99] P. Schall, D.A. Weitz, F. Spaepen, Structural rearrangements that govern flow in colloidal glasses, Science 318 (5858) (2007) 1895–1899.
- [100] R. Besseling, E.R. Weeks, A.B. Schofield, W.C.K. Poon, Three-dimensional imaging of colloidal glasses under steady shear, Phys. Rev. Lett. 99 (2) (2007) 028301.
- [101] M.L. Falk, J.S. Langer, Dynamics of viscoplastic deformation in amorphous solids, Phys. Rev. E 57 (1998) 7192–7205.
- [102] A.S. Argon, Plastic deformation in metallic glasses, Acta Met. 27 (1979) 47–58.
- [103] L. Van Brutzel, E. Bouchaud, Molecular dynamics simulations of crack propagation mode in silica, in: School on Physics of Glass - Structure and Dynamics, May 10–22, 1999, Institut d'Etudes Scientifiques de Cargse, France, Physics of Glasses - Structure and Dynamics, in: P. Jund, R. Jullien (Eds.), AIP Conference Proceedings, vol. 489, 1999, pp. 231–235.
- [104] P. Vashishta, R.K. Kalia, J.P. Rino, I. Ebbsjo, Interaction potential for SiO<sub>2</sub>: a molecular-dynamics study of structural correlations, Phys. Rev. B 41 (1990) 12197–12210.
- [105] C.L. Rountree, S. Prades, D. Bonamy, E. Bouchaud, R.K. Kalia, C. Guillot, A unified study of crack propagation in amorphous silica: Using experiments and simulations, J. Alloys Compd. 434–435 (2007) 60–63.
- [106] R.K. Kalia, A. Nakano, K. Tsuruta, P. Vashishta, Morphology of pores and interfaces and mechanical behavior of nanoclustered-assembled silicon nitride ceramic, Phys. Rev. Lett. 78 (1997) 689.
- [107] A. Nakano, R.K. Kalia, P. Vashishta, Dynamics and morphology of brittle cracks: a molecular-dynamics study of silicon-nitride, Phys. Rev. Lett. 75 (1995) 3138–3141.
- [108] Y.-C. Chen, Z. Lu, K. Nomura, W. Wang, R.K. Kalia, A. Nakano, P. Vashishta, Interaction of voids and nanoductility in silica glass, Phys. Rev. Lett. 99 (2007) 155506.
- [109] Y.C. Chen, K. Nomura, R.K. Kalia, A. Nakano, P. Vashishta, Void deformation and breakup in shearing silica glass, Phys. Rev. Lett. 103 (2009) 035501.
- [110] B. Lawn, Fracture of Brittle Solids, Cambridge University Press, 1993.
- [111] M. Ciccotti, Stress-corrosion mechanisms in silicate glasses, J. Phys. D: Appl. Phys. 42 (2009) 214006(1–18).
- [112] M. Tomozawa, W.-T. Han, W.A. Lanford, Water entry into silica glass during slow crack growth, J. Am. Ceram. Soc. 74 (1991) 2573–2576.
- [113] M. Tomozawa, Fracture of glasses, Ann. Rev. Mat. Sci. 26 (1996) 43–74.
- [114] A. Grimaldi, M. George, G. Pallares, M. Ciccotti, The crack tip: a nanolab for studying confined liquids, Phys. Rev. Lett. 100 (2008) 165505.
- [115] T.A. Michaels, S.W. Freeman, A molecular mechanism for stress corrosion in vitreous silica, J. Am. Ceram. Soc. 68 (1983) 284–288.
- [116] D. Bonamy, S. Prades, C.L. Rountree, L. Ponson, D. Dalmas, E. Bouchaud, K. Ravi-Chandar, C. Guillot, Nanoscale damage during fracture in silica glass, Int. J. Fract. 140 (2006) 3–14.
- [117] D. Bonamy, S. Prades, L. Ponson, D. Dalmas, C.L. Rountree, E. Bouchaud, C. Guillot, Experimental investigation of damage and fracture in glassy materials at the nanometer scale, Int. J. Prod. Tech. 26 (2006) 339–353.
- [118] E. Bouchbinder, J. Mathiesen, I. Procaccia, Roughening of fracture surfaces: the role of plastic deformation, Phys. Rev. Lett. 92 (24) (2004) 245505.
- [119] E. Bouchbinder, J. Mathiesen, I. Procaccia, Stress field around arbitrarily shaped cracks in two-dimensional elastic materials, Phys. Rev. E 69 (2 Part 2) (2004) 026127.
- [120] I. Afek, E. Bouchbinder, E. Katzav, J. Mathiesen, I. Procaccia, Void form and roughening in slow fracture, Phys. Rev. E 71 (2005) 066127.
- [121] S. Santucci, L. Vanel, S. Ciliberto, Subcritical statistics in rupture of fibrous materials: experiments and model, Phys. Rev. Lett. 93 (2004) 095505.
- [122] F.T. Pierce, Tensile tests for cotton yarns. v. the weakest link-theorems on the strength of long and short composite specimens, J. Textile Institute Trans. 17 (1926) 355–368.
- [123] P.C. Hemmer, A. Hansen, S. Pradhan, Rupture processes in fibre bundle models, Lecture Notes in Physics 705 (2006) 27–55.
- [124] F. Kun, F. Raischel, R.C. Hidalgo, H.J. Herrmann, Extensions of fibre bundle models, Lecture Notes in Phys. 705 (2006) 57–92.
- [125] H.E. Daniels, The statistical theory of the strength of bundles and threads, Proc. Roy. Soc. Lond. Ser. A Math. 183 (1945) 405–435; Phys. Sci. 183 (1945) 405–435. 995.
- [126] D. Sornette, Mean-field solution of a block-spring model of earthquakes, J. Phys. I France 2 (1992) 2089–2096.
- [127] L. de Arcangelis, S. Redner, H.J. Herrmann, A random fuse model for breaking processes, J. Phys. Lett. (Paris) 46 (1985) 585–590.
- [128] H.J. Herrmann, S. Roux, Statistical Model for the Fracture and Breakdown for Disordered Media, North Holland, Amsterdam, 1990.
- [129] M.J. Alava, P.K.V.V. Nukala, S. Zapperi, Statistical models of fracture, Adv. Phys. 55 (2006) 349–476.
- [130] Y.S. Li, P.M. Duxbury, Crack arrest by residual bonding in resistor and spring networks, Phys. Rev. B Condensed Matter 38 (13) (1988) 9257–9260.
- [131] S. Zapperi, A. Vespuignani, H.E. Stanley, Plasticity and avalanche behaviour in microfracturing phenomena, Nature 388 (1997) 658–660.
- [132] L. de Arcangelis, A. Hansen, H.J. Herrmann, S. Roux, Scaling laws in fracture, Phys. Rev. B Condens. Matter 40 (1) (1989) 877–880.
- [133] M. Sahimi, S. Arbab, Mech. of disordered solids. iii. fracture properties, Phys. Rev. B Condens. Matter 47 (2) (1993) 713–722.
- [134] P.M. Duxbury, P.D. Beale, P.L. Leath, Size effect of electrical breakdown in quenched random media, Phys. Rev. Lett. 57 (1986) 1052–1055.
- [135] P.K.V.V. Nukala, S. Simunovic, Scaling of fracture strength in disordered quasi-brittle materials, Eur. Phys. J. B 37 (2004) 91–100.
- [136] S. Zapperi, P.K.V.V. Nukala, Fracture statistics in the three-dimensional random fuse model, Int. J. Frac. 140 (2006) 99–111.
- [137] A. Hansen, P.C. Hemmer, Burst avalanches in bundles of fibers - local versus global load-sharing, Phys. Lett. A 184 (1994) 394–396.
- [138] S. Zapperi, P.K.V.V. Nukala, S. Simunovic, Crack roughness and avalanche precursors in the random fuse model, Phys. Rev. E 71 (2005) 026106.
- [139] S. Zapperi, P.K.V.V. Nukala, S. Simunovic, Crack avalanches in the three-dimensional random fuse model, Physica A 357 (2005) 129–133.
- [140] S. Deschanel, L. Vanel, N. Godin, G. Vigier, S. Ciliberto, Experimental study of crackling noise: conditions on power law scaling correlated with fracture precursors, J. Stat. Mech.: Theor. Exp. P01018 (2009) 1–13.
- [141] T. Utsu, Representation and analysis of the earthquake size distribution: A historical review and some new approaches, Pure Appl. Geophys. 155 (1999) 509–535.
- [142] M. Minozzi, G. Caldarelli, L. Pietronero, S. Zapperi, Dynamic fracture model for acoustic emission, Eur. Phys. J. B 36 (2003) 203–207.
- [143] B. Pant, S. Morel, E. Bouchaud, Acoustic emission tracking of failure precursors in cement.
- [144] L.I. Salminen, A.I. Tolvanen, M.J. Alava, Acoustic emission from paper fracture, Phys. Rev. Lett. 89 (18) (2002) 185503.
- [145] A. Hansen, H. Hinrichsen, S. Roux, Roughness of crack interfaces, Phys. Rev. Lett. 66 (19) (1991) 2476–2479.
- [146] G.C. Batrouni, A. Hansen, Fracture in three-dimensional fuse networks, Phys. Rev. Lett. 80 (1998) 325–328.
- [147] V.I. Raisanen, E.T. Seppala, M.J. Alava, P.M. Duxbury, Quasistatic cracks and minimal energy surfaces, Phys. Rev. Lett. 80 (1998) 329–332.
- [148] V.I. Raisanen, M.J. Alava, R.M. Nieminen, Fracture of three-dimensional fuse networks with quenched disorder, Phys. Rev. B 58 (1998) 14288–14295.
- [149] E.T. Seppala, V.I. Raisanen, M.J. Alava, Scaling of interfaces in brittle fracture and perfect plasticity, Phys. Rev. E 61 (6 Pt A) (2000) 6312–6319.
- [150] P.K.V.V. Nukala, S. Zapperi, S. Simunovic, Crack surface roughness in three-dimensional random fuse networks, Phys. Rev. E 74 (2 Pt 2) (August 2006) 026105.
- [151] P.K.V.V. Nukala, S. Zapperi, M.J. Alava, S. Simunovic, Effect of disorder and notches on crack roughness, Phys. Rev. E 76 (5 Pt 2) (2007) 056111.

- [152] S. Roux, A. Hansen, Perfect plasticity in a random medium, *J. Phys. II (France)* 2 (1992) 1007–1021.
- [153] T. Halpin-Healy, Directed polymers in random media: Probability distributions, *Phys. Rev. A* 44 (1991) R3415–R3418.
- [154] M. Kardar, G. Parisi, Y.-C. Zhang, Dynamic scaling of growing interfaces, *Phys. Rev. Lett.* 56 (1986) 889.
- [155] A.A. Middleton, Numerical results for the ground-state interface in a random medium, *Phys. Rev. E* 52 (1995) R3337–R3340.
- [156] M. Hinojosa, E. Reyes-Melo, C. Guerra, V. Gonzalez, U. Ortiz, Scaling properties of slow fracture in glass: from deterministic to irregular topography, *Int. J. Frac.* 151 (2008) 81–93.
- [157] A. Hansen, J. Schmittbuhl, Origin of the universal roughness exponent of brittle fracture surfaces: stress weighted percolation in the damage zone, *Phys. Rev. Lett.* 90 (2003) 45504.
- [158] J. Schmittbuhl, A. Hansen, Roughness of interfacial crack fronts: stress-weighted percolation in the damage zone, *Phys. Rev. Lett.* 90 (2003) 045505.
- [159] R. Toussaint, S.R. Pride, Fracture of disordered solids in compression as a critical phenomenon. i. statistical mechanics formalism, *Phys. Rev. E* 66 (3 Part 2A) (2002) 036135.
- [160] R. Toussaint, S.R. Pride, Fracture of disordered solids in compression as a critical phenomenon. ii. model hamiltonian for a population of interacting cracks, *Phys. Rev. E* 66 (3 Part 2A) (2002) 036136.
- [161] R. Toussaint, S.R. Pride, Fracture of disordered solids in compression as a critical phenomenon. iii. analysis of the localization transition, *Phys. Rev. E* 66 (3 Part 2A) (2002) 036137.
- [162] S. Zapperi, H.J. Herrmann, S. Roux, Planar cracks in the fuse model, *Eur. Phys. J. B* 17 (2000) 131–136.
- [163] P.K.V. Nukala, S. Zapperi, M.J. Alava, S. Simunovic, Crack roughness in the two-dimensional random threshold beam model, *Phys. Rev. E* 78 (2008) 046105 (1–8).
- [164] H. Gao, J.R. Rice, A first order perturbation analysis on crack trapping by arrays of obstacles, *J. Appl. Mech.* 56 (1989) 828.
- [165] G. Bertotti, G. Durin, A. Magni, Scaling aspects of domain wall dynamics and barkhausen effect in ferromagnetic materials, *J. Appl. Phys.* 75 (1994) 5490–5492.
- [166] G. Durin, S. Zapperi, Scaling exponents for barkhausen avalanches in polycrystalline and amorphous ferromagnets, *Phys. Rev. Lett.* 84 (2000) 4705–4708.
- [167] D. Ertas, M. Kardar, Critical dynamics of contact line depinning, *Phys. Rev. E* 49 (1994) R2532.
- [168] E. Rolley, C. Guthmann, R. Gombrowicz, V. Repain, Roughness of the contact line on a disordered substrate, *Phys. Rev. Lett.* 80 (1998) 2865–2868.
- [169] P. Le Doussal, K.J. Wiese, S. Moulinet, E. Rolley, Height fluctuations of a contact line: a direct measurement of the renormalized disorder correlator, *EPL* 87 (2009) 56001p1–p6.
- [170] M. Kardar, Nonequilibrium dynamics of interfaces and lines, *Phys. Reports* 301 (1998) 85–112.
- [171] P. Chauve, P. Le Doussal, K.J. Wiese, Renormalization of pinned elastic systems: how does it work beyond one loop? *Phys. Rev. Lett.* 86 (2001) 1785–1788.
- [172] O. Duemmer, W. Krauth, Depinning exponents of the driven long-range elastic string, *J. Statist. Mech.* 1 (2007) 01019.
- [173] L. Ponson, Depinning transition in failure of disordered brittle materials, in: 2008 APS March Meeting, 2008.
- [174] L. Ponson, Depinning transition in the failure of inhomogeneous brittle materials, *Phys. Rev. Lett.* 103 (2009) 055501.
- [175] M.V. Feigelman, V.B. Geshkenbein, A.I. Larkin, V.M. Vinokur, Theory of collective flux creep, *Phys. Rev. Lett.* 63 (1989) 2303–2306.
- [176] A.B Kolton, A. Rosso, T. Giamarchi, Creep motion of an elastic string in a random potential, *Phys. Rev. Lett.* 94 (4) (2005) 047002.
- [177] J. Koivisto, J. Rosti, M.J. Alava, Creep of a fracture line in paper peeling, *Phys. Rev. Lett.* 99 (2007) 145504.
- [178] S. Roux, D. Vandembroucq, F. Hild, Effective toughness of heterogeneous brittle materials, *Eur. J. Mech. A/Solids* 22 (2003) 743–749.
- [179] Y. Charles, D. Vandembroucq, F. Hild, S. Roux, Material-independent crack arrest statistics, *J. Mech. Phys. Sol.* 52 (2004) 1651–1669.
- [180] Y. Charles, F. Hild, S. Roux, D. Vandembroucq, Material-independent crack arrest statistics: application to indentation experiments, *Int. J. Fract.* 142 (2006) 51–67.
- [181] P. Bak, C. Tang, K. Wiesenfeld, Self-organized criticality: an explanation of 1/f noise, *Phys. Rev. Lett.* 59 (1987) 381–384.
- [182] D. Bonamy, S. Santucci, L. Ponson, Crackling dynamics in material failure as the signature of a self-organized dynamic phase transition, *Phys. Rev. Lett.* 101 (2008) 045501.
- [183] A.B Kolton, A. Rosso, T. Giamarchi, W. Krauth, Dynamics below the depinning threshold in disordered elastic systems, *Phys. Rev. Lett.* 97 (5) (2006) 057001.
- [184] A. Rosso, W. Krauth, Roughness at the depinning threshold for a long-range elastic string, *Phys. Rev. E* 65 (2002) 25101.
- [185] H. Leshhorn, T. Nattermann, S. Sepanow, L.-H. Tang, Driven interface depinning in a disordered medium, *Ann. Phys.* 6 (1997) 1–34.
- [186] D. Ertas, M. Kardar, Dynamic roughening of directed lines, *Phys. Rev. Lett.* 69 (1992) 929.
- [187] D. Bonamy, L. Ponson, S. Prades, E. Bouchaud, C. Guillot, Scaling exponents for fracture surfaces in homogeneous glass and glassy ceramics, *Phys. Rev. Lett.* 97 (2006) 135504.
- [188] E. Katzav, M. Adda-Bedia, B. Derrida, Fracture surfaces of heterogeneous materials: a 2d solvable model, *Eur. Phys. Lett.* 78 (2007) 46006.
- [189] A. Tanguy, M. Gounelle, S. Roux, From individual to collective pinning: effect of long-range elastic interactions, *Phys. Rev. E* 58 (1998) 1577–1590.
- [190] M. Mosayebi, E. Del Gado, P. Ilg, H.C. Ottinger, Probing a critical length scale at the glass transition, *Phys. Rev. Lett.* 104 (2010) 205704.